

The Pennsylvania State University  
The Graduate School  
Department of Mechanical Engineering

**STUDY OF PERFORMANCE AND CHARACTERISTICS OF  
MATERIALS UNDER EXTREME ENVIRONMENT USING THE  
REAXFF REACTIVE MOLECULAR DYNAMICS  
SIMULATIONS**

A Dissertation in  
Mechanical Engineering

by  
Ali Rahnamoun

© 2016 Ali Rahnamoun  
Submitted in Partial Fulfillment  
of the Requirements  
for the Degree of  
Doctor of Philosophy  
August 2016

The dissertation of Ali Rahnamoun was reviewed and approved\* by the following:

Adri C.T van Duin

Professor of Mechanical Engineering, Penn State University

Dissertation Adviser

Chair of Committee

Richard Yetter

Professor of Mechanical Engineering

Yuan Xuan

Assistant professor of Mechanical Engineering

Deborah Levin

Professor of Aerospace Engineering

Coray Colina

Professor of Material Science and Engineering

Karen Thole

Professor of Mechanical Engineering

Professor-In-Charge of MNE Graduate Programs

\*Signatures are on file in the Graduate School

## ABSTRACT

The primary focus of this work is the study of different materials at extreme environment. These extreme environments include Atomic Oxygen (AO) impacts, ice cluster impacts, noble gas ions irradiation and electron irradiation on different materials.

AO is the most abundant element in the low Earth orbit (LEO). It is the result of the dissociation of molecular oxygen by ultraviolet radiation from the sun. In the LEO, AO collides with the materials used on spacecraft surfaces and causes degradation of these materials. The degradation of the materials on the surface of spacecraft at LEO has been a significant problem for a long time. Kapton polyimide, polyhedral oligomeric silsesquioxane (POSS), silica, and Teflon are the materials used in spacecraft industry. Degradation caused by AO impact is an important issue in these materials applications on spacecraft surface. To investigate the surface chemistry of these materials in exposure to space AO, a computational chemical evaluation of the Kapton polyimide, POSS, amorphous silica, and Teflon was performed in separate simulations under similar conditions. For performing these simulations, the ReaxFF reactive force-field program was used, which provides the computational tool required to perform molecular dynamics (MD) simulations on system sizes sufficiently large to describe the full chemistry of the reactions. Using these simulations, the effects of AO impact on different materials and the role of impact energies, the content of material, and the temperature of material on their behavior are studied. The ReaxFF results indicate that Kapton is less resistant than Teflon against AO damage. These results are in good agreement with the MISSE experimental results. In the MISSE projects, the mass loss of different materials is studied during space missions. These simulations indicate that the amorphous silica shows the highest stability among these materials before the start of the

highly exothermic silicon oxidation. We have verified that adding silicon to the bulk of the Kapton structure enhances the stability of the Kapton against AO impact. Our canonical MD simulations demonstrate that an increase in the heat transfer in materials during AO impact can provide a considerable decrease in the disintegration of the material. This effect is especially relevant in silica AO collision.

During aircraft or spacecraft missions, ice accumulates on different parts of their surface. We studied the dynamics of the collisions between amorphous silica structures and amorphous and crystal ice clusters with impact velocities of 1, 4 and 7 km/s using the ReaxFF reactive molecular dynamics simulation method. The 1km/s and lower impact velocities can happen during aircraft missions and the impact velocities higher than 1 km/s can happen during spacecraft missions. The initial ice clusters consist of 150 water molecules for the amorphous ice cluster and 128 water molecules for the crystal ice cluster. The ice clusters are collided on the surface of amorphous fully oxidized and suboxide silica. These simulations show that at 1 km/s impact velocities, all the ice clusters accumulate on the surface and at 4 km/s and 7 km/s impact velocities, some of the ice cluster molecules bounce back from the surface. We also studied the effect of the second ice cluster impacts on the surfaces which are fully covered with ice, in particular their mass loss/accumulation. These studies show that at 1 km/s impacts, the entire ice cluster accumulates on the silica surface. At 7 km/s impact velocity some ice molecules, which are part of the ice layers accreted on the silica surface, will separate from the ice layers on the surface. At 4 km/s ice cluster impact, ice accumulation is observed for the crystal ice cluster impacts and ice separation is observed for the amorphous ice impacts.

Observing the temperatures of the ice clusters during the collisions indicates that the possibility of electron excitation at impact velocities less than 10 km/s is minimal and ReaxFF reactive

molecular dynamics simulation can predict the chemistry of these hypervelocity impacts. However, at impact velocities close to 10 km/s the average temperature of the impacting ice clusters increase to about 2000K, with individual molecules occasionally reaching temperatures of over 8000K and thus it will be prudent to consider the concept of electron excitation at these higher impact velocities, which goes beyond the current ReaxFF ability.

An important parameter affecting the ability to remove this ice from the surface is the heat transfer characteristics of the accumulated ice. The ice heat transfer is related to the process of ice formation and its density and internal structure. We investigated the effects of ice and silica structure and the ice cluster attachment mechanism to the silica surface on the thermal conductivity (TC) of the attached ice cluster using the ReaxFF reactive molecular dynamics method. The purpose of this study is to investigate the thermal transport in amorphous and crystalline ice after deposition on the silica surfaces. A dual thermostat method was applied for the calculation of TC values. The validity of this method was verified by comparing the calculated values of TC for crystal and amorphous ice with available experimental values. Our calculations show that the TC value for both crystal and amorphous ice drop after deposition on the silica surfaces. This decrease in the TC is more significant for the ice deposition on suboxide silica surfaces. Furthermore, crystal ice shows higher TC values than amorphous ice after accumulation. However, when crystal ice impacts on the silica surface at 1 km/s impact speed, the crystalline shape of the ice cluster is lost to a considerable level and the TC values obtained for the ice clusters in such cases are closer to amorphous ice TC values. We observed a decrease in the TC values when ionic species are added inside the ice clusters.

We studied Kr noble gas ions irradiations on graphene, and the subsequent annealing of the irradiated graphene. Different types of defects were generated in graphene after noble gas ion

irradiations. Kr irradiation mostly caused mono vacancy defects in graphene while light noble gas ions can mostly generate Stone-Wales defects in graphene. The irradiated graphene was annealed between 300K and 2000K and the reconstruction of the defects was studied.

In order to study the electron beam irradiation on Kapton using molecular simulation, electron beams irradiation at random positions of Kapton are modeled. For changing the amount of energy transfer to Kapton, each electron beam is irradiated for 1fs or 2fs. The temperature evolution and chemical composition changes in Kapton during and after electron beam irradiation was studied. The changes in chemical composition of Kapton are compared to the experimental results. This study shows that the time of each electron beam irradiation has considerable effect on the amount of energy transferred to Kapton. Kapton decomposition takes place at different Kapton temperatures under different electron irradiation conditions. At the start of decomposition, small molecules separate from the surface and with continuing electron irradiation, larger molecules start to separate from the surface.

As our simulations demonstrate, ReaxFF can provide a cost-effective screening tool for future material optimization for applications in extreme environments.

## Table of Contents

List of Figures .....	ix
List of Tables .....	xii
Acknowledgement.....	xiv
1. Introduction .....	1
1.1 Atomic Oxygen impact on spacecraft materials.....	2
1.2 Ice cluster impact on spacecraft materials.....	5
1.3 Study of thermal conductivity of ice clusters after deposition on the silica surfaces .....	7
1.4 Study of defects in graphene caused by Kr irradiation .....	9
1.5 Study of Kapton decomposition caused by electron beam irradiation .....	11
2.The ReaxFF Reactive force field molecular dynamics simulation program .....	13
2.1 Molecular Dynamics Method .....	13
2.2 The ReaxFF, Reactive Force Field Method .....	15
3. Disintegration of Kapton, POSS Polyimide, Amorphous Silica and Teflon During Atomic Oxygen Impact.....	21
3.1Methods.....	22
3.1.1 Slabs preparation .....	22
3.1.2 Simulation steps.....	24
3.2 Results on AO impact simulations .....	25
3.2.1 AO impact .....	25
3.2.2 Heat transfer effects .....	31
3.2.3 The effect of different Silica ratios in Kapton-POSS.....	33
4. Ice Cluster Impacts on Amorphous Silica .....	37
4.1 Method description .....	38
4.2 Simulation results .....	41
4.2.1 Ice cluster impacts products.....	41
4.2.3 Multiple ice cluster impacts.....	45
4.2.3 Ice cluster impacts on the silica surfaces which are completely covered with ice layers.....	48
4.3 The possibility of electron excitation.....	50
5. Study of thermal conductivity of ice clusters after impact deposition on the silica surfaces.....	52
5.1 Simulation model and method .....	54

5.1.1 Ice cluster impact simulations .....	54
5.1.2 The dual thermostat method .....	57
5.2 Simulation results .....	59
5.2.1 Thermal conductivity of amorphous and crystal ice clusters .....	59
5.2.2 TC values of crystal and amorphous ice clusters after second impacts on the silica surfaces ..	65
5.2.3 Influence of adding ionic 1-Butyl-3-methylimidazolium (BMIM) in the bulk of the amorphous ice cluster on the ice cluster TC value.....	69
6. Defect formation in graphene under noble gas ion irradiation .....	71
6.1. Defect structures in graphene .....	72
6.2 Computational Method.....	74
6.3 Kr irradiation on graphene simulations results .....	76
7. Electron-induced degradation of Kapton.....	78
7.1 Method description .....	79
7.2 Electron beam irradiation on Kapton results and discussions .....	81
8. Conclusions .....	86
References .....	92

# List of Figures

Figure 1. $(\text{SiO}_{1.5})_n$ , $n=8$ cage used in Kapton-POSS structure. The yellow atoms represent Si and the red atoms represent O.....	3
Figure 2. Molecular dynamics algorithm.....	14
Figure 3. ReaxFF in the computational chemical hierarchy[90].....	15
Figure 4. Schematic overview of ReaxFF force field development[90].....	16
Figure 5. Preparation of Kapton structure . In this preparation, 30 Kapton monomers are put together in an amorphous configuration. There are 1230 total atoms in the structure. The gray atoms represent C and the red atoms represent O and the blue atoms represent N and the white atoms represent H .....	23
Figure 6. Preparation of the Kapton-POSS structure. In this preparation, 20 Kapton-POSS monomers are put together in an amorphous configuration. There are 2120 total atoms in the structure. The gray atoms represent C and the red atoms represent O and the blue atoms represent N and the white atoms represent H and the yellow atoms represent Si .....	23
Figure 7. Preparation of the Teflon structure. In this preparation, 5 Teflon monomers are put together in an amorphous configuration. There are 2200 total atoms in the structure. The gray atoms represent C and the green atoms represent F.....	23
Figure 8. Preparation of the Silica structure with 2600 atoms. Putting 130 $\text{Si}_8\text{O}_{12}$ cages at low density in the big enough box and slowly compressing the system. The final structure is one big molecule. The red atoms represent O and the yellow atoms represent Si.....	24
Figure 9. Steps used in the AO collision simulations.....	25
Figure 10. Key snapshots of AO collisions on Silica, Kapton, POSS and Teflon materials.....	26
Figure 11. Temperature evolution of Kapton, Kapton-POSS, Teflon and amorphous silica under AO impact (NVE simulations).....	28
Figure 12. Total mass of the Kapton, Kapton-POSS, Teflon and amorphous silica slabs under AO impact(NVE simulations) .....	30
Figure 13. Normalized slab mass changes of the Kapton, Kapton-POSS, Teflon and amorphous silica slabs obtained by dividing the remaining slabs mass by the initial mass of the slabs.....	30
Figure 14. Temperature evolution of the Kapton,POSS and Silica during AO impact in NVE and NVT simulations. All the thermostats show the same performance for such systems. Therefore, the graphs for thermostats are on top of each other .....	32
Figure 15. Total mass of the light weight molecules coming off the surface of the Kapton-POSS during AO impact. All the thermostats show the same performance for such systems. Therefore, the graphs for thermostats are on top of each other .....	33
Figure 16. Two different monomers used for building two Kapton-POSS structures with different silicon contents. Using the left monomer can provide higher silicon content inside the material, provided that both final structures will have the same total number of atoms .....	34
Figure 17. Total remaining mass of the two Kapton-POSS structures with different Si contents during AO impact.....	35
Figure 18. Normalized slab mass changes of the Kapton-POSS with different Si contents obtained by dividing the remaining slabs mass by the initial mass of the slabs .....	35

Figure 19. Temperature evolution of the Kapton-POSS with different Si contents during AO impact in NVE simulations .....	36
Figure 20. Configuration of the ice clusters including 150 water molecules for amorphous ice and 128 water molecules for crystal ice clusters and equilibrated at the initial temperature of 150K .....	40
Figure 21. Separating the fragments bouncing back from the surface after ice cluster impact .....	41
Figure 22. Distribution of the molecules separating from the silica surface at different amorphous ice cluster impact velocities .....	44
Figure 23. Average number of O and H atoms of ice cluster remaining on the silica surface after first impact. 1: Amorphous ice impacts on suboxide silica, 2: Amorphous ice impacts on fully oxidized silica, 3: Crystal ice impacts on suboxide silica, 4: Crystal ice impacts on fully oxidized silica.....	45
Figure 24. Multiple ice cluster impacts on the silica surfaces. After each impact the fragments which bounce back from the surface are removed from the simulation system .....	47
Figure 25. Amorphous and crystal ice cluster impacts on the silica surfaces that are completely covered with ice layers .....	49
Figure 26. Average temperature evolution of ice clusters during impact on the fully oxidized and suboxide silica surfaces at amorphous ice impact velocities of 1km/s and 10 km/s. The number of molecules observed in each temperature range at the time that maximum temperature is observed inside the ice cluster during the collisions is shown in the left side histograms .....	51
Figure 27. RDFs in SiO <sub>2</sub> silica shown for Oxygen-Oxygen O–O, Silicon-Silicon Si–Si, and Silicon-Oxygen Si–O .....	55
Figure 28. Snapshots of crystal ice cluster- silica impact simulation. The crystal ice impacts on the fully oxidized silica surface at two different impact velocities - 500m/s and 1 km/s .....	57
Figure 29. Schematic of the system for calculation of the ice TC after ice deposition on the silica surface .....	59
Figure 30. Temperature profile, T(z), as a function of the z coordinate for amorphous ice after reaching steady state condition .....	62
Figure 31. RDF graphs of crystal ice cluster before and after 1km/s impact on the surface of fully oxidized silica. These graphs are for the lower half of the ice crystal that has interface with silica surface after impact.....	64
Figure 32. RDF graphs of the crystal ice cluster before and after 1km/s impact on the surface of suboxide and fully oxidized silica. These graphs are for lower half of the ice crystal that has interface with silica surface after impact .....	64
Figure 33. First and second impacts of crystal ice on suboxide silica surface at 500 m/s and 1 km/s impact velocities.....	66
Figure 34. Side view of first and second impacts of crystal ice on suboxide silica surface at 500 m/s and 1 km/s impact velocities.....	66
Figure 35. RDF graphs of the top and bottom layers of crystal ice cluster after two successive 1km/s impacts on the surface of suboxide silica .....	67
Figure 36. Amorphous ice cluster mixed with ionic BMIM .....	69
Figure 37. Stone-Wales defect in graphene.....	73
Figure 38. Mono Vacancy defect in graphene .....	73
Figure 39. Some common types of double vacancy defects in graphene .....	73

Figure 40. Some common types of Frenkel defects in graphene.....	74
Figure 41. Force field training results of Carbon-Krypton interactions.....	75
Figure 42. Adatoms distribution from their original lattice position after He <sup>+</sup> irradiations on graphene..	77
Figure 43. Adatoms distribution from their original lattice position after Kr <sup>+</sup> irradiations on graphene...	77
Figure 44. Initial configuration of Kapton at the start of electron beam irradiation .....	80
Figure 45. Random locations of electron beam irradiation on Kapton .....	80
Figure 46. Electron beams irradiations on Kapton ReaxFF molecular dynamics simulation procedure ....	81
Figure 47. Temperature evolution of Kapton during 30 electron beam irradiation. Each electron beam is turned on for 1 fs. Each point on the graph is the time that on electron beam is irradiated. ....	82
Figure 48. Temperature evolution of Kapton during 25 electron beam irradiation. Each electron beam is turned on for 2 fs. Each point on the graph is the time that on electron beam is irradiated. ....	82

# List of Tables

Table 1 The conditions of some of the experimental studies on irradiation of Kapton .....	11
Table 2 Chemical compositions of the materials separating from the surface of Kapton, POSS and Silica materials at the first stages of AO impacts .....	29
Table 3 Erosion yield results of Kapton and Teflon AO collision simulations .....	31
Table 4 The numbers of different atoms in two different Kapton-POSS structures .....	34
Table 5 The molecules bouncing back from the silica surfaces after ice cluster impacts. Each data point is the average value of three separate simulations with similar initial conditions .....	43
Table 6 Normalized number of water molecules which dissociate after ice cluster impacts. Each data point is the average value of three separate simulations with similar initial conditions .....	45
Table 7 Number of H and O atoms accreting on the fully oxidized and suboxide silica surfaces after crystal and amorphous ice cluster impacts. Each data point is the average value of three separate simulations with similar initial conditions .....	46
Table 8 Sticking coefficients for crystal and amorphous ice clusters .....	48
Table 9 Number of H and O atoms accreting or separating after second crystal and amorphous ice cluster impacts on the silica surfaces that are completely covered with ice layers .....	50
Table 10 Characteristics of fully oxidized and suboxide amorphous silica structures .....	55
Table 11 ReaxFF and experimental values of the thermal conductivity of amorphous and crystal ice .....	60
Table 12 ReaxFF and experimental values of the thermal conductivity of fully oxidized and suboxide silica .....	61
Table 13 ReaxFF values of the thermal conductivity of amorphous ice depositing on the fully oxidized silica surface with or without initial impact velocity on the silica surface .....	62
Table 14 ReaxFF values of the thermal conductivity of amorphous ice depositing on the suboxide silica surface with or without initial impact velocity on the silica surface .....	62
Table 15 ReaxFF values of the thermal conductivity of crystal ice depositing on the fully oxidized silica surface with or without initial impact velocity on the silica surface .....	63
Table 16 ReaxFF values of the thermal conductivity of crystal ice depositing on the suboxide silica surface with or without initial impact velocity on the silica surface .....	63
Table 17 ReaxFF values of the thermal conductivity of amorphous ice depositing on the fully oxidized silica .....	67
Table 18 ReaxFF values of the thermal conductivity of amorphous ice depositing on the suboxide silica .....	68
Table 19 ReaxFF values of the thermal conductivity of crystal ice depositing on the fully oxidized silica surface .....	68
Table 20 ReaxFF values of the thermal conductivity of crystal ice depositing on the suboxide silica surface .....	68
Table 21 ReaxFF values of the thermal conductivity of amorphous ice containing ionic BMIM depositing on the silica surface .....	70
Table 22 Percentage of different defects in the $Kr^+$ irradiated graphene .....	76

Table 23 Molecular composition of Kapton structure at the start of simulations.....	82
Table 24 Molecular composition of Kapton structure at the end of 1fs irradiations simulation .....	83
Table 25 Molecular composition of Kapton structure at the end of 2fs irradiations simulation .....	83
Table 26 Atomic masses of the observed peaks at different times in five different atomic mass unit (amu) regions after low energy electron beam irradiation experiment .....	85

# Acknowledgement

I would like to express my sincere gratitude to my advisor professor van Duin for all his patience, support and willingness to share his knowledge and experience through the course of my PhD studies. I specially will always be thankful for his trust and support at all the stages of my PhD career. He has been a constant source of motivation and inspiration.

I also would like to thank my family for their endless love and support. All that I have achieved in my life is mainly because of their support and motivation. I always shall remain indebted to them.

Finally, I would like to thank the Penn State University for giving me the opportunity to pursue my graduate studies at this great university.

# 1. Introduction

The materials on the surface of the spacecraft and in some cases the materials on the surface of aircraft will be exposed to very high velocity impacts by atomic Oxygen, ice clusters, high energy ions, radiation and many other hypervelocity impacts during the missions. Hypervelocity refers to velocities in the range of a few kilometers per second to some tens of kilometers per second. This is especially relevant in the field of space exploration, where hypervelocity impacts can result in anything from minor component degradation to the complete destruction of a material.

Atomic Oxygen (AO), which is the most abundant in Low Earth Orbital (LEO), impacts on the spacecraft surface materials at average impact energy around 4.5 eV. Materials used on the surface of the spacecraft, like Kapton polymer, have shown to be damaged by the effect of the AO or electron irradiation.

Graphene is also an important material which has recently found significant applications. Carbon fiber/epoxy composite materials are often used as structural components in aerospace applications. These materials show relatively favorable specific mechanical properties. Graphene nanoplatelets can be included in the epoxy matrix to improve the overall mechanical properties of the composite [1-4]. The effect of hypervelocity gas ion impacts on the surface of graphene is another point of interest in this study.

Another important concept is hypervelocity molecular cluster impacts on various materials. Cluster impacts with collision velocities up to 17 km/s have been observed at space environment. Ice cluster impacts and the consequent ice accumulation on the silica surface are studied in this

work. The thermal conductivity of the accumulated ice is an important parameter that should be evaluated in order to obtain better understanding of accumulated ice removal process.

In this thesis, we describe various applications of the ReaxFF reactive force field to study material response in extreme environments. Each of these applications is described in the following sections.

## **1.1 Atomic Oxygen impact on spacecraft materials**

The Low Earth Orbital (LEO) environment subjects materials on the surface of a spacecraft to  $\sim 4.5$  eV collisions with AO (Atomic Oxygen) and to  $\sim 8$  eV collisions with ambient  $N_2$  molecules[5]. Such collisions cause the surface degradation of these materials. There have been many efforts to protect these materials by using non-volatile metal oxides on the surface and in the bulk of the material. For enhancing the brittleness characteristics of such materials, compounds like fluoropolymers metal oxides are applied[6].

At the LEO space exposure condition, the materials used on the surface of the spacecraft are affected by AO. Other parameters that can affect these materials such as ultraviolet radiation (UV), micrometeoroids, debris and thermal cycling are important to be considered. Simultaneous exposure of such materials to AO and UV radiation can dramatically increase the amount of the degradation[7]. The impact of UV radiation is especially experienced on Teflon materials used on the surface of spacecraft[8].

One of the most common materials used on the surface of spacecraft is Kapton. Kapton is a polyimide film which can remain stable in a wide range of temperatures, from 0 – 673 K. The

main reasons for the interest in Kapton application on the spacecraft surface are the light weight, temperature stability, insulation characteristics and UV stability of this material[9, 10].

For enhancing the stability and mechanical properties of Kapton, silicon oxide compound can be added to the material. Polyhedral oligomeric silsesquioxanes are molecules with the chemical composition  $(\text{RSiO}_{1.5})_n$  which are used in the space applications. The most common composition is the composition of  $n=8$  which is shown in the figure 1.

While oxidation is taking place in Kapton and Kapton-POSS under AO impacts, various molecules start to separate from the materials. Many of the small separating molecules are Carbon containing molecules. Therefore, the AO collision can erode the surface of these materials.

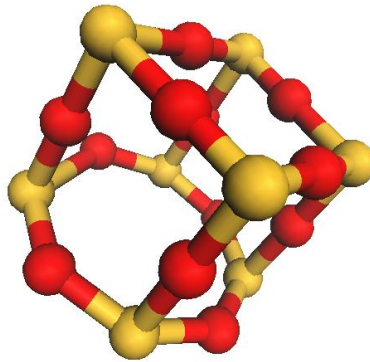


**Figure 1.  $(\text{SiO}_{1.5})_n$ ,  $n=8$  cage used in Kapton-POSS structure. The yellow atoms represent Si and the red atoms represent O**

Teflon is another important material used on spacecraft. The main usage of Teflon is protection from solar heating. However, the drawbacks of using Teflon in such applications can be erosion and cracking of this material[6].

In this research, atomistic scale simulations of surface degradation of Kapton, Kapton-POSS, amorphous silica and Teflon, which are among the most common materials used on the surface of the spacecraft, under AO collision are evaluated.

For performing these simulations, the ReaxFF reactive force field program was used. This classical force field can provide the computational requirements to perform reactive molecular dynamics simulations on relatively large (>1000 atoms) systems. Therefore, we will be able to describe the full chemistry of the reactions using this program.

ReaxFF is a general bond-order-dependent force field that provides reasonable descriptions of bond breaking and bond formation [11-19]. The main difference between traditional non-reactive force fields and ReaxFF is that in ReaxFF the connectivity is determined by bond orders calculated from interatomic distances that are updated every MD simulation step. This allows for bonds to break and form during the simulation. In order to account for nonbonded interactions such as van der Waals and Coulomb interactions for a system with changing connectivity, these interactions are calculated between every pair of atoms, irrespective of connectivity, and any excessive close-range nonbonded interactions are avoided by inclusion of a shielding term. In addition, ReaxFF accounts for polarization effects by using a geometry-dependent charge calculation scheme. A more complete description of the ReaxFF methods and its implementation in molecular dynamics simulations is given in Chapter 2 of this thesis. The results of the AO impact work is described in Chapter 3 of this thesis.

## 1.2 Ice cluster impact on spacecraft materials

High velocity collisions between the clusters - like water nanodroplets- and materials have received significant attention recently due to their relevance for both fundamental and applied research [20-33]. While there have been many investigations on high energy collisions of different types of atoms on different materials [34-38], due to the complex nature of the cluster-surface interactions, a thorough understanding of such impacts is not available yet.

The complications in the simulations of such interactions are related to the high energy transfer to the surface and the changes in the colliding cluster during the collision. During these types of collisions, different phenomena, like reaction inside the colliding cluster, mass gain or mass loss at the surface might happen. At very high velocity collisions, electron excitation can happen and for capturing the correct behavior of the materials, considering electron excitation might be necessary.

Collisions of clusters on the surface of spacecraft can happen at velocities of up to 17 km/s and such collisions can cause thermal activation chemistry with the time scale of the order of vibrations of the nuclei. This means that at such impacts the activation process is thermal and it takes place on a very short time scale. During impact, high relative velocities and high densities for the cluster take place and the dynamics of such condition should be considered.

The important parameter in these impacts is the stopping force exerted on the colliding species. This stopping force is a function of the speed for colliding species, but because of the dependence of the stopping force on the shape of the clusters and the change in the shape of the clusters, the relation between the stopping force and cluster velocity is quite complex.

External kinetic energy is the energy of the clusters as a moving mass while internal kinetic energy is measured in a coordinate system which moves with the clusters center of mass and it is associated with the particles thermal motion. Therefore, the kinetic temperature corresponding to the total kinetic energy of the cluster is divided into two parts, namely thermal temperature and translational temperature. In this study we focus on the effects of external kinetic energy on the cluster-surface interactions during the impacts.

Due to the complexity of the dynamics of these interactions, a straightforward interpretation of experimental results is usually not possible. However, these phenomena can be studied using classical molecular dynamics simulations, which provide a powerful tool in understanding the dynamics of cluster surface collisions.

These investigations can help better understanding of physical and physicochemical behavior of materials under extreme conditions of pressure and temperature.

The first simulations and experiments related to cluster-surface collisions were mostly focused on metal clusters and rare gases [39-41]. However, recent theoretical and experimental research includes a larger variety of materials [42-47].

One of the important parameters which should be considered in the cluster-surface collisions is the ratio of total kinetic energy to total binding energy of the cluster. The important role of this parameter has been shown in earlier studies[22]

Although many efforts have been put in understanding the cluster-surface collision phenomena, still many parameters that can play important role in this field should be studied in more detail in different length and time scales. In this study we will try to shine more light on different aspects of these phenomena which can take place at the extreme conditions. Particularly, for ice cluster

impacts, the effect of cluster impact velocity on the amount of ice accumulation and the subsequent change in structure of the ice cluster will be studied.

Silicon-based compounds are widely used at different parts of spacecraft and aircraft like coatings, seals and photovoltaic parts. The performance of silicon-based materials at space conditions has been widely studied. Coatings obtained by sputter deposition of fully oxidized and suboxide silica have been used on the surface of spacecraft [48]. Because of the widespread applications of these materials on the spacecraft, fully oxidized and suboxide silica structures have been selected here to study the effects of hypervelocity ice cluster collisions. This can be extended to the study of ice clusters impacting on other materials such as aluminum or polymer composites. The results of the ice cluster impact studies are described in Chapter 4 of this thesis.

### **1.3 Study of thermal conductivity of ice clusters after deposition on the silica surfaces**

For aircraft and spacecraft, ice accumulation can be problematic both during flight and during take-off. Especially for aircraft, the ice accretion can decrease the lift and cause the pilot to lose control. When water droplets, which can be super-cooled to  $-40^{\circ}\text{C}$ , impact on the cold aircraft surface, they can freeze and accumulate[49]. Ice is a source of debris from the external fuel tank of the spacecraft that can be released during launch and has the potential to cause damage to the spacecraft surface elements.

The thermophysical properties of ice which is deposited on the surface play a key role in the physics of heat conduction. There have been significant amounts of studies on thermophysical properties of materials. These studies have been conducted on materials

with different complexities and different calculations methods have been applied in thermal conductivity (TC) calculations [50-68].

The dominant contributors to the concept of thermal conductivity in ice clusters are phonons. Therefore, several methods have been developed to capture the phonon effect in predicting TC[69, 70]. Various different approaches have been applied in the calculation of TC of materials. One of the most straightforward methods applied in determination of TC is direct method[71, 72]. In the direct method, the TC is calculated as the ratio of an imposed heat flux to the resulting temperature gradient. The heat flux is imposed by adding kinetic energy from hot side and withdrawing kinetic energy from cold side of the system. Another method for computation of TC is the Green–Kubo method[73]. In this method, the TC is calculated in terms of the integral of correlation functions. This method uses the fluctuations of the heat current in a homogeneous equilibrium system to calculate the TC applying linear response theory. Other methods include the thermal diffusion method[74], Evans homogeneous field method[75]and Boltzmann transport equation[76]. At the nano-scale, molecular structure of the materials and surfaces, and the interactions between them at the atomistic length scales play a key role in the heat transfer performance. Therefore, the molecular dynamics (MD) method emerges as a valuable method for investigation of the heat transfer in such scales. One of the objectives of this study is to use MD simulations to identify the relationship between the ice structure at the silica interface and its thermal transport properties. Because MD simulation provides the ability to obtain the detailed information on atomic level and the associated dynamics of the structure, it is used for the atomic level evaluation of the thermal transport characteristics. The force field used for these simulations has been already developed for

silica-ice interface [77] and can successfully describe water-dissociation and proton-transfer events at this interface, which can substantially affect the water/silica contact and affiliated thermal transfer.

Using ReaxFF reactive force field method, equilibrium and non-equilibrium molecular dynamics (EMD and NEMD) can be used to determine the thermal conductivity of materials. In EMD method, an equilibrated system is used and the TC value is calculated with application of statistical averaging. In NEMD method, the TC value is calculated using monitoring of cooling/heating rates. The EMD and NEMD approaches are reliable alternatives to the traditional Green-Kubo method[78]. The results of this thermal conductivity study are described in Chapter 5 of this thesis.

#### **1.4 Study of defects in graphene caused by Kr irradiation**

The discovery of graphene has brought some of the most exciting properties of materials in technological applications. It is made by isolating single two dimensional atomic layers of graphite. The strongest bond in nature, the C-C bond covalently locks these atoms in place resulting in remarkable mechanical properties [79-81]. A suspended single layer of graphene is one of the stiffest known materials characterized by a remarkably high Young's modulus of  $\sim 1$  TPa[82]. Graphene is five times stiffer and two orders of magnitude stronger than steel. Graphene shows great heat dissipation[83] and the capability to bear large current density[84]. Therefore, the last decade has witnessed the flourishing of graphene in many areas from fundamental science to practical applications.

Functionalized graphene like graphene oxide which can be produced in large scale contrary to pristine graphene, which production is still limited to laboratory scale quantities retains enough conductivity to function as an electrostatic charge dissipation layer in space structures.

Loss of propellant through boil-off from cryotanks used for in-space propulsion is a significant problem in long-duration missions. Development of high-performance gas-barrier coatings using functionalized graphene can help in reducing this fuel loss. Proper dispersion of the two-dimensional graphene nanoparticles in a composite material can greatly reduce propellant loss [85].

The examples of graphene applications for space applications described above can provide some hints of graphene applications that, in the near term, could enhance current technology in space industry, and, in the long term, could enable revolutionary concepts which are not possible now.

Defects can deteriorate the useful properties of graphene based materials in extreme environments. However, a pristine graphene is not always necessary or even desirable. Careful manipulation of graphene structure via ion irradiation can be used to tailor the properties. In this study, defect formation via energetic noble gas irradiation in graphene is investigated. In order to study defect formation under noble gas irradiation in graphene, an extensive set of reactive molecular dynamics simulations have been conducted.

In this study, the atomistic scale details of Kr ion impacts causing defect formation and the associated dynamic processes involved in the irradiations and during subsequent relaxation are analyzed. The results of the Kr-impact study on graphene are described in Chapter 6 of this thesis.

## 1.5 Study of Kapton decomposition caused by electron beam irradiation

Kapton polyimide can be exposed to high-energy electrons, protons, heavy ions, vacuum ultraviolet and cosmic radiations in space environment. In the geosynchronous orbit, high energy electrons and protons are the main radiation factors in this environment. Under these conditions, major structural transformations in the Kapton, such as chain scission and cross-linking events can take place. These transformations can result in changes in the properties of the polymer like thermal conductivity, dielectric constant, etc. The concentration of the aromatic groups can offer protection against structural damage on exposure to electron or gamma irradiations[86].

Furthermore, radiation processing has emerged as a time saving and easy-to-control method to bring about desired modifications in polymers. Among several types of radiations that can be used for radiation processing, high-energy electrons are of particular interest for polymers, due to their high dose rates and consequently high-energy deposition in small time intervals.

There are a very few studies on evaluating the effects of radiation on mechanical and the structural properties of polyimides [87, 88].

Due the importance of Kapton in aerospace applications, many experiments investigating the exposure of Kapton to ionizing radiation have been conducted over the last decade. Some of such studies that mostly have been studied by irradiation of heavy atoms are mentioned in Table 1.

Table 1 The conditions of some of the experimental studies on irradiation of Kapton

Reference	Particle	Energy/eV
Li et al. (2007)	H <sup>+</sup>	$5.0 \times 10^4$
Sun et al. (2002)	Si <sup>+</sup>	$3.0 \times 10^6$
Virk et al. (2001)	C <sup>5+</sup>	$7.0 \times 10^7$
Sharma et al. (2005)	Li <sup>3+</sup>	$5.0 \times 10^7$

Electron irradiation is another important type of irradiation that should be studied in more details. Experimental studies show that electron beams penetrate to a certain depth in Kapton and the energy of the electron beam gets dissipated in the bulk of Kapton [89]. These results show that simulation of electron beams inside Kapton with stationary charged particles can be a reasonable assumption.

Therefore, in the present work, we recently developed a new, ReaxFF-based, framework for studying electron beam damage in polymers. In this study, electron beams are modeled with some charged particles inside the Kapton structure. Each electron beam is modeled with a string of dummy atoms along the Kapton structure. In order to model this string of dummy atoms as an electron beam, a charge of -1 is added to each dummy atom. When it is time to turn off this particular electron beam, the charges of dummy atoms are changed back to zero value. Using this method, we could model an electron beam at each random location of Kapton. We can model the energy transfer by electron beam to the bulk of Kapton. Using this framework, the effect of electron irradiation and the electron energy transfer to the Kapton structure and the consequent changes in Kapton structure are evaluated using reactive molecular dynamics simulations. The results from this study are described in Chapter 7 of this thesis.

## **2.The ReaxFF Reactive force field molecular dynamics simulation program**

### **2.1 Molecular Dynamics Method**

Molecular dynamics (MD) is a popular simulation method by which we can calculate the interactions between the atoms and using these calculated interacting forces, the positions of the atoms inside the system can be updated at each time step of the simulation. These predictions are obtained using classical Newton's laws of motion. This is a simplification of the interaction between atoms and considering the atoms interacting based on classical Newton's laws. This is based on the assumption that atoms behave as classical particles. Though this is not exactly accurate; but vast studies have found that this assumption work well for many elements.

In order to calculate the amount of the interactions between atoms, the related potentials are used. These potentials are known as force field in molecular dynamics simulations. These force fields are developed based on training the associated parameters using the experimental and quantum mechanics simulations results.

Force fields can be categorized in two classes

- Non-reactive force fields
- Reactive force fields

Non-reactive force fields cannot simulate chemical bond formation or chemical bond breakings. However, this category of force fields can be used for simulating many systems at equilibrium. For performing the simulations of the systems far away from equilibrium, reactive force field should be used that incorporate bond order concept in calculating the associated potential energies. These reactive force fields can be used in non-equilibrium simulations used for calculation of some important properties of materials (E.g thermal conductivity). Obviously, the amount of computations for simulations using reactive force field is much higher than the simulations using non-reactive force fields. The molecular dynamics algorithm is shown in Figure 2.

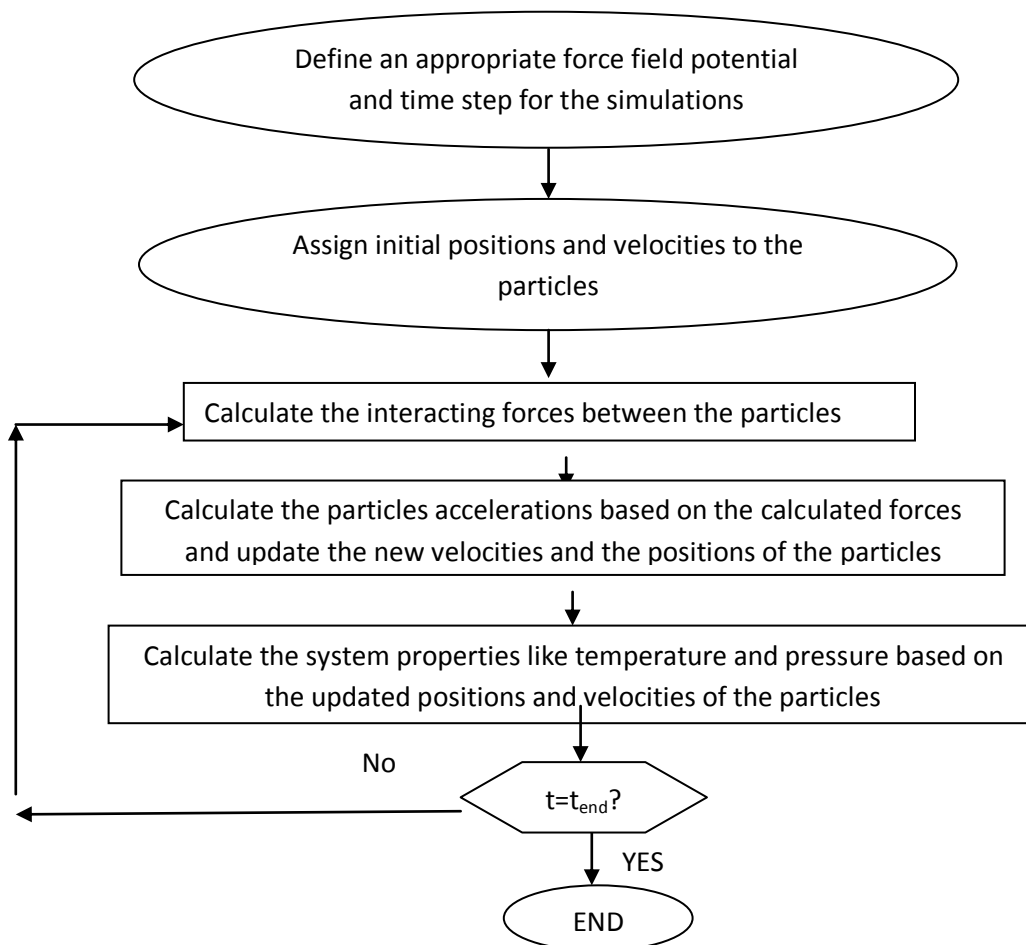


**Figure 2. Molecular dynamics algorithm**

## 2.2 The ReaxFF, Reactive Force Field Method

ReaxFF reactive force field molecular dynamics program has been used for performing the simulations in this study. ReaxFF can provide the computational requirements to perform molecular dynamics simulations on systems which are sufficiently large to describe the full chemistry of the reactions. The ReaxFF reactive molecular dynamics program was developed based computational chemical methods to bridge the gap between quantum chemical (QC) and empirical force field (EFF). (Figure 3)

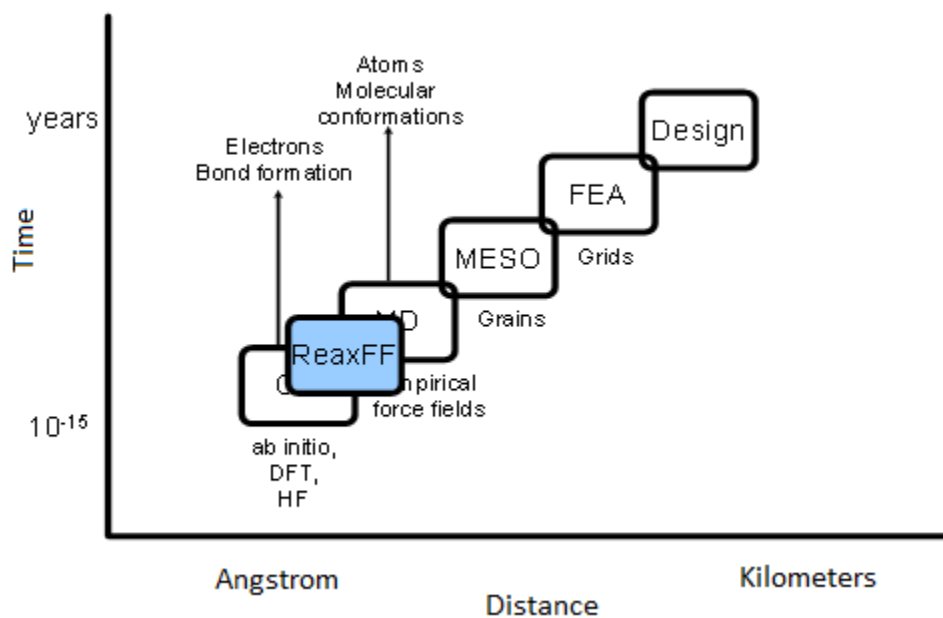


Figure 3. ReaxFF in the computational chemical hierarchy[90]

ReaxFF is a general bond-order-dependent force field that provides reasonable descriptions of bond breaking and bond formation. The main difference between traditional non-reactive force fields and ReaxFF is that in ReaxFF the connectivity is determined by bond orders calculated

from interatomic distances that are updated every MD simulation step. This allows for bonds to break and form during the simulation. In order to account for nonbonded interactions such as van der Waals and Coulomb interactions for a system with changing connectivity, these interactions are calculated between every pair of atoms, irrespective of connectivity, and any excessive close-range nonbonded interactions are avoided by inclusion of a shielding term. In addition, ReaxFF accounts for polarization effects by using a geometry-dependent charge calculation scheme.

We can consider two major branches for ReaxFF parameters which are developed so far. These branches are combustion and water related. Figure 4 shows these branches and the general parameters shared in these branches and the condition of transferability.

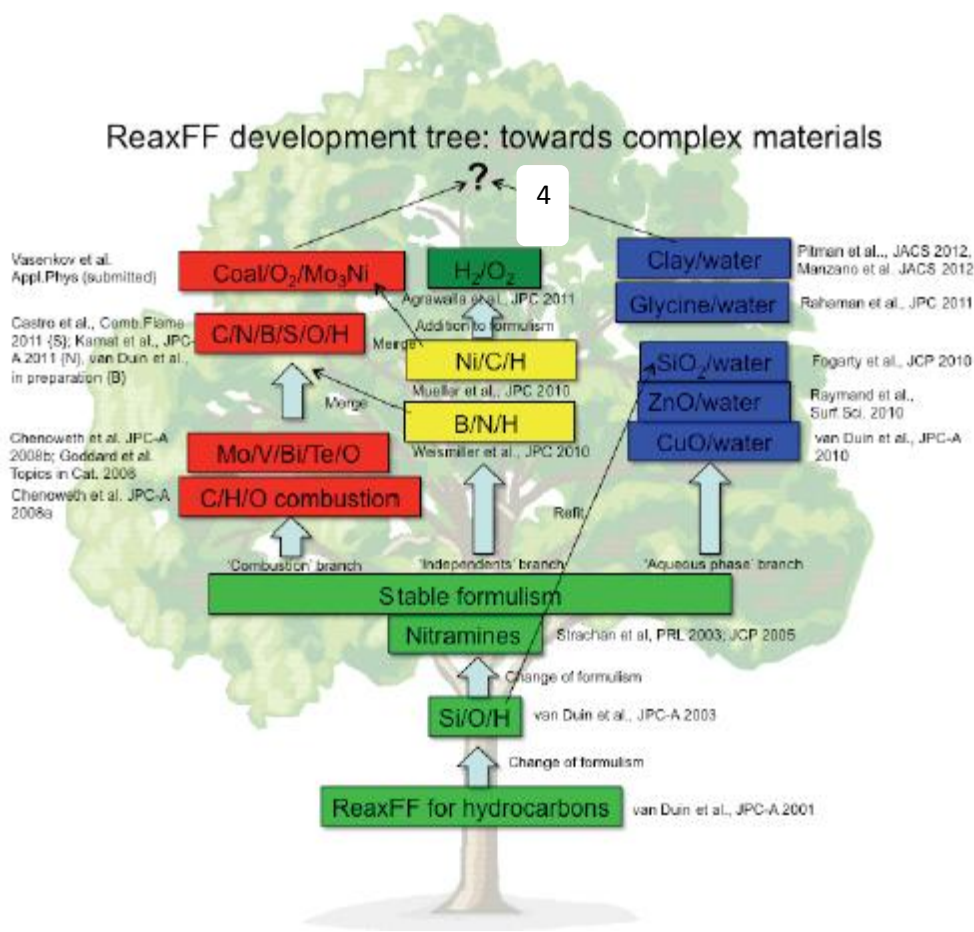


Figure 4. Schematic overview of ReaxFF force field development[90]

In ReaxFF, different energies contribute to the total system energy:

$E_{\text{bond}}$ = bond energies contribution

$E_{\text{over}}$ = penalizing over-coordination contribution

$E_{\text{under}}$ = stabilize under-coordination of atoms contribution (optional)

$E_{\text{lp}}$ = lone-pair energies contribution

$E_{\text{val}}$ =valence angle energies contribution

$E_{\text{coulomb}}$ =non-bonded Coulomb term contribution

$E_{\text{vdw}}$ =van der Waals interaction energy contribution

The total energy will be the sum of these separate terms (equation 1)

$$E_{\text{system}}=E_{\text{bond}}+E_{\text{over}}+E_{\text{under}}+E_{\text{lp}}+E_{\text{val}}+E_{\text{vdw}}+E_{\text{coulomb}} \quad (1)$$

All terms except the last two are bond-order dependent and the bond orders are given by a general relationship between bond-order and inter-atomic distance.

This relationship which distinguishes between contributions from sigma bond, pi bond and double pi bond is shown in equation 2.

$$BO'_{ij}=\exp \left[ p_{\text{bo}, 1} \left( \frac{r_{ij}}{r_0} \right)^{p_{\text{bo},2}} \right] + \exp \left[ p_{\text{bo}, 3} \left( \frac{r_{ij}^{\pi}}{r_0} \right)^{p_{\text{bo},4}} \right] + \exp \left[ p_{\text{bo}, 5} \left( \frac{r_{ij}^{\pi\pi}}{r_0} \right)^{p_{\text{bo},6}} \right] \quad (2)$$

$p_{bo,i}, i = 1$  to 6 are force field parameters and are using experimental and quantum chemistry data the value of these parameters are adjusted through optimization procedures. The first term of the above equation is sigma bond, the second term corresponds to first pi bond and third term refers to second pi bond. The uncorrected over-coordination is calculated for each atom from this uncorrected bond order, which is further used in obtaining the corrected bond order,  $BO_{ij}$ . The corrected bond orders are then used for calculating bond energy which is given by equation (3).

$$E_{\text{bond}} = -D_e^{-\sigma} \cdot BO_{ij}^{\sigma} \cdot \exp[p_{\text{be}1} (1 - (BO_{ij}^{\sigma})^{p_{\text{be}2}}) - D_e^{\pi} BO_{ij}^{\pi} - D_e^{\pi\pi} BO_{ij}^{\pi\pi}] \quad (3)$$

where,  $p_{\text{be}1}$ ,  $p_{\text{be}2}$ ,  $D_e^{\pi}$ ,  $D_e^{\pi\pi}$  are the force field parameters

The lone pair value is obtained by calculating the difference between the total number of electrons in outer shell and the sum of bond orders around the atomic center. The lone pair energy penalty is given by equation 4.

$$E_{\text{lp}} = \frac{p_{\text{lp}2} \Delta_i^{\text{lp}}}{1 + \exp(-75 \times \Delta_i^{\text{lp}})} \quad (4)$$

Where  $\Delta_i^{\text{lp}}$  is the number of lone pairs and  $p_{\text{lp}2}$  is the force field parameter.

In order to calculate valence angle energy, a bond order dependent formulation is utilized. The equilibrium angle  $\theta_0$  for  $\theta_{ikj}$  used in equation (5) depends on the sum of  $\Pi$ -bond orders around the central atom j Valence angle energy can be expressed by

$$E_{\text{val}} = f_7(\text{BO}_{ij}) \times f_7(\text{BO}_{kj}) \times f_8(\Delta_j) \times \left\{ p_{\text{val1}} - p_{\text{val1}} \exp \left[ -p_{\text{val2}} (\Theta_0(\text{BO}) - \Theta_{ijk})^2 \right] \right\} \quad (5)$$

The exact functional forms of  $f_7$  and  $f_8$  can be found in ReaxFF references where  $p_{\text{val1}}$  and  $p_{\text{val2}}$  are force field parameters.

Similar to bond and angle energy terms, the torsion angle energy term is dependent on bond order. This energy term disappears when BO approaches to 0. The torsion angle energy term is expressed in equation 6.

$$E_{\text{tor}} = f_{10}(\text{BO}_{ij}, \text{BO}_{jk}, \text{BO}_{kl}) \times \sin \Theta_{ijk} \times \sin \times \left[ \frac{1}{2} V_1 \cdot (1 + \cos \omega_{ijkl}) + \frac{1}{2} V_2 \times \exp \left\{ p_{\text{tor1}} \left( \text{BO}_{jk}^\pi - 1 + f_{11}(\Delta_j, \Delta_k) \right)^2 \right\} \right. \\ \left. (1 - \cos 2\omega_{ijkl}) + \frac{1}{2} V_3 (1 + \cos 3\omega_{ijkl}) \right] \quad (6)$$

The distance-corrected Morse potential is chosen for calculating the van der Waals interactions. In order to avoid excessive high repulsions between bonded atoms and atoms sharing a valence angle, the shielded interaction is considered in the calculations.

$$E_{\text{vdWaals}} = \text{Tap} \times D_{ij} \times \left\{ \exp \left[ \alpha_{ij} \left( 1 - \frac{f_{13}(r_{ij})}{r_{\text{vdW}}} \right) \right] - 2 \times \exp \left[ \frac{1}{2} \alpha_{ij} \left( 1 - \frac{f_{13}(r_{ij})}{r_{\text{vdW}}} \right) \right] \right\} \quad (7)$$

Where  $\text{Tap}$  is a taper term which avoids discontinuities when charged species move in and out of the non-bonded cutoff radius.

$$f_{13}(r_{ij}) = \left[ r_{ij}^{P_{\text{vdW}}} + \left( \frac{1}{\gamma_w} \right)^{P_{\text{vdW}}} \right]^{\frac{1}{P_{\text{vdW1}}}} \quad (8)$$

Coulomb interactions are calculated for each pair of atoms. A shielded Coulomb-potential is used to adjust orbital overlap between atoms at close distance. The Electron Equilibrium Method (EEM) is used for the calculation of atomic charges.

$$E_{\text{coulomb}} = \text{Tap.C.} \frac{q_i q_j}{\left[ r_{ij}^3 + \left( \frac{1}{\gamma_{ij}} \right)^3 \right]^{1/3}} \quad (9)$$

### **3. Disintegration of Kapton, POSS Polyimide, Amorphous Silica and Teflon During Atomic Oxygen Impact**

At the LEO space exposure condition, the materials used on the surface of the spacecraft are affected by AO. Other parameters that can affect these materials such as ultraviolet radiation (UV), micrometeoroids, debris and thermal cycling are important to be considered for LEO exposure conditions. Simultaneous exposure of such materials to AO and UV radiation can dramatically increase the amount of the degradation. The impact of UV radiation is especially experienced on Teflon materials used on the surface of spacecraft.

In this research, atomistic scale simulations of surface degradation of Kapton, Kapton-POSS, amorphous silica and Teflon, which are among the most common materials used on the surface of the spacecraft, under collision from AO are evaluated.

For performing these simulations, the ReaxFF reactive force field program was used. This classical force field can provide the computational requirements to perform reactive molecular dynamics simulations on relatively large (>1000 atoms) systems. Therefore, we will be able to describe the full chemistry of the reactions using this program.

## **3.1 Methods**

### **3.1.1 Slabs preparation**

The preparation of the structures of these four materials for the AO collision simulations is depicted in Figures 5-8. In the preparation of these slabs the densities of  $1.3\text{g/cm}^2$ ,  $2\text{g/cm}^2$ ,  $2.62\text{g/cm}^2$  and  $2.2\text{ g/cm}^2$  were obtained for Kapton, Kapton-POSS, silica and Teflon slabs respectively.

For preparing Kapton and Kapton-POSS and Teflon structures, the monomers shown in Figures 5 -7 are used for the polymerization. In the Kapton, Kapton-POSS and Teflon structures, 30, 20 and 5 monomers are used respectively.

For preparing the amorphous silica structure, 71  $\text{Si}_8\text{O}_{12}$  cages are put in a periodic box with initial low density and after that, by slowly reducing the periodic box dimensions, the system is compressed to reach the target density for the silica structure.

The Kapton, Kapton-POSS and Teflon structures are prepared using amorphous cell tool in Material Studio software. The main target in preparing these structures was to construct models that have densities close to the density of these materials under stable conditions. The sizes and lengths of the monomers used to construct these models have been selected arbitrarily. Therefore, these amorphous structures obtained by these methods are not unique.

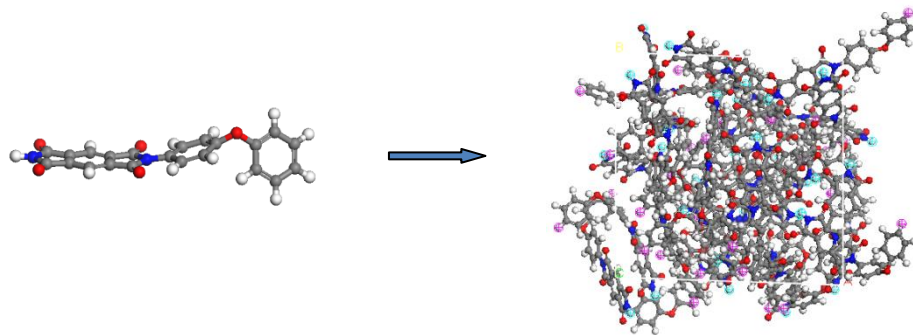


Figure 5. Preparation of Kapton structure . In this preparation, 30 Kapton monomers are put together in an amorphous configuration. There are 1230 total atoms in the structure. The gray atoms represent C and the red atoms represent O and the blue atoms represent N and the white atoms represent H

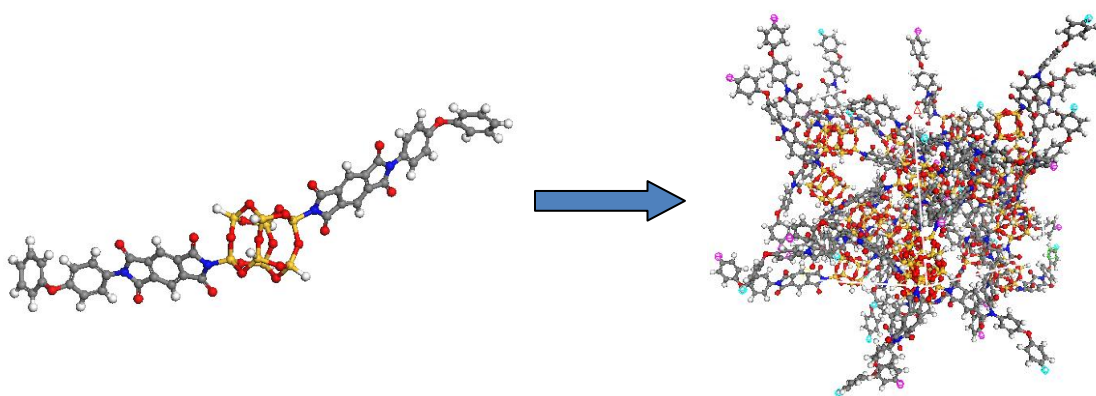


Figure 6. Preparation of the Kapton-POSS structure. In this preparation, 20 Kapton-POSS monomers are put together in an amorphous configuration. There are 2120 total atoms in the structure. The gray atoms represent C and the red atoms represent O and the blue atoms represent N and the white atoms represent H and the yellow atoms represent Si

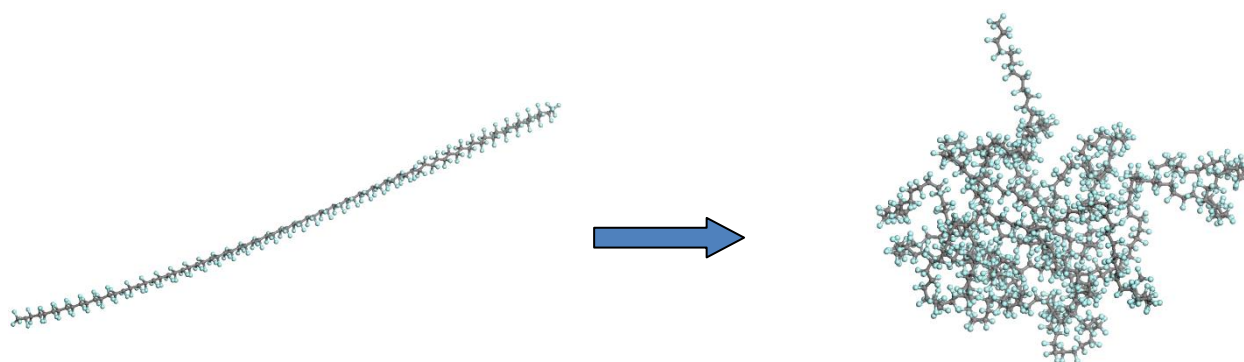


Figure 7. Preparation of the Teflon structure. In this preparation, 5 Teflon monomers are put together in an amorphous configuration. There are 2200 total atoms in the structure. The gray atoms represent C and the green atoms represent F

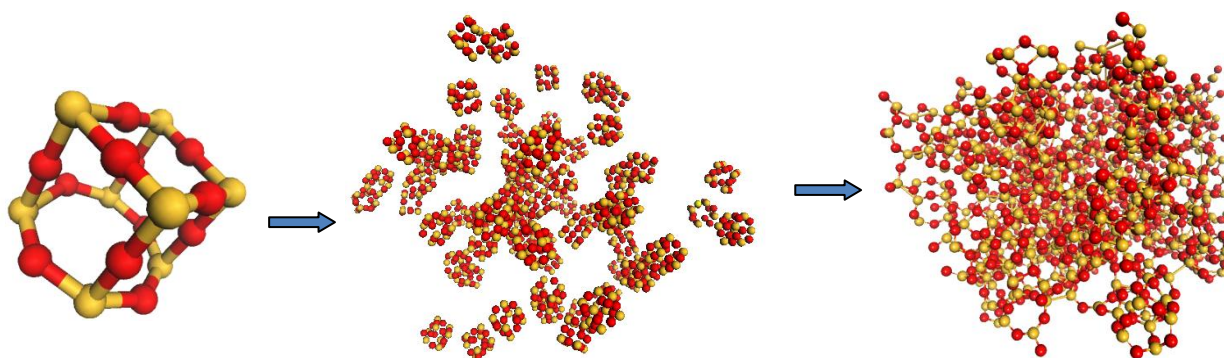


Figure 8. Preparation of the Silica structure with 2600 atoms. Putting 130  $\text{Si}_8\text{O}_{12}$  cages at low density in the big enough box and slowly compressing the system. The final structure is one big molecule. The red atoms represent O and the yellow atoms represent Si

### 3.1.2 Simulation steps

After constructing the structures, the simulation is performed. Each simulation involves four steps. These steps are shown in figure 9. After preparing the structures, using geometry optimization followed by NVT equilibration at 300 K, the materials are ready for performing the AO impact simulations. The time step of the simulations is 0.1fs and AO are added to the simulation every 200fs and the position of putting these AO are about 65 angstroms over the surface of the materials. The position of the AO in the plane parallel to the surface of the material (x and y coordinates) are picked randomly for each AO added to the system. These AO are directed towards the material with 4.5 eV energy and impact the surfaces of the materials perpendicularly.

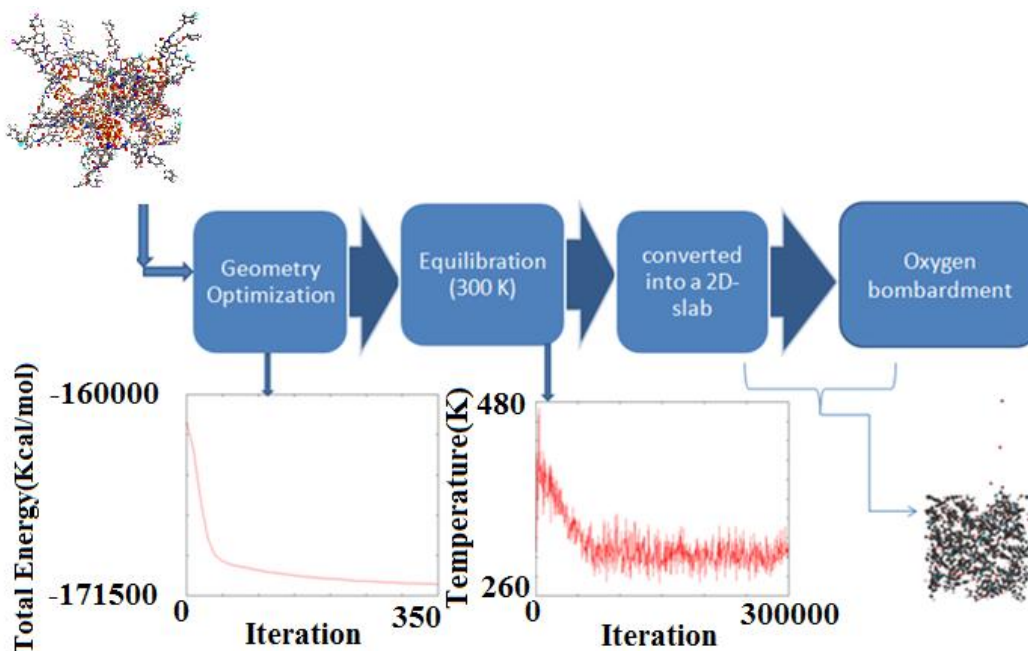


Figure 9. Steps used in the AO collision simulations

## 3.2 Results on AO impact simulations

### 3.2.1 AO impact

After minimization and equilibration of the structures, the surfaces of these three structures are collided with high energy AOs. These AOs are directed towards the slabs with 4.5 eV energy. Every 200 fs time interval, one AO is added to the system. The molecular dynamics simulation of these reactions are NVE simulations, indicating conservation of energy, and some key snapshots of the changes in Kapton, POSS and Silica during the simulation are shown in figure 10.

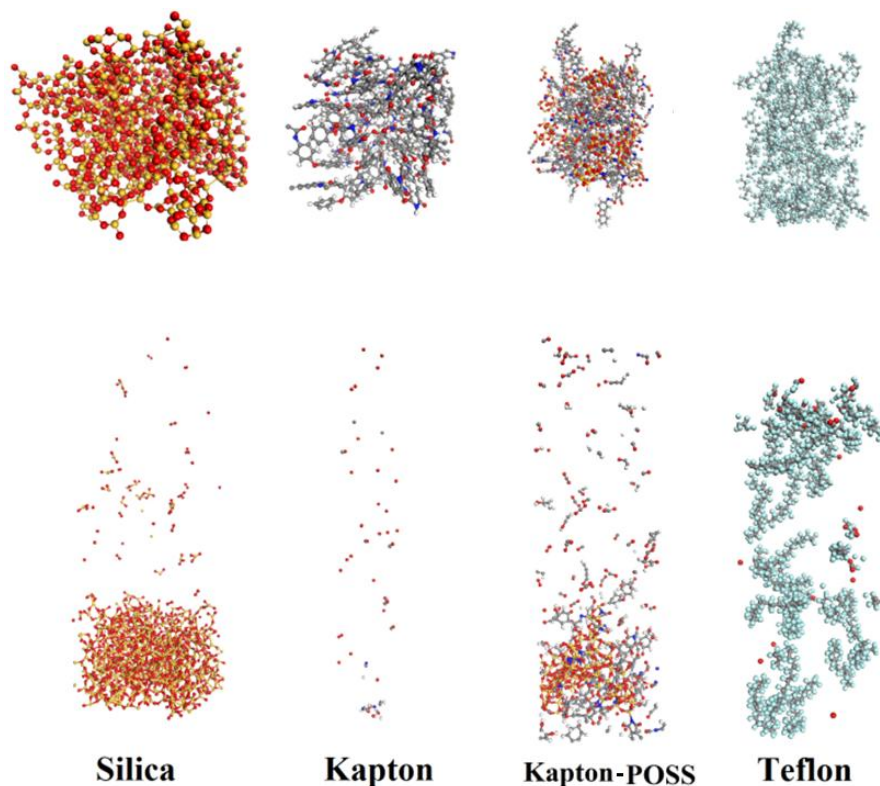


Figure 10. Key snapshots of AO collisions on Silica, Kapton, POSS and Teflon materials

The temperature evolution and the total remaining mass of the slabs under the AO impacts is shown in figures 11 and 12 respectively. For better understanding and because the initial weights of the slabs are different, the total mass is divided by the initial mass to obtain the normalized slab mass in figure 13.

With continuing the AO impact, the materials start to disintegrate at different rates and at some stage the materials are almost disintegrated. This is because of the limited number of the atoms of the initial slab used in the simulations. Because of this limitation in the size of the system, the trend of the mass loss at the first stages of the simulations (the values of first 200000 iterations) can best indicate the performance of these materials under AO collisions .

The AO impact on the silica results more exothermic reactions, however as shown in the figure 12, the silica is more stable than Kapton, POSS and Teflon. Based on the results in figures 11 and 12, Kapton-POSS shows much more stability compared to Kapton under AO impacts. It is clear that changing the Kapton structure to Kapton-POSS structure can improve the stability of this material against AO impact.

The chemical compositions of the materials released from the surface of Kapton, POSS, Teflon and Silica materials at the first stages of AO impacts are shown in table 2. These simulations show that at the first stages, water and O<sub>2</sub> are the first small molecules separating from the Kapton surface and with the progress of AO collisions, organic compounds containing Carbon start separating from the surface, while for the POSS, we can see such carbon containing organic materials coming off the surface even at the first stages of the simulation. The simulation of AO collisions on Silica surface shows the more stable performance of this material at the first stages and all the AO reaching the surface attach to the surface. By keeping AO collisions, first O<sub>2</sub> and later Silicon Oxide containing fragments separate from the surface of the Silica structure. For showing the first silicon containing molecules separating from the surface, the results of the simulation after impacting 250 atomic Oxygens on the silica surface are shown in table 2. The results show that also, Teflon shows very good stability against AO impact. The difference between the performance of Teflon compared to other materials under study is that most of the atomic oxygens impacting the surface of Teflon, don't react with the Teflon while for other three cases, most of atomic oxygens react with the surfaces. The data in the table 2 show that after adding 51 AO, several different molecules start to separate from the surface of Kapton and Kapton-POSS while Silica and Teflon still stay stable and just few small molecules separate from their surfaces.

In order to get a better understanding of the reactions that lead to separation of small molecules from these materials during AO impacts, some bond dissociation energies values are mentioned here which include most of the bonds inside these materials :

C-C ~ 3.7 eV, C-H ~ 3.5 eV, C-N ~ 3eV, C-O ~ 11.2 eV, C-F ~ 5.5 eV, O-H ~ 4.8 eV, Si-O ~ 8.3eV

These values show that AO impacts by 4.5 eV energy can mostly break C-C, C-H and C-N and O-H bonds at the first stages of AO impacts and will break other bonds when the temperature of the materials increases. The distribution of the molecules separating from these materials are in accordance with the prediction of bond breakings based on bond dissociation energies.

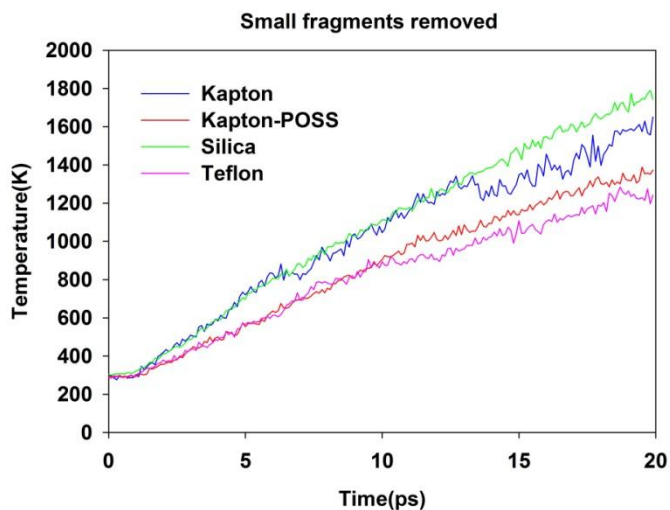


Figure 11. Temperature evolution of Kapton, Kapton-POSS, Teflon and amorphous silica under AO impact (NVE simulations)

**Table 2 Chemical compositions of the materials separating from the surface of Kapton, POSS and Silica materials at the first stages of AO impacts**

Material	Number of AO added	Number of AO reacted	Molecules separated from the surface
Kapton	21	11	1H <sub>2</sub> O
Kapton- POSS	21	14	1C <sub>6</sub> H <sub>5</sub> O <sub>2</sub>
Silica	21	12	-----
Teflon	21	1	-----
Kapton	36	27	1HO, 1H, 2O <sub>2</sub> , 1C <sub>2</sub> H <sub>2</sub> O <sub>2</sub> , 1H <sub>2</sub> O
Kapton- POSS	36	28	1CO <sub>2</sub> , 1H <sub>2</sub> O, 1HO, 1C <sub>3</sub> H <sub>2</sub> O, 1CO, 1C <sub>6</sub> H <sub>5</sub> O <sub>2</sub> , 1O <sub>2</sub>
Silica	36	24	-----
Teflon	36	3	-----
Kapton	51	42	1C <sub>6</sub> H <sub>6</sub> O <sub>3</sub> , 1C <sub>6</sub> H <sub>5</sub> O, 1CO <sub>2</sub> , 1C <sub>2</sub> HO, 1C <sub>4</sub> H <sub>2</sub> O <sub>3</sub> N, 3O <sub>2</sub> , 1CHO, 1H, 1C <sub>2</sub> HO <sub>2</sub> , 1 HO
Kapton- POSS	51	43	2H <sub>2</sub> O, 1CO <sub>2</sub> , 3HO, 1C <sub>5</sub> H <sub>4</sub> O <sub>2</sub> , 2CO, 1C <sub>3</sub> H <sub>2</sub> O, 1C <sub>2</sub> HO, 1C <sub>4</sub> H <sub>4</sub> O <sub>2</sub> , 1O <sub>2</sub>
Silica	51	40	1O <sub>2</sub>
Teflon	51	8	4COF <sub>2</sub>
Silica	250	214	16 O <sub>2</sub> Si, 38O <sub>2</sub> , 6O <sub>3</sub> Si, 2O <sub>3</sub> Si <sub>2</sub> , 2O <sub>4</sub> Si <sub>2</sub> , 1O <sub>5</sub> Si <sub>2</sub>

For comparing the simulations results with experimental results, the AO erosion yield observations of Materials International Space Station Experiment 2 (MISSE 2) have been used. In these experiments, different materials which have been used for making different elements on the surface of spacecraft have been exposed to the low Earth orbit (LEO) environment on the exterior of the International Space Station (ISS) for nearly four years. Based on these experimental results, the erosion yield for Kapton is  $4.28 \times 10^{-24}$  g/oxygen atom and this value for Teflon is  $3.05 \times 10^{-25}$  g/oxygen.

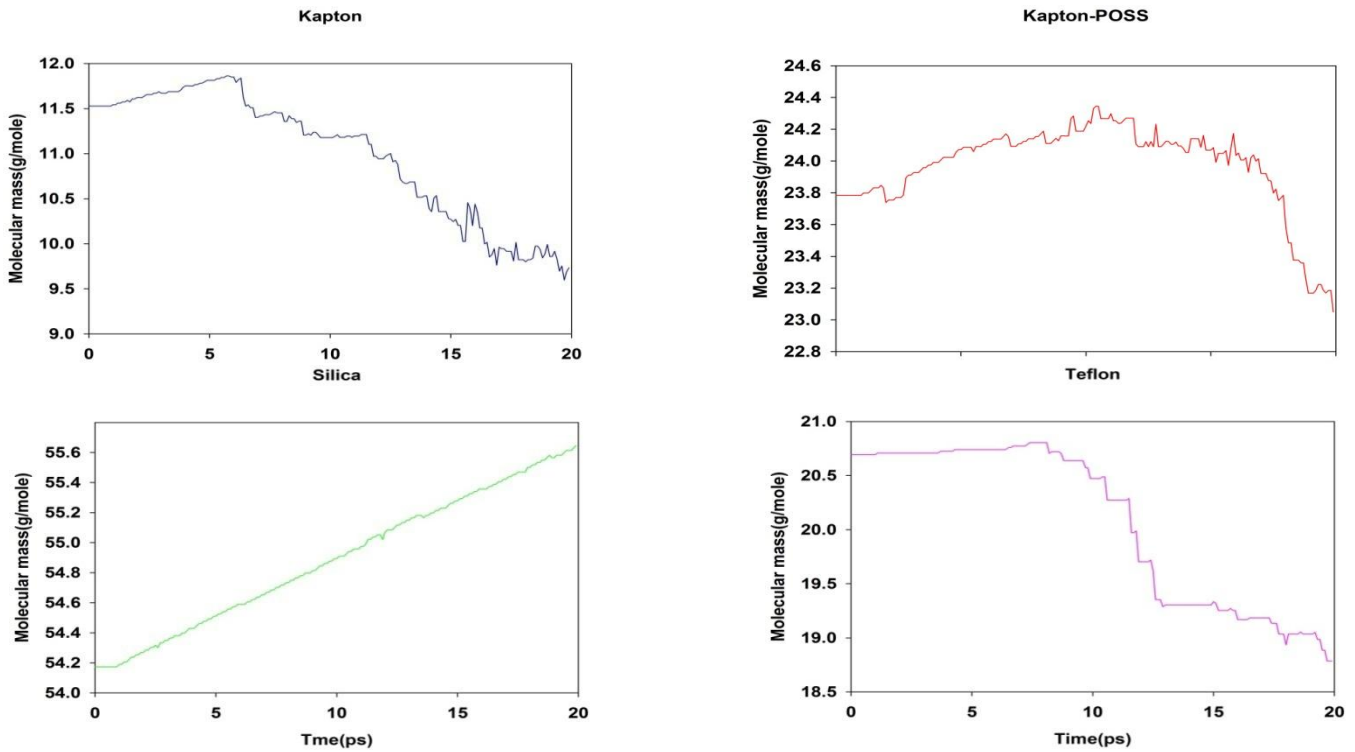


Figure 12. Total mass of the Kapton, Kapton-POSS, Teflon and amorphous silica slabs under AO impact(NVE simulations)

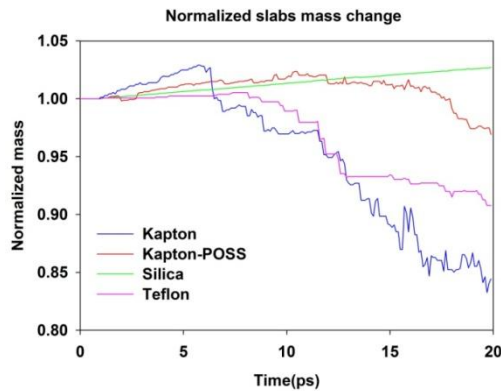


Figure 13. Normalized slab mass changes of the Kapton, Kapton-POSS, Teflon and amorphous silica slabs obtained by dividing the remaining slabs mass by the initial mass of the slabs

The erosion yield results of the simulations for Kapton and Teflon are shown in table 3. If we consider the erosion yield of Kapton and Teflon at the first stages of the simulation where

separation of small molecules starts from the surfaces, the erosion yield values are close to the experiment results.

Because there isn't complete understanding about the details of the interactions of AO and the surface of the materials during the AO impacts, and also because there are some differences between AO impacts experimental results, further investigations of these interactions are needed. At high impact energies, the issue of electron excitation might be an important feature to be considered too. Therefore, physical chemistry investigations of such phenomenon can be very helpful in achieving better understanding of these interactions.

**Table 3 Erosion yield results of Kapton and Teflon AO collision simulations**

<b>Material</b>	<b>Number of AO added</b>	<b>Erosion Yield(g/Oxygen atom)</b>
<b>Kapton</b>	21	$1.42 \times 10^{-24}$
<b>Teflon</b>	21	0
<b>Kapton</b>	36	$7.29 \times 10^{-24}$
<b>Teflon</b>	36	0
<b>Kapton</b>	51	$2.00 \times 10^{-23}$
<b>Teflon</b>	51	$5.86 \times 10^{-25}$

### **3.2.2 Heat transfer effects**

Considering there is some heat transfer between the materials on the surface of the spacecraft and other parts, we repeated the NVE-simulations described in the previous section using a canonical NVT/Berendsen thermostat ensemble with three different thermostats –strong ( $T_{\text{damp}}=100\text{fs}$ ), medium ( $T_{\text{damp}}=500\text{fs}$ ) and weak ( $T_{\text{damp}}=5000\text{fs}$ ).  $T_{\text{damp}}$  is the damping constant of

each of these thermostats. The results of these simulations and the effect of using thermostats in the simulation compared to the NVE simulation for Kapton, POSS and Silica are depicted in figures 14-15. If we compare the simulations with no thermostat and weak thermostat, it is clear that using thermostats, all the thermostats show the same performance for such systems and these thermostats keep the slab temperature around a constant value and preventing the temperature increase in each of the slabs during AO impacts, will prevent mass losses in the slabs.

This result indicates the importance of the material temperature in regards to the stability of them. On the other hand, it should be noted that the heat transfer of these materials on the surface of the spacecraft to the body of the spacecraft is not desired. All these requirements highlight the need for materials, which can show the desired qualities of current materials used, but they should be less exothermic when reacting with the high energy AO.

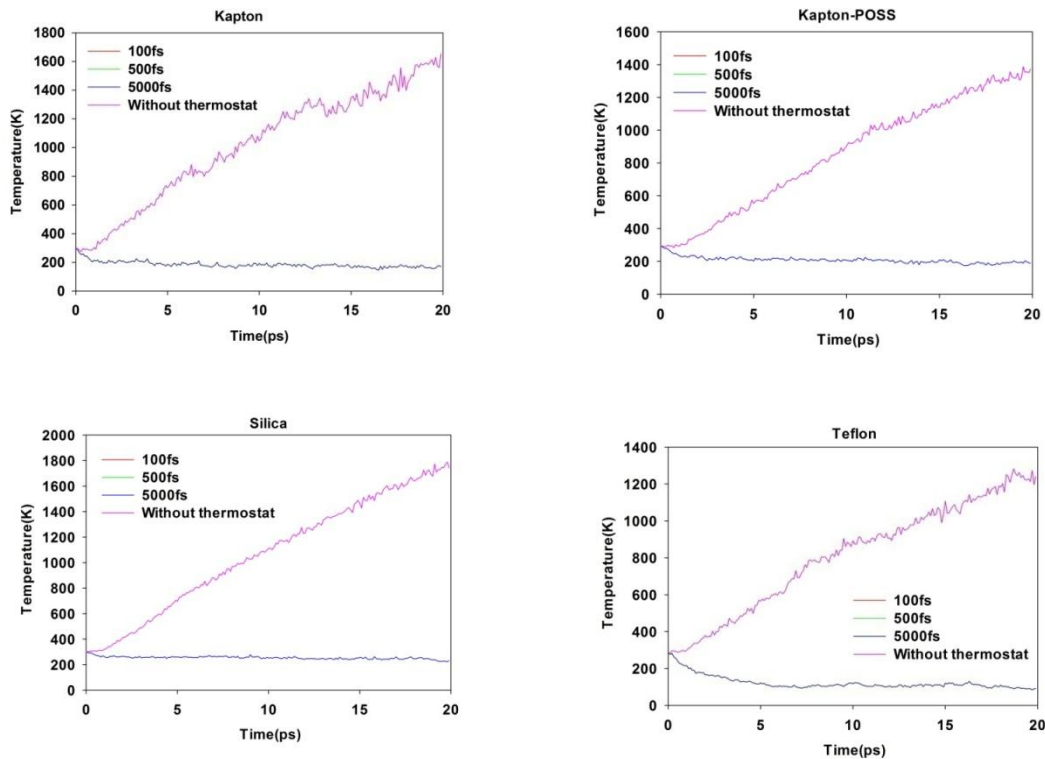


Figure 14. Temperature evolution of the Kapton,POSS and Silica during AO impact in NVE and NVT simulations. All the thermostats show the same performance for such systems. Therefore, the graphs for thermostats are on top of each other

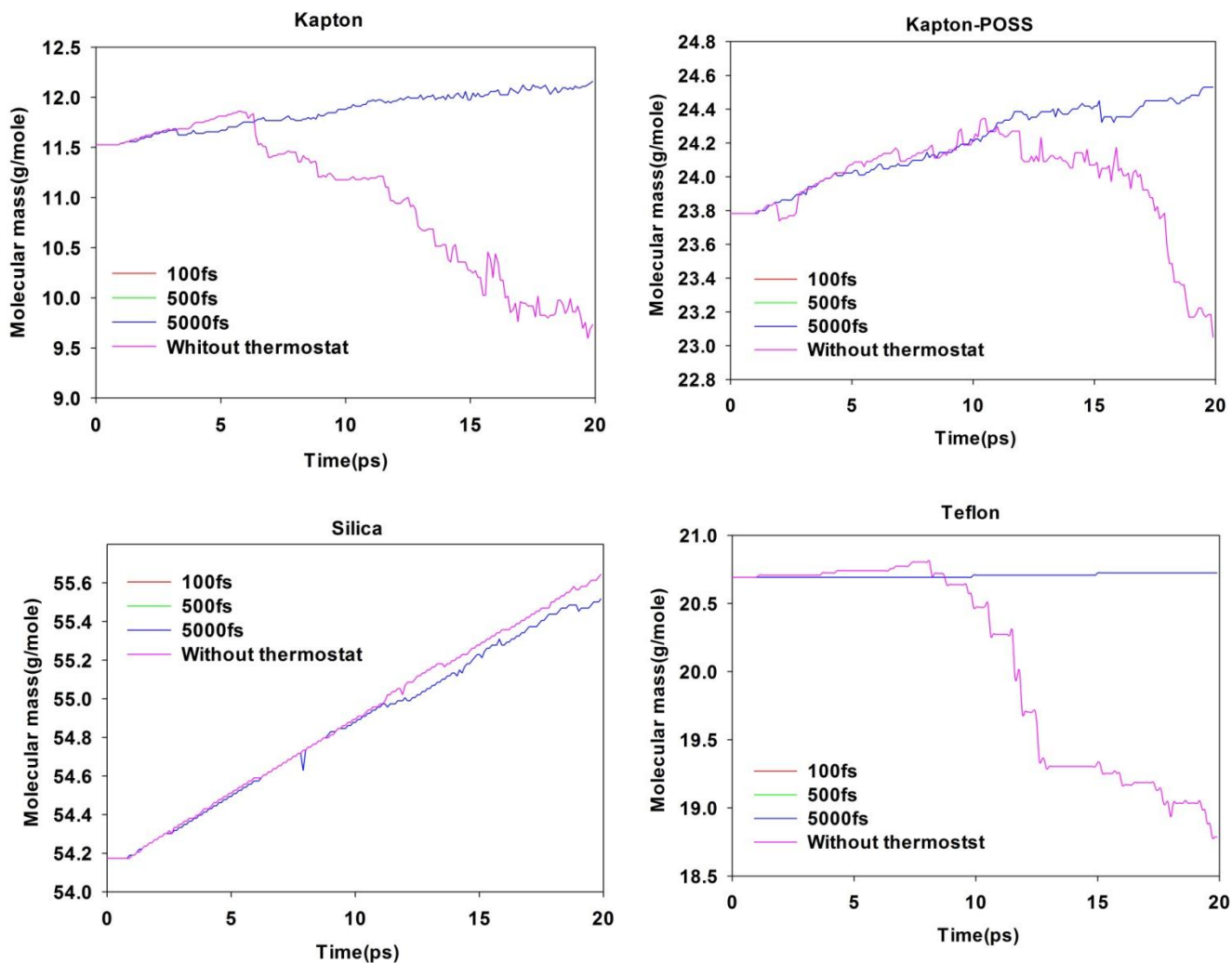


Figure 15. Total mass of the light weight molecules coming off the surface of the Kapton-POSS during AO impact. All the thermostats show the same performance for such systems. Therefore, the graphs for thermostats are on top of each other

### 3.2.3 The effect of different Silica ratios in Kapton-POSS

An important parameter which can play the main role in the characteristics of the Kapton-POSS is the amount of silicon in the bulk of the material. For evaluating the effect of this silicon content, the simulations on Kapton-POSS with two different silicon contents is performed. The monomers which have been used for making two Kapton-POSS structures with different silicon

contents are depicted in figure 16. The monomer on the left is used for building the higher silicon content structure and the monomer on the right is used for building the lower silicon content structure. The numbers of the atoms in these two different structures is shown in the table 4.

**Table 4 The numbers of different atoms in two different Kapton-POSS structures**

<b>Atoms</b>	<b>Lower silicon content structure</b>	<b>Higher silicon content structure</b>
<b>C</b>	880	660
<b>H</b>	560	540
<b>O</b>	440	510
<b>Si</b>	160	240
<b>N</b>	80	60
<b>Total</b>	2120	2010

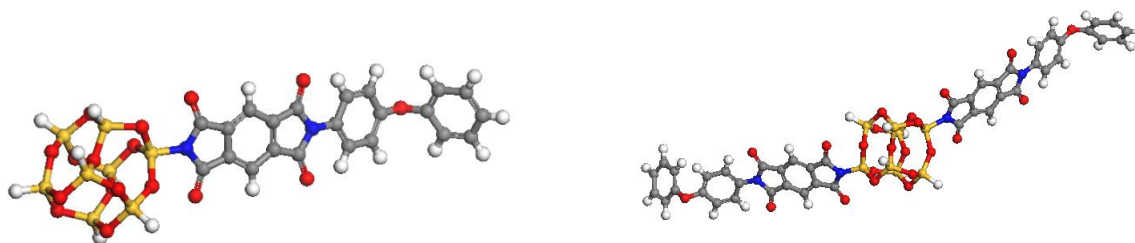


**Figure 16. Two different monomers used for building two Kapton-POSS structures with different silicon contents. Using the left monomer can provide higher silicon content inside the material, provided that both final structures will have the same total number of atoms**

In the simulations, the AOs are directed towards the slabs with 4.5 eV energy. Every 200 fs time interval, one AO is added to the system and the time step of the simulations is 0.1 fs.

The total remaining mass of the slabs and the normalized slab mass under the AO attack are shown in figures 17 and figure 18 respectively. Based on these results, at the end of the

simulation, the slab with lower Si content loses about 3 percent of the initial mass and the slab with higher Si content loses about 1 percent of the initial mass. The temperature evolution of these slabs during AO impact is depicted in figure 19.

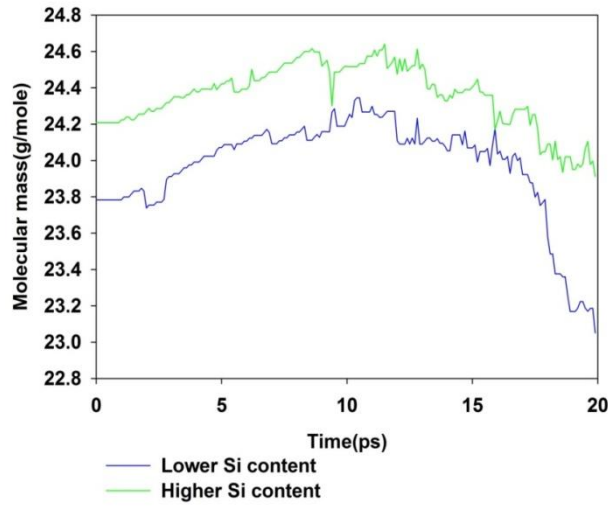


Figure 17. Total remaining mass of the two Kapton-POSS structures with different Si contents during AO impact

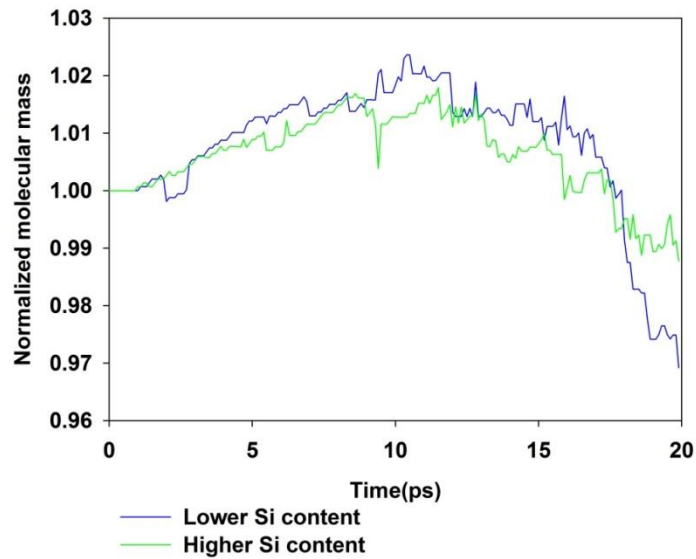


Figure 18. Normalized slab mass changes of the Kapton-POSS with different Si contents obtained by dividing the remaining slabs mass by the initial mass of the slabs

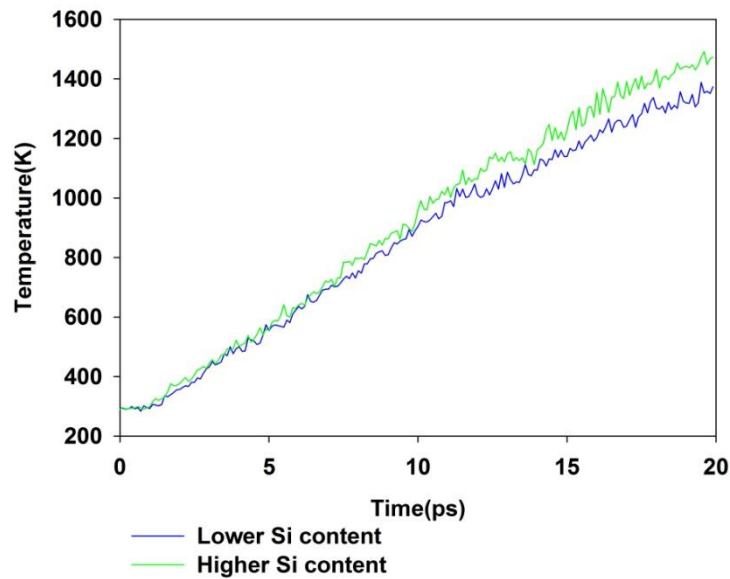


Figure 19. Temperature evolution of the Kapton-POSS with different Si contents during AO impact in NVE simulations

These results indicate that there would be slight increase in the temperature of the Kapton-POSS with higher Si content. Because of the limitations on the amount of mass and temperature for the materials used on the surface of the spacecraft, these parameters should be considered in selecting the surface elements materials. Computational chemistry methods can provide a useful tool for searching optimal material composition under LEO conditions.

## 4. Ice Cluster Impacts on Amorphous Silica

Due to the complexity of the dynamics of hypervelocity ice cluster impacts on surfaces, a straightforward interpretation of experimental results is usually not possible. However, these phenomena can be studied using classical molecular dynamics simulations, which provide a powerful tool in understanding the dynamics of ice cluster cluster-surface collisions.

These investigations can help better understanding of physical and physicochemical behavior of materials under extreme conditions of pressure and temperature in conditions like astrophysical processes and high-barrier reactions.

Although many efforts have been put in understanding the cluster-surface collision phenomena, still many parameters that can play important role in this field should be studied in more detail in different length and time scales. In this study we will try to shine more light on different aspects of these phenomena which can take place at the extreme conditions. Particularly, for ice cluster impacts, the effect of cluster impact velocity on the amount of ice accumulation and the subsequent change in structure of the ice cluster will be studied.

Silicon-based compounds are widely used at different parts of spacecraft and aircraft like coatings, seals and photovoltaic parts. The performance of silicon-based materials at space conditions has been widely studied. Coatings obtained by sputter deposition of fully oxidized and suboxide silica have been used on the surface of spacecraft. Because of widespread applications of these materials on the spacecraft, fully oxidized and suboxide silica structures have been selected here to study the effects of hypervelocity ice cluster collisions. This can be extended to the study of ice clusters impacting on other materials such as aluminum or polymer composites.

## 4.1 Method description

In this research, atomistic scale simulations results of high velocity impacts of amorphous and crystal ice clusters on amorphous fully oxidized and suboxide silica surfaces at different impact velocities are studied. For performing these simulations, the ReaxFF reactive force field method was used in conjunction with the stand-alone ReaxFF program. The ReaxFF method can provide the computational requirements to perform molecular dynamics simulations on systems which are sufficiently large. Therefore, we will be able to describe the full chemistry of the reactions using this method.

Two different amorphous silica structures are used in these hypervelocity impact simulations. These two silica structures are fully oxidized silica and suboxide silica. For obtaining these structures,  $\text{SiO}_2$  and  $\text{SiO}_{1.5}$  building molecules are put inside periodic simulation boxes at initial low densities and then slowly compressed. During the compression, the small silica molecules start to react and form a silica structure including 2600 atoms for suboxide silica structure and 2610 atoms for the fully oxidized silica structure. After this stage, the surface of the silica structure is opened and the annealing process between 150K to 700K is performed. At the end of this surface opening and annealing process, the density of the silica structure which is ready for the ice deposition on top of it is  $2.18 \text{ g/cm}^3$ .

Each amorphous ice cluster contains 150 water molecules and each crystal ice cluster contains 128 water molecules. The characteristics of these ice clusters are obtained from homogeneous water condensation and ice formation in supersonic expansions to vacuum for stagnation pressures from 12 to 1,000 mbar using the particle-based Ellipsoidal-Statistical Bhatnagar-Gross-Krook (ES-BGK) method[91, 92]. The amorphous ice clusters are obtained by equilibrating 150

water molecules inside a box with density of  $0.98 \text{ g/cm}^3$ . The final configuration of the amorphous and crystal ice clusters before the stage of sending them towards the silica surface are shown in Figure 20. In order to prevent premature interactions between ice cluster and silica surface, the ice cluster is put in an initial position so that the bottom of the ice cluster is at a distance about  $20\text{\AA}$  from the surface of the silica and the total system is equilibrated at 150K using NVT simulation. After equilibrating the total system, different velocities are added to the ice clusters in the direction normal to the silica surfaces in order to obtain different impact velocities.

During the collision between ice cluster and silica structure, numerous chemical and physical processes take place over very short time scales and include high local temperatures. This indicates that large time step in the simulations could potentially cause incorrect results. Therefore, in these simulations, 0.1 femto seconds (fs) time step is chosen. In order to ensure that 0.1 time step is short enough, the 7 km/s amorphous ice impact on suboxide silica simulations were repeated using 0.05 time step and the total simulation time was twice the total simulation time of the simulations with 0.1 time step. We selected 7 km/s which is the highest ice cluster impact velocity in our simulations because if the accuracy of the time step chosen for this simulation is demonstrated, this time step will also give accurate results for impact velocities lower than 7 km/s. The average number of molecules bouncing back from the silica surfaces for these simulations with 0.05 time steps show the same trend compared to the simulations with 0.1 time steps. Therefore, 0.1 time step for our simulations is sufficiently accurate for predicting the ice cluster impacts.

The molecular dynamics simulations of this study are based on ReaxFF reactive force field. These molecular dynamics simulations are NVE simulations, indicating conservation of energy.

The total time of each collision simulation is 30 pico seconds (ps). During the impacts, conservation of energy with a fluctuation of around 7 kcal/mol has been observed. These fluctuations take place around the average total energy of the system with a value around  $-4 \times 10^5$  kcal/mol for ice cluster impacts on the silica surfaces at different impact velocities. The total time of each collision simulation is 30 pico seconds (ps). In order to obtain statistically reliable results, simulations at different impact velocities are repeated three times and the results are analyzed based on the outputs of all these simulations.



Figure 20. Configuration of the ice clusters including 150 water molecules for amorphous ice and 128 water molecules for crystal ice clusters and equilibrated at the initial temperature of 150K

Figure 21 represents a schematic of the model used for the simulations which includes collision between amorphous ice cluster and silica surface.

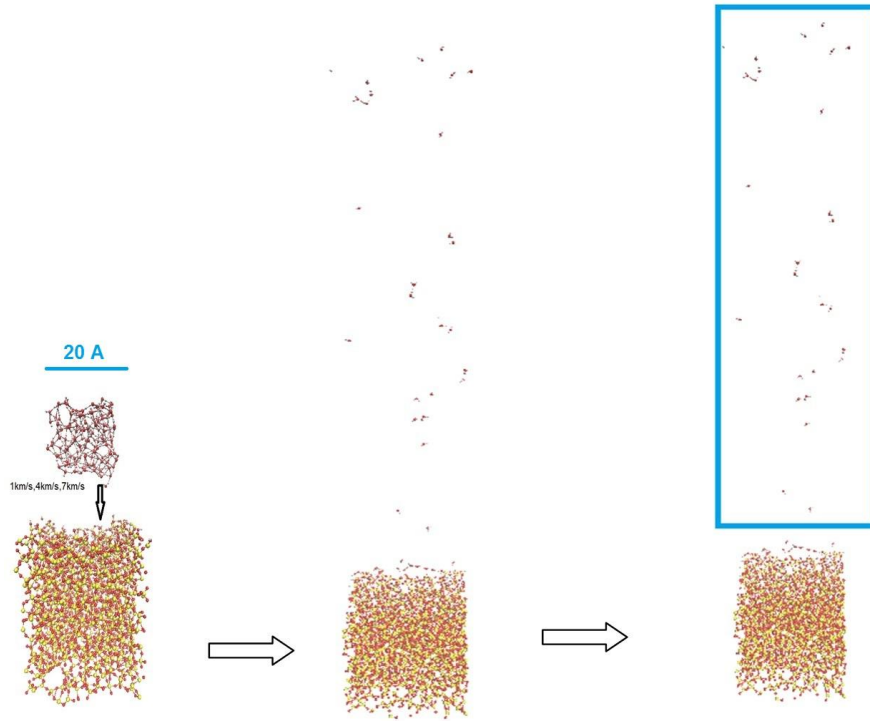


Figure 21. Separating the fragments bouncing back from the surface after ice cluster impact

## 4.2 Simulation results

### 4.2.1 Ice cluster impacts products

For investigating the effect of different impact conditions, separate impact simulations are performed with initial system temperature of 150K. This temperature is selected to make sure that water cluster is in sub-cooled condition at the moment of the impact. Amorphous ice clusters collide on the surface of the silica structures with 1, 4 and 7km/s impact velocities.

As shown in figure 21, the fragments bouncing back from the surface are the molecules which are far away from the surface and don't attach to the surface after the ice cluster impact. The distributions of different molecules separating from silica surfaces at these different conditions

are shown in Figure 22. In these graphs the numbers of water molecules that bounce back from the surface without reacting or attaching are not included. The details of these separating molecules are mentioned in Table 5. The numbers of each molecule in these figures are the average number of molecules observed in 3 ice cluster impacts at each separate impact condition. As mentioned before, each amorphous ice cluster includes 150 water molecules and each crystal ice cluster includes 128 water molecules. After ice cluster impacts at 1 km/s impact velocity, no fragments bounce back from the surface and the entire ice cluster accretes on the surface. At 4 km/s and 7 km/s impact velocities, some fragments bounce back from the surface. These results indicate that the amount of the fragments bouncing back from the surface increases with increasing the impact velocity which is in accordance with similar experimental studies[93]. These experimental studies have been conducted for ice cluster impact velocities less than 1km/s. The sticking coefficients of ice clusters decrease with increase of impact velocity. However, the sticking coefficient value at a special impact velocity is highly dependent on the size of the ice cluster and by decreasing the size of the ice cluster, an increase in the value of the sticking coefficient at the same impact velocity is observed. The sizes of the ice clusters in these experiments are in the range of 50-350  $\mu\text{m}$ .

The ice cluster impacts on fully oxidized silica surfaces cause more different types of molecules bouncing back from the surface compared to the ice cluster impacts on suboxide silica surfaces.

Table 5 The molecules bouncing back from the silica surfaces after ice cluster impacts. Each data point is the average value of three separate simulations with similar initial conditions

Amorphous ice impacts on fully oxidized silica			Amorphous ice impacts on suboxide silica		
	4 km/s	7 km/s		4 km/s	7 km/s
H <sub>2</sub> O	103	106	H <sub>2</sub> O	92	104
H	0	2.3	H <sub>3</sub> O	0.5	6.7
HO	2.5	3	H <sub>4</sub> O <sub>2</sub>	0	2
H <sub>3</sub> O	0	0.7	Total mass(g/mole)	1666	2071
HO <sub>2</sub>	0	0.5			
H <sub>2</sub> O <sub>2</sub>	0	0.3			
H <sub>3</sub> O <sub>2</sub>	1.3	1			
H <sub>4</sub> O <sub>2</sub>	0	4.3			
Total mass(g/mole)	1949	2193			
Crystal ice impacts on fully oxidized silica			Crystal ice impacts on suboxide silica		
	4 km/s	7 km/s		4 km/s	7 km/s
H <sub>2</sub> O	79	93	H <sub>2</sub> O	69	90
H	0	1	H	0.3	0.7
HO	1	3.7	HO	0	0.3
H <sub>3</sub> O	0	0.3	H <sub>3</sub> O	2.3	5.7
O <sub>2</sub>	0	0.3	H <sub>5</sub> O <sub>2</sub>	0.3	0
H <sub>3</sub> O <sub>2</sub>	0.3	0.7	Total mass(g/mole)	1299	1734
H <sub>4</sub> O <sub>2</sub>	0	2.3			
H <sub>6</sub> O <sub>3</sub>	0	0.3			
Total mass(g/mole)	1445	1868			

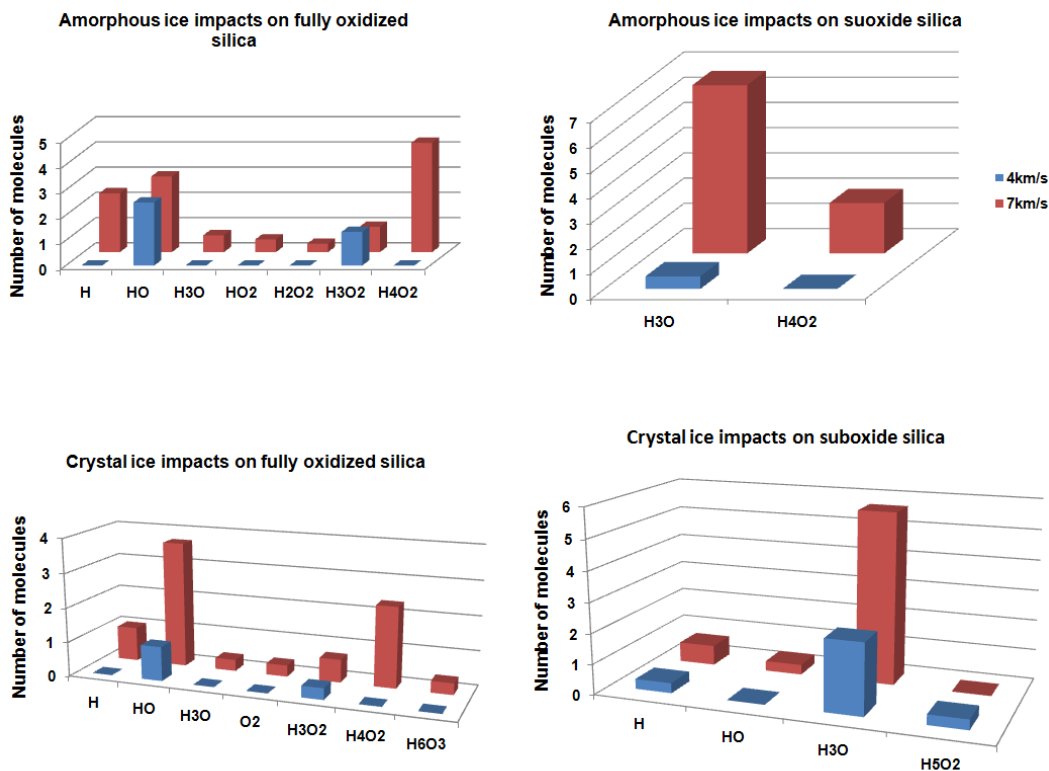


Figure 22. Distribution of the molecules separating from the silica surface at different amorphous ice cluster impact velocities

In order to investigate the water molecules dissociations after ice cluster impacts, the number of molecules which form as a result of water dissociation after each ice cluster impact is divided by the initial number of water molecules inside the ice cluster. These values are shown in table 6. These values show that in most cases, the water dissociations are more in the case of amorphous ice cluster impacts compared to crystal ice cluster impacts. This can be attributed to the difference between amorphous and crystal ice in the density and bonding arrangement.

Table 6 Normalized number of water molecules which dissociate after ice cluster impacts. Each data point is the average value of three separate simulations with similar initial conditions

Crystal ice cluster on fully oxidized silica		Amorphous ice cluster on fully oxidized silica	
4 km/s	0.00887	4 km/s	0.02553
7 km/s	0.05773	7 km/s	0.08107
Crystal ice cluster on suboxide silica		Amorphous ice cluster on suboxide silica	
4 km/s	0.01993	4 km/s	0.00333
7 km/s	0.04447	7 km/s	0.0578

The average number of O or H atoms which are initially part of the ice clusters, remaining on the silica surface after first 4km/s and 7km/s ice cluster impacts and the standard deviation statistical errors are shown in figure 23. These results show that there is more ice accumulation on the silica surface at 4 km/s impacts compared to 7km/s impacts.

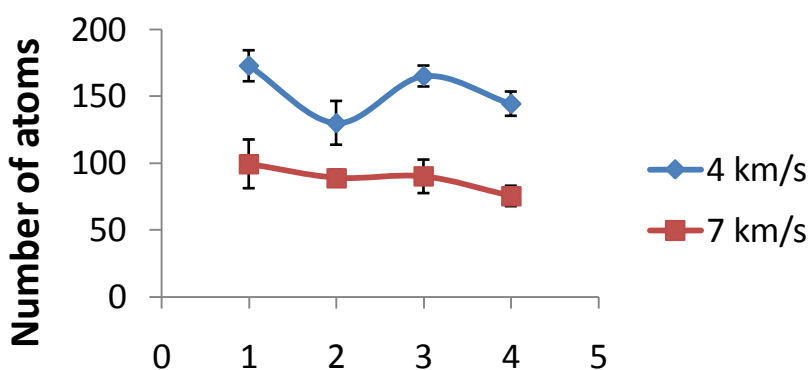


Figure 23. Average number of O and H atoms of ice cluster remaining on the silica surface after first impact. 1: Amorphous ice impacts on suboxide silica, 2: Amorphous ice impacts on fully oxidized silica, 3: Crystal ice impacts on suboxide silica, 4: Crystal ice impacts on fully oxidized silica

### 4.2.3 Multiple ice cluster impacts

In this section we tried to investigate the effect of multiple ice cluster impacts on silica surfaces. After each ice cluster impact, the molecules that bounce back from the surface are removed from

the simulation box and a new ice cluster is put inside the box at around 20 Angstrom away from the surface (Figure 24). Before sending the new ice cluster towards the surface, the system is equilibrated at 150 K.

In order to investigate the amount of ice cluster attaching to the surface after each impact, the total number of H and O atoms which remain on the surface after removal of bouncing back molecules are studied at the end of each simulation. For obtaining statistically reliable data, each simulation is repeated three times. The amorphous ice clusters include 150 water molecules (450 H and O atoms) and the crystal ice clusters include 128 water molecules (384 H and O atoms). The details of the number of H and O atoms that attach to the silica surfaces are mentioned in Table 7.

**Table 7** Number of H and O atoms accreting on the fully oxidized and suboxide silica surfaces after crystal and amorphous ice cluster impacts. Each data point is the average value of three separate simulations with similar initial conditions

Crystal ice cluster on fully oxidized silica				Amorphous ice cluster on fully oxidized silica			
	1 <sup>st</sup> impact	2 <sup>nd</sup> impact	3 <sup>rd</sup> impact		1 <sup>st</sup> impact	2 <sup>nd</sup> impact	3 <sup>rd</sup> impact
1 km/s	384	384	384	1 km/s	450	450	450
4 km/s	144	144	87	4 km/s	139	136	68
7 km/s	75	49	19	7 km/s	89	51	33
Crystal ice cluster on suboxide silica				Amorphous ice cluster on suboxide silica			
	1 <sup>st</sup> impact	2 <sup>nd</sup> impact	3 <sup>rd</sup> impact		1 <sup>st</sup> impact	2 <sup>nd</sup> impact	3 <sup>rd</sup> impact
1 km/s	384	384	384	1 km/s	450	450	450
4 km/s	165	168	133	4 km/s	176	162	138
7 km/s	96	89	70	7 km/s	108	111	64

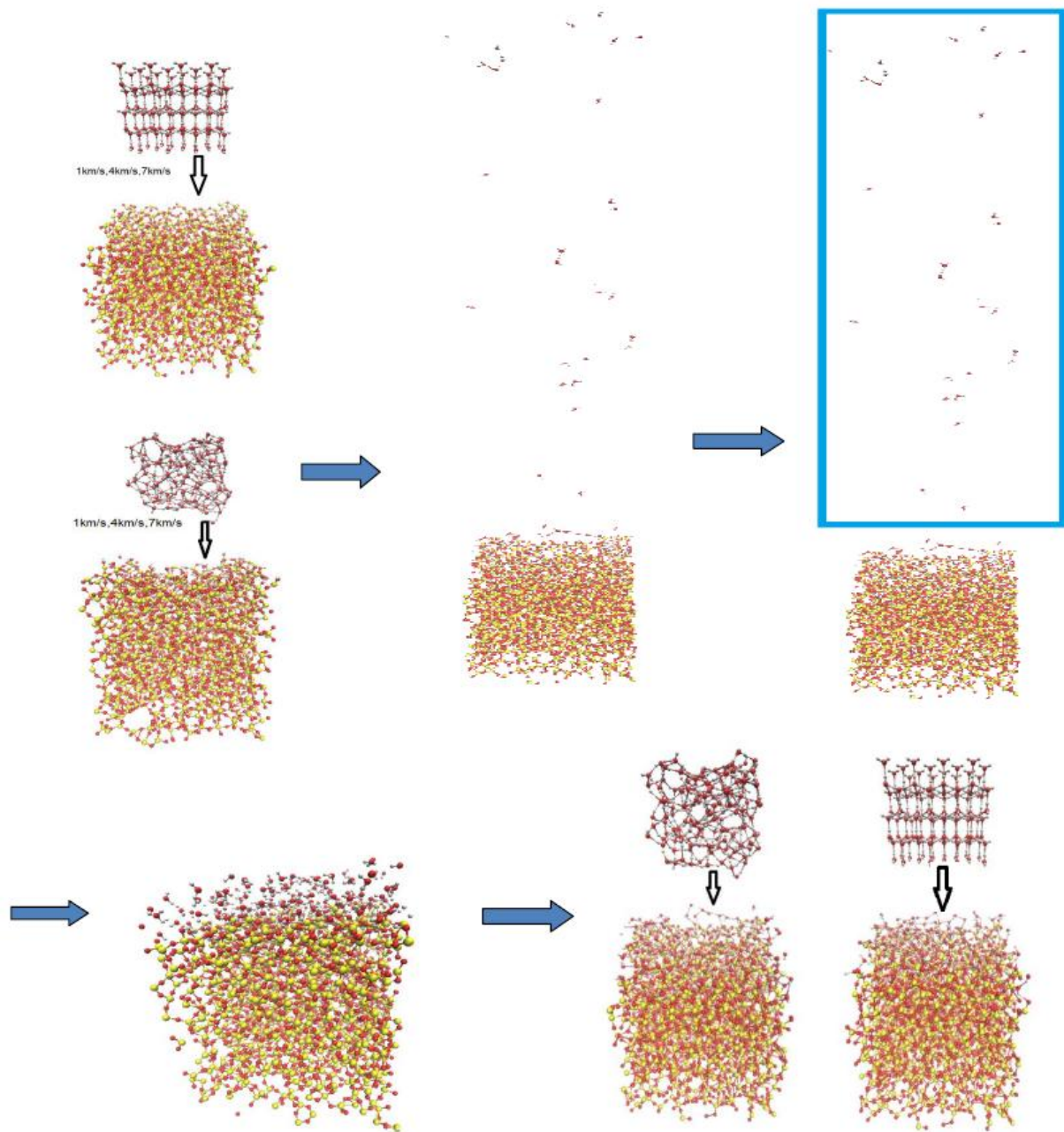


Figure 24. Multiple ice cluster impacts on the silica surfaces. After each impact the fragments which bounce back from the surface are removed from the simulation system

These results show that at 1 km/s ice cluster impact velocity the highest amount of ice accumulation is observed for both crystal and amorphous ice impacts. With increasing the ice

cluster impact velocities to 4 km/s and 7 km/s the amount of ice accumulation decreases. Generally at different ice cluster impact velocities, the ice accumulation is more on suboxide silica compared to fully oxidized silica surfaces. If we normalize the number of H and O atoms attaching to the silica surfaces by dividing the total H and O numbers by the initial total number of H and O atoms inside the ice cluster before the impacts (Table 8) , the numbers can represent the sticking coefficients for these ice clusters. These values show that generally, the sticking coefficients for crystal ice clusters are higher than amorphous ice clusters. The sticking coefficient values for all 1 km/s impacts are equal to 1.

**Table 8 Sticking coefficients for crystal and amorphous ice clusters**

Crystal ice cluster on fully oxidized silica				Amorphous ice cluster on fully oxidized silica			
	1 <sup>st</sup> impact	2 <sup>nd</sup> impact	3 <sup>rd</sup> impact		1 <sup>st</sup> impact	2 <sup>nd</sup> impact	3 <sup>rd</sup> impact
4 km/s	0.375859	0.375	0.225703	4 km/s	0.308889	0.302222	0.15
7 km/s	0.196172	0.127604	0.049479	7 km/s	0.197778	0.113333	0.0726
Crystal ice cluster on suboxide silica				Amorphous ice cluster on suboxide silica			
	1 <sup>st</sup> impact	2 <sup>nd</sup> impact	3 <sup>rd</sup> impact		1 <sup>st</sup> impact	2 <sup>nd</sup> impact	3 <sup>rd</sup> impact
4 km/s	0.429688	0.436641	0.346354	4 km/s	0.39	0.36	0.306667
7 km/s	0.25	0.231771	0.182292	7 km/s	0.238889	0.246667	0.141111

### **4.2.3 Ice cluster impacts on the silica surfaces which are completely covered with ice layers**

Another subject of interest is the ice cluster impact on the surfaces that are completely covered with ice layers. In order to perform such simulations, the ice clusters are deposited on the silica surfaces with 1 km/s impact velocities. After that, another ice cluster is sent towards the surface

at impact velocities of 1 km/s, 4 km/s and 7 km/s (Figure 25). The details of the number of H and O atoms that attach to the silica surfaces are mentioned in Table 9. The negative values represent number of H or O atoms being separated from the surface.

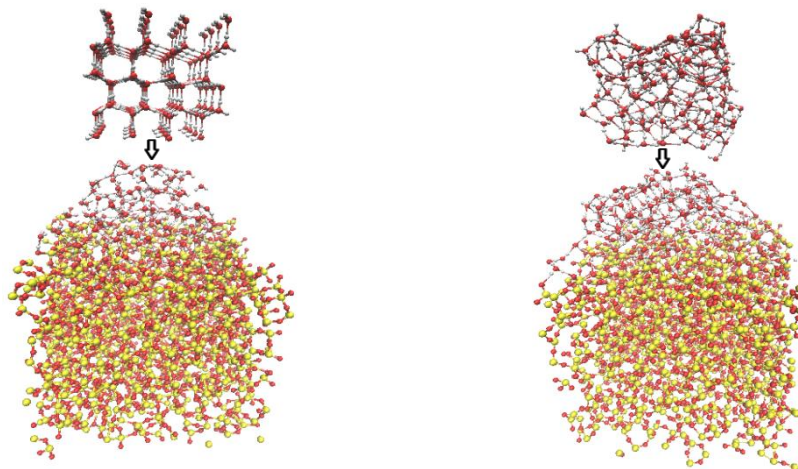


Figure 25. Amorphous and crystal ice cluster impacts on the silica surfaces that are completely covered with ice layers

The results show that when the silica surfaces are completely covered with ice layers, the 7 km/s ice impacts cause removal of ice molecules from the accumulated ice for both crystal and amorphous ice cluster impacts. This high velocity impact can cause melting of some layers of ice and cause the removal of these ice layers. However, crystal ice clusters impacting at 4km/s cause ice accumulation and amorphous ice clusters impacting at 4 km/s cause ice removal.

Table 9 Number of H and O atoms accreting or separating after second crystal and amorphous ice cluster impacts on the silica surfaces that are completely covered with ice layers

Crystal ice cluster on fully oxidized silica		Amorphous ice cluster on fully oxidized silica	
1 km/s	384	1 km/s	450
4 km/s	25	4 km/s	-17
7 km/s	-264	7 km/s	-344
Crystal ice cluster on suboxide silica		Amorphous ice cluster on suboxide silica	
1 km/s	384	1 km/s	450
4 km/s	57	4 km/s	-16
7 km/s	-200	7 km/s	-276

### 4.3 The possibility of electron excitation

One of the concerns related to the use of empirical reactive molecular dynamics methods in the simulations of hypervelocity impacts is the possibility of electron excitation during high energy impacts. In order to have an estimate of the chance of electron excitation in these simulations, the internal temperatures of the ice clusters during the collisions with impact velocities of 1 km/s and 10 km/s on suboxide silica, which represent our lowest and highest impact energy values, are studied and the results are shown in Figure 26. The temperatures in these graphs are the average temperature of all water molecules remaining inside ice clusters during the collisions. As these graphs indicate, the average temperature for the ice clusters during the 10 km/s impact is about 2000K, but individual molecules show temperatures of up to 9500K, which could potentially lead to electron excitation. Based on these results, we believe that electron excitation will not be

a major issue in these simulations at lower impact velocities (below 10 km/s). However, at impact velocities of 10 km/s and higher, it would be more prudent to consider the possibility of the electron excitement effects.

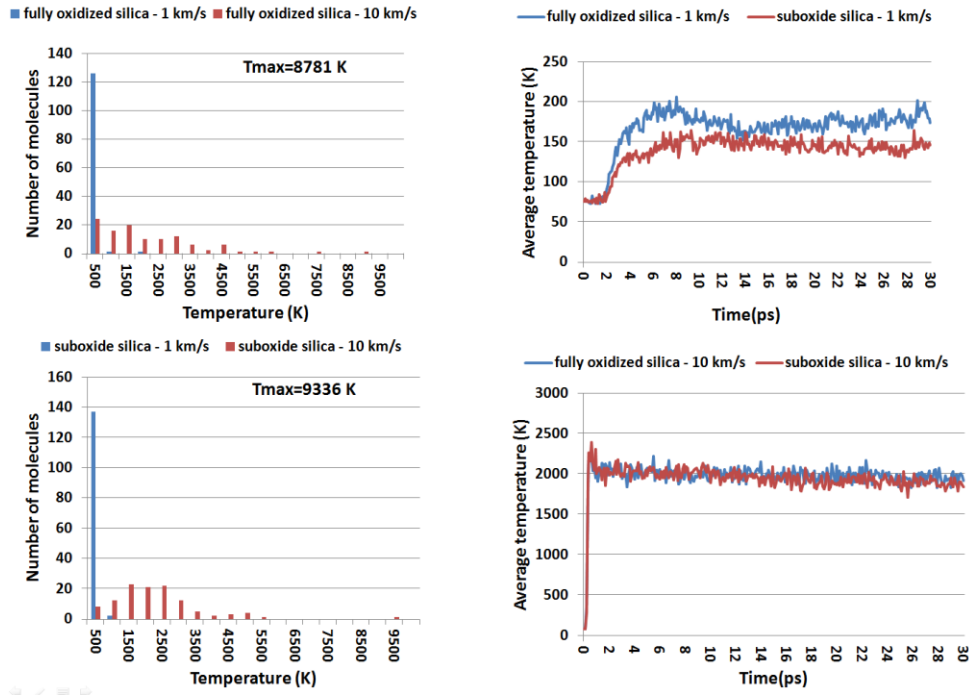


Figure 26. Average temperature evolution of ice clusters during impact on the fully oxidized and suboxide silica surfaces at amorphous ice impact velocities of 1km/s and 10 km/s. The number of molecules observed in each temperature range at the time that maximum temperature is observed inside the ice cluster during the collisions is shown in the left side histograms

## **5. Study of thermal conductivity of ice clusters after impact deposition on the silica surfaces**

For aircraft and spacecraft, ice is a threat both during flight and during take-off. Especially for aircraft, the ice accretion can decrease the lift and cause the pilot to lose control. When water droplets, which can be supercooled to  $-40^{\circ}\text{C}$ , impact on the cold aircraft surface, they can freeze and accumulate. Ice can be a source of debris from the external fuel tank of the spacecraft that can be released during launch or from the shuttle waste management system and has the potential to cause damage to the spacecraft surface elements[94].

The thermophysical properties of ice on the surface of the spacecraft play a key role in the physics of heat conduction. There have been significant amounts of studies on thermophysical properties of materials. These studies have been conducted on materials with different complexities and different calculations methods have been applied in thermal conductivity (TC) calculations. Some references have been mentioned on these studies in the introduction of this thesis.

The dominant contributors to the concept of thermal conductivity in water and ice clusters are phonons. Therefore, several methods have been developed to capture the phonon effect in predicting TC. Various different approaches have been applied in the calculation of TC of materials. One of the most straightforward methods applied in determination of TC is direct method. In the direct method, the TC is calculated as the ratio of an imposed heat flux to the resulting temperature gradient. The heat flux is imposed by adding kinetic

energy from hot side and withdrawing kinetic energy from cold side of the system. Another method for computation of TC is the Green–Kubo method. In this method, the TC is calculated in terms of the integral of correlation functions. This method uses the fluctuations of the heat current in a homogeneous equilibrium system to calculate the TC applying linear response theory. Other methods include the thermal diffusion method, Evans homogeneous field method and Boltzmann transport equation.

At the nano-scale, molecular structure of the materials and surfaces, and the interactions between them at the atomistic length scales play a key role in the heat transfer performance. Therefore, the molecular dynamics (MD) method emerges as a valuable method for investigation of the heat transfer in such scales. One of the objectives of this study is to use MD simulations to identify the relationship between the ice structure at the silica interface and its thermal transport properties. Because MD simulation provides the ability to obtain the detailed information on atomic level and the associated dynamics of the structure, it is used for the atomic level evaluation of the thermal transport characteristics. The force field used for these simulations has been already developed for silica-ice interface and can successfully describe water-dissociation and proton-transfer events at this interface, which can substantially affect the water/silica contact and affiliated thermal transfer.

Using ReaxFF reactive force field method, equilibrium and non-equilibrium molecular dynamics (EMD and NEMD) can be used to determine the thermal conductivity of materials, since these are computationally inexpensive and combine well with the relatively expensive ReaxFF force engine. In EMD method, an equilibrated system is used and the TC value is calculated with application of statistical averaging. In NEMD

method, the TC value is calculated using cooling/heating rates monitoring. The EMD and NEMD approaches are reliable alternatives to the traditional Green-Kubo method.

## **5.1 Simulation model and method**

### **5.1.1 Ice cluster impact simulations**

In this research, TC values of amorphous and crystal ice clusters after deposition on fully oxidized and suboxide silica surfaces at different impact velocities are evaluated. This study can be extended to the study of ice clusters deposited on other materials such as aluminum or polymer composites. In these simulations, the ice clusters deposit on the silica surfaces after impacting the silica surfaces with impact velocities of 0, 0.5 and 1 km/s. These ice cluster impacts can happen at lower velocities during aircraft missions or even higher velocities during collisions at spacecraft surfaces. However, in this study we have focused on this range of impact velocities. The changes in impacting ice clusters thermal conductivities at this impact velocity range can pave the path to predicting the trend of changes in the thermal conductivity of ice clusters at other impact velocities.

Two different amorphous silica structures are used in these simulations. These silica structures are fully oxidized silica and suboxide silica obtained by combining  $\text{SiO}_2$  and  $\text{SiO}_{1.5}$  building molecules for fully oxidized and suboxide silica respectively. Because spacecraft are traveling in abrasive environment, there is possibility of creating suboxide silica surfaces during the missions. Therefore, we have considered both fully oxidized and

suboxide silica in these studies. The characteristics of these silica structures are mentioned in Table 10. Initially, the  $\text{Si}_8\text{O}_{20}$  building blocks are put in a periodic box at low density. After this initial step, the system is compressed to reach to the high density of  $2.6 \text{ g/cm}^3$ . After this stage the surface of the silica structure is opened and the annealing process between 150K to 700K is performed. At the end of this surface opening and annealing process, the density of the silica structure which is ready for the ice deposition on top of it is  $2.18 \text{ g/cm}^3$ . The same procedure is applied for preparing the fully oxidized silica structure. The RDF graphs of the fully oxidized silica at 150K are shown in Figure 27. These graphs demonstrate good correspondence with realistic  $\text{SiO}_2$  amorphous silica[95].

**Table 10 Characteristics of fully oxidized and suboxide amorphous silica structures**

Amorphous silica type	Molecular formula	Total number of atoms	Molar mass (g/mole)
Fully oxidized	$\text{Si}_{870}\text{O}_{1740}$	2610	52250.46
Suboxide	$\text{Si}_{1040}\text{O}_{1560}$	2600	54140.84

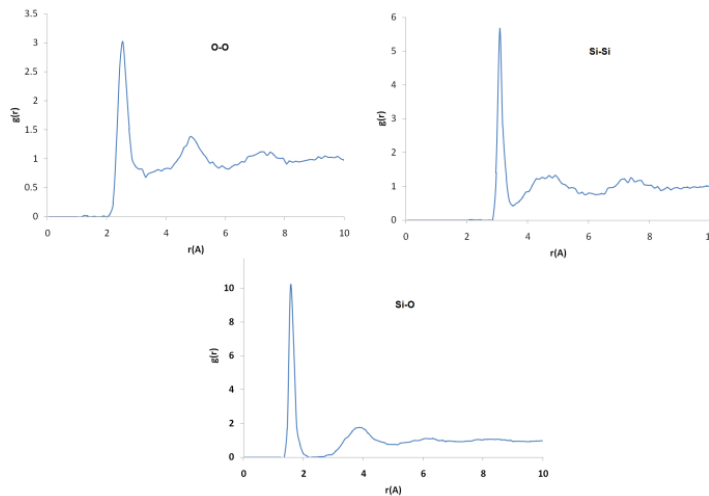


**Figure 27. RDFs in  $\text{SiO}_2$  silica shown for Oxygen-Oxygen O–O, Silicon-Silicon Si–Si, and Silicon-Oxygen Si–O**

The amorphous ice cluster contains 500 water molecules and the crystal ice cluster contains 512 water molecules. These ice clusters are prepared at the initial temperature of 150 K.

The amorphous ice structure was prepared by filling a box of size  $27.39 \times 27.06 \times 27.65 \text{ \AA}^3$  with 500 water molecules. This resulted in a density of  $0.98 \text{ g/cm}^3$ . The system was then equilibrated using an *NVT* ensemble at 150K.

In order to prevent pre-collision interactions between the ice cluster and silica surface, the ice clusters are put in an initial position so that the bottom of the ice clusters are at a distance about 20Angstrom from the surface of the silica. The total system is equilibrated at 150K using *NVT* simulation. This temperature is in the range of the temperatures observed during operations at high altitudes from the earth surface.

In order to start the collision procedure in each simulation, a velocity normal to the surface is given to the ice cluster to obtain impact velocities of 500 m/s and 1 km/s.

In these simulations, 0.1 femto seconds (fs) time step is chosen. The molecular dynamics simulations are *NVE* simulations, indicating conservation of energy. The total time of the each collision simulation is 30 pico seconds (ps). During the impacts, conservation of energy with a fluctuation of around 7 kcal/mol has been observed. These fluctuations take place around the average total energy of the system with a value around  $-4 \times 10^5 \text{ kcal/mol}$ .

Figure 28 shows several snapshots of the crystal ice impacting on the fully oxidized silica surface at two different impact velocities 500m/s and 1 km/s. The loss of crystallinity is more significant in the 1 km/s impact compared to 500m/s impact. This causes a decrease in the TC values of ice cluster which will be discussed later.

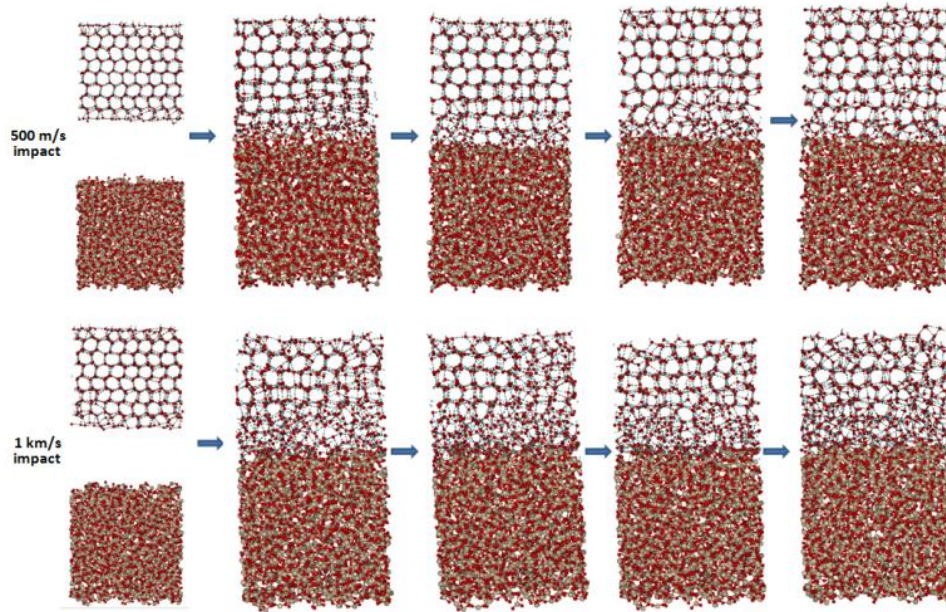


Figure 28. Snapshots of crystal ice-silica impact simulation. The crystal ice impacts on the fully oxidized silica surface at two different impact velocities - 500m/s and 1 km/s

### 5.1.2 The dual thermostat method

In the dual thermostat method, two thermostats are applied to different ends of the system. In our simulations, the Berendsen thermostats[90] are applied at two ends of the system. One side of the slab is kept at temperature  $T_H=300K$  and the other side of the slab is kept at  $T_C=150K$  temperature using these two thermostats. When the system reaches the steady state, a linear temperature profile is established along the ice slab.

The total system is equilibrated at 150K before applying the thermostats. Using the thermostat at the hot side, energy is added to the system and using the thermostat at the cold side of the slab, the energy is withdrawn from the system.

The schematic of the system for calculation of the ice slab TC after deposition on the silica surface is shown in Figure 29. The hot side thermostat is applied to the lower 500 atoms of silica ( $T_H=300K$ ) and the cold side thermostat is applied to the top 100 atoms of ice ( $T_C=150K$ ). The temperatures  $T_H$  and  $T_C$  of two thin layers of the ice are calculated every 0.25 pico seconds using equipartition theory. Equipartition theory relates the temperature of a system with its average energies.

After the first ice cluster depositions on the silica surfaces, the TC evaluation is performed for the middle 900 atoms inside the ice clusters. These atoms are shown inside a black box in Figure 29. Once steady state is reached, the thermal conductivity,  $k$ , is calculated from Fourier's law.

$$K = \frac{\langle \left| \frac{\Delta E}{\Delta t} \right| \rangle}{A \langle \left| \frac{dT(z)}{dz} \right| \rangle}$$

The change in energy  $\langle \Delta E \rangle$  is obtained as  $\langle \Delta E \rangle = \langle \Delta E_H \rangle + \langle \Delta E_C \rangle$  where  $\langle \Delta E_H \rangle$  is the time average of kinetic energy change in the hot side and  $\langle \Delta E_C \rangle$  is the time average of the kinetic energy change in the cold side of the system.  $A$  is the slab area perpendicular to the heat flux direction and  $\langle |dT(z)/dz| \rangle$  is the time average of the temperature gradient in the direction of the heat flux.

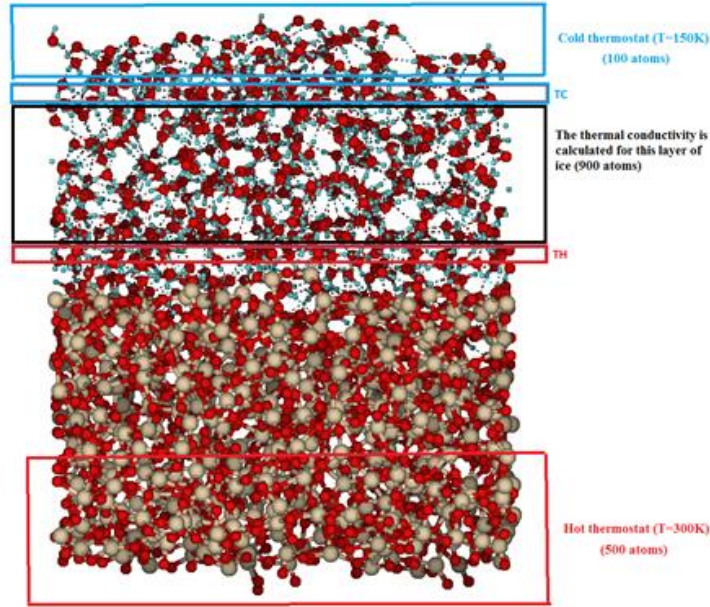


Figure 29. Schematic of the system for calculation of the ice TC after ice deposition on the silica surface

## 5.2 Simulation results

### 5.2.1 Thermal conductivity of amorphous and crystal ice clusters

In order to calculate the TC values for amorphous and crystal ice before deposition on the silica surface, amorphous and crystal ice clusters before deposition on the silica surfaces are studied. These values can be compared to the available experimental values for the TC of crystal and amorphous ice to evaluate the accuracy of the method.

Using the dual thermostat method and imposing 200K and 150K temperatures at both ends of the amorphous and crystal ice, the thermal conductivities are calculated. These

values along with the available experimental values are mentioned in Table 11, showing that the calculated TC values are in good agreement with the experimental values.

The TC of crystalline ice is larger than that of amorphous ice because the efficient thermal transport in solids arises from lattice vibrations (phonons). In crystalline ice the phonon's mean free path is large enough that it can move over relatively large distances ballistically before being scattered from structural defects. However, for amorphous ice, this effective heat transfer reduces considerably because of the disorder in the structure[96]

**Table 11 ReaxFF and experimental values of the thermal conductivity of amorphous and crystal ice**

Type of ice	Thermal conductivity from ReaxFF simulations(W/m.K)	Experimental thermal conductivity values (W/m.K)[96, 97]
Amorphous ice	1.4727	1.2-1.4
Crystal ice	2.1788	2.1-2.2

Before studying the TC values for the ice clusters after deposition on the silica surfaces, the TC values of fully oxidized and suboxide silica are calculated by the method similar to the method used for TC calculations of the ice clusters. The TC values are mentioned in Table 12. The experimental value of TC for fully oxidized silica is reported as 1.4 W/m.K. The calculated value of TC for suboxide silica is higher than the TC value for

fully oxidized silica. This is contributed to higher Si content in suboxide silica (Table 10). Silicon has a relatively high thermal conductivity value of 149 W/m.K[98].

**Table 12 ReaxFF and experimental values of the thermal conductivity of fully oxidized and suboxide silica**

Silica type	Thermal conductivity (W/m.K)
Fully oxidized silica	1.8
Suboxide silica	3.47

The phonon mean free path for amorphous ice has been reported to be around 5 Angstrom[99]. Considering the phonon mean free path equation  $\lambda \propto k/(\rho C v)$  where k is the thermal conductivity,  $\rho$  is the ice density, C is the ice specific heat capacity and v is the sound velocity[100], the mean free path value for crystalline ice should be around two to three times the value of the mean free path for amorphous ice based on the available values for k,  $\rho$  and C.

The dimensions of the systems which are studied are at least 27 Å which is larger than the mean free path of the ice clusters. Therefore, the method for determination of thermal conductivity values of the ice clusters is reasonable.

For plotting the temperature profile, T(z), as a function of the z coordinate for amorphous ice, after reaching the steady state condition along the ice cluster, four thin slabs are selected at four points along the slab (equal distance in z direction). Each slab includes 100 atoms. The temperature of each slab is calculated based on the equipartition theorem. The calculated temperatures are shown in Figure 30. This temperature profile can be estimated as linear profile. Therefore, the Fourier's law is applicable in these simulations.

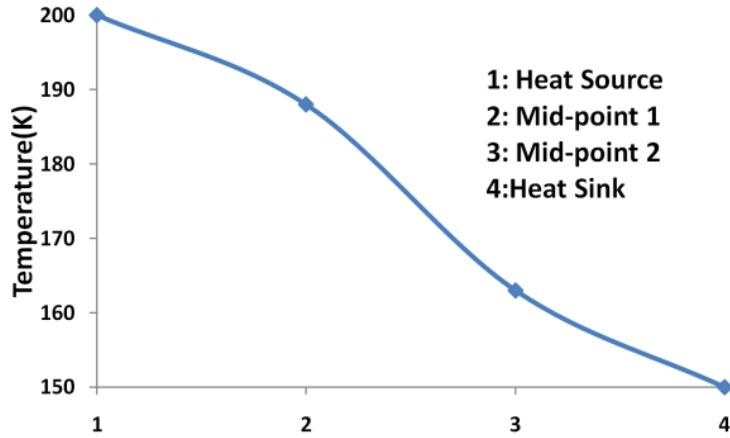


Figure 30. Temperature profile,  $T(z)$ , as a function of the  $z$  coordinate for amorphous ice after reaching steady state condition

The TC values for the cases that amorphous and crystal ice deposited on the silica surfaces are shown in Tables 13-16.

Table 13 ReaxFF values of the thermal conductivity of amorphous ice depositing on the fully oxidized silica surface with or without initial impact velocity on the silica surface

Deposition condition	Thermal conductivity (W/m.K)
No impact	0.59
500 m/s impact	0.61
1 km/s impact	0.62

Table 14 ReaxFF values of the thermal conductivity of amorphous ice depositing on the suboxide silica surface with or without initial impact velocity on the silica surface

Deposition condition	Thermal conductivity (W/m.K)
No impact	0.51
500 m/s impact	0.55
1 km/s impact	0.42

Table 15 ReaxFF values of the thermal conductivity of crystal ice depositing on the fully oxidized silica surface with or without initial impact velocity on the silica surface

Deposition condition	Thermal conductivity (W/m.K)
No impact	1.25
500 m/s impact	1.10
1 km/s impact	0.60

Table 16 ReaxFF values of the thermal conductivity of crystal ice depositing on the suboxide silica surface with or without initial impact velocity on the silica surface

Deposition condition	Thermal conductivity (W/m.K)
No impact	1.22
500 m/s impact	1.11
1 km/s impact	0.54

These results show that crystal ice shows higher TC value compared to amorphous ice. Impact of ice on the silica surface causes decrease of TC value for crystal ice compared to the ice deposition without impact. The decrease of the TC value for crystal ice can be attributed to increase of loss in the crystallinity of the structure of first layers of ice after impact. The RDF graphs of the crystal ice before and after 1km/s impact on the fully oxidized silica surface are shown in Figure 31. These graphs are for lower half of the ice cluster that has interface with the silica surface after impact on the silica surface. This loss in the crystallinity is evident in this RDF graph.

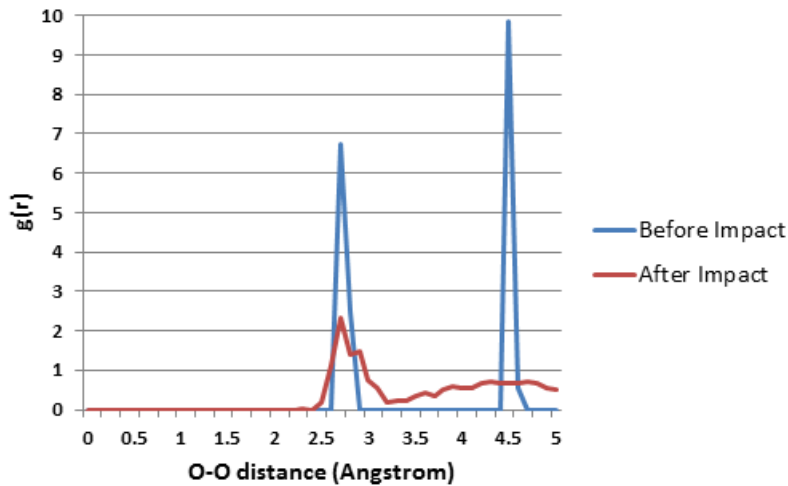


Figure 31. RDF graphs of crystal ice cluster before and after 1km/s impact on the surface of fully oxidized silica. These graphs are for the lower half of the ice crystal that has interface with silica surface after impact

The ice clusters on fully oxidized silica shows higher TC compared to the ice on suboxide silica. This is because of a higher degree of irregularity in the ice structure on the suboxide silica. The RDF graphs for the lower half parts of the crystal ice after attaching on the suboxide and fully oxidized silica with impact velocities of 1 km/s are shown in Figure 32. These graphs show that the crystal ice becomes more amorphous in lower layers after impacting on the suboxide silica surface.

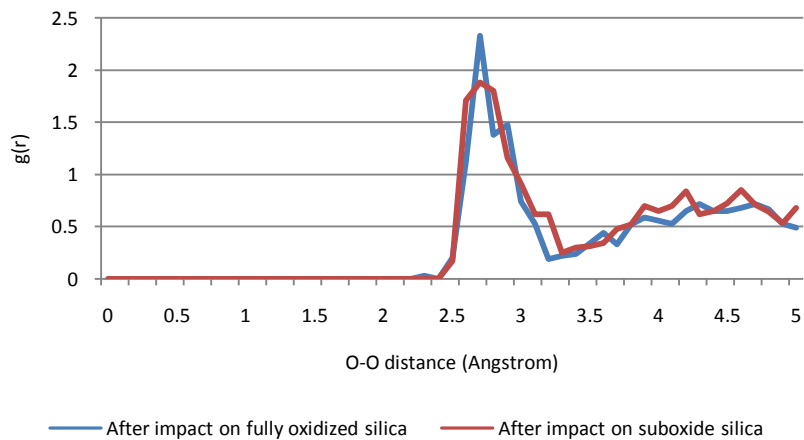


Figure 32. RDF graphs of the crystal ice cluster before and after 1km/s impact on the surface of suboxide and fully oxidized silica. These graphs are for lower half of the ice crystal that has interface with silica surface after impact

These results show a drop in the values of TC of the ice clusters after deposition on the silica surfaces compared to the TC values obtained for separate ice clusters. This drop can be attributed to presence of the interface between ice and silica surface and the difference between silica and ice structures. The structural mismatch causes reduction in the heat transfer at the ice-silica interfaces in addition to heat transfer resistance caused by discontinuity.

### **5.2.2 TC values of crystal and amorphous ice clusters after second impacts on the silica surfaces**

In order to investigate the change in the properties of the accreted ice during continued exposure to ice deposition, we investigated the collision of a second ice cluster on the surface of the previously deposited ice. Snapshots of the first and second crystal ice impacts on suboxide silica at 500 m/s and 1 km/s impact velocities are shown in Figures 33 and 34. As shown in these pictures, the retained crystal structure changes at different layers. After deposition of the second crystal ice cluster which impacts on the previously deposited ice with impact velocity of 500 m/s, the crystal structure of the second crystal ice cluster is almost preserved and amorphous structure is not observed in the lower layers of this second ice cluster. Therefore, after the second 500 m/s impact, the crystal ice stays almost intact at top layers. However, the loss of crystal structure is more pronounced at different layers of the second ice clusters impacting at 1 km/s.

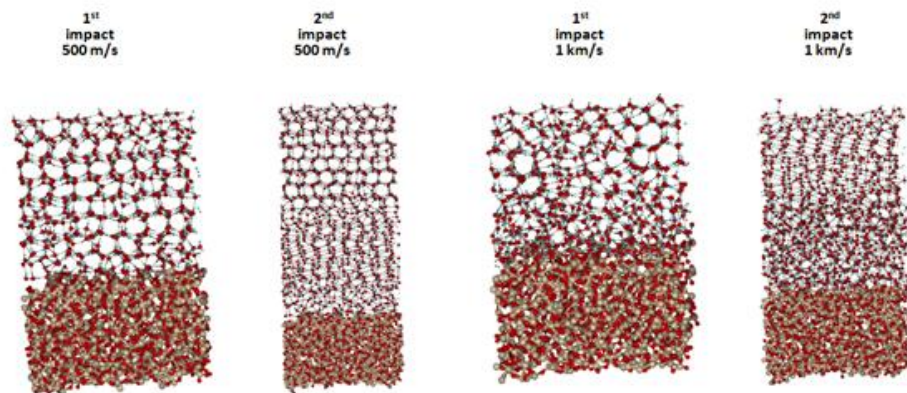


Figure 33. First and second impacts of crystal ice on suboxide silica surface at 500 m/s and 1 km/s impact velocities

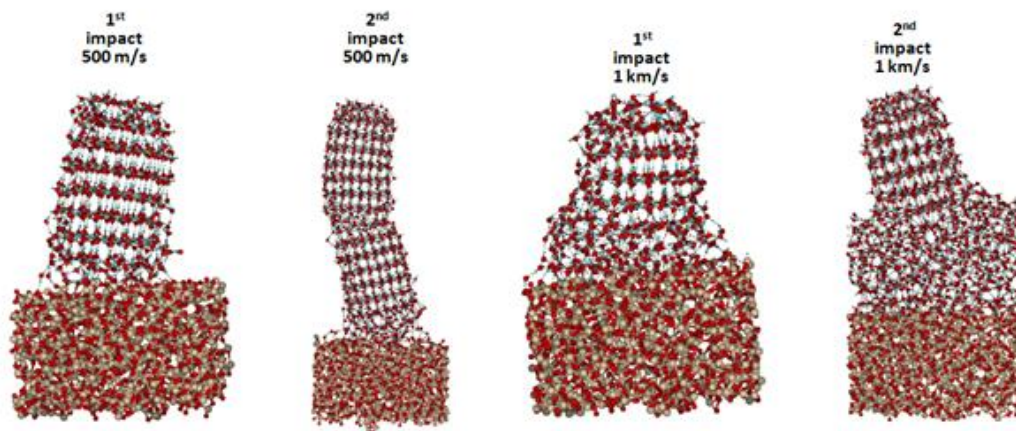


Figure 34. Side view of first and second impacts of crystal ice on suboxide silica surface at 500 m/s and 1 km/s impact velocities

In order to calculate the TC values for the deposited ice in these cases, the dual thermostat method is applied to two layers of the ice. Therefore, two values of TC are obtained for each case. Generally the TC values are higher for the top ice layers because there is no silica interface for the top layer and less irregularity is created in the ice structure at the top layers. This can be directly observed in Figures 33 and 34. The RDF graphs of top and bottom layers of crystal ice clusters after the second impact on the suboxide silica surface

are shown in Figure 35. This graph shows that the top layer retains the crystal structure better than the lower layer. The TC values are obtained by calculating the TC values at top and bottom layers. These values and the average TC values are mentioned in Tables 17-20. The TC average values are generally higher than the values obtained for the deposited ice clusters after the first impacts because the TC values obtained for the top layers are closer to the TC values for separate ice clusters and therefore, the average will be higher.

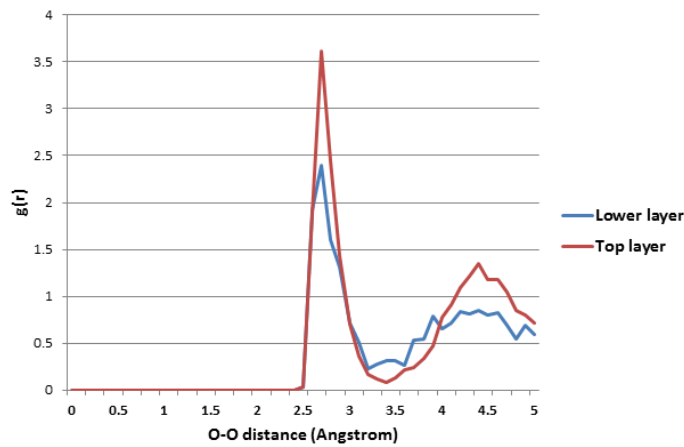


Figure 35. RDF graphs of the top and bottom layers of crystal ice cluster after two successive 1km/s impacts on the surface of suboxide silica

Table 17 ReaxFF values of the thermal conductivity of amorphous ice depositing on the fully oxidized silica

Deposition condition	Thermal conductivity (W/m.K)	TC Average value
500 m/s impact( <i>Bottomlayer /Toplayer</i> )	0.53	0.87
	1.20	
1km/s impact( <i>Bottomlayer /Toplayer</i> )	0.54	0.9
	1.25	

**Table 18 ReaxFF values of the thermal conductivity of amorphous ice depositing on the suboxide silica**

Deposition condition	Thermal conductivity (W/m.K)	TC Average value
500 m/s impact ( <i>Bottomlayer /Toplayer</i> )	0.57	0.77
	0.96	
1 km/s impact ( <i>Bottomlayer /Toplayer</i> )	0.54	0.8
	1.05	

**Table 19 ReaxFF values of the thermal conductivity of crystal ice depositing on the fully oxidized silica surface**

Deposition condition	Thermal conductivity (W/m.K)	TC Average value
500 m/s impact( <i>Bottomlayer /Toplayer</i> )	1.19	1.44
	1.69	
1 km/s impact( <i>Bottomlayer /Toplayer</i> )	1.26	1.31
	1.37	

**Table 20 ReaxFF values of the thermal conductivity of crystal ice depositing on the suboxide silica surface**

Deposition condition	Thermal conductivity (W/m.K)	TC Average value
500 m/s impact( <i>Bottomlayer /Toplayer</i> )	1.12	1.66
	2.2	
1 km/s impact( <i>Bottomlayer /Toplayer</i> )	1.07	1.2
	1.33	

### 5.2.3 Influence of adding ionic 1-Butyl-3-methylimidazolium (BMIM) in the bulk of the amorphous ice cluster on the ice cluster TC value

In many situations, especially at the thruster exit, there is possibility of presence of ionic species that can mix in the bulk of the ice clusters. As such, investigating the effect of presence of ionic species in the bulk of ice clusters on the values of the TC is another point of interest in these studies. In order to study the effect of ionic species, we mixed 400 ice molecules with 12 ionic 1-Butyl-3-methylimidazolium (BMIM) molecules and equilibrated the system at 150K (Figure 36). BMIM is an ionic liquid fuel with hypergolic reaction capabilities. These types of ionic liquids can mix with ice clusters at the exit of the thrusters and create ionic ice clusters.

The TC calculations for such mixtures show a drop in the TC values (Table 21). This reduction in TC can be attributed to the more irregularity imposed on the ice structure caused by the presence of the ionic BMIM.

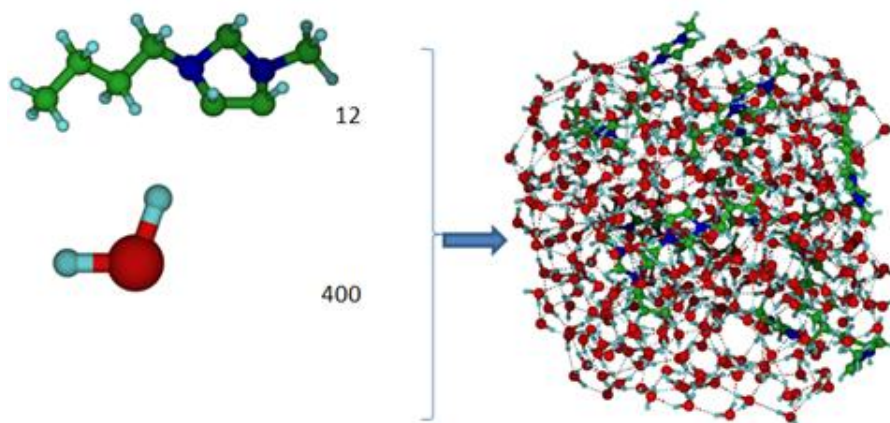


Figure 36. Amorphous ice cluster mixed with ionic BMIM

Table 21 ReaxFF values of the thermal conductivity of amorphous ice containing ionic BMIM depositing on the silica surface

Silica type	Thermal conductivity (W/m.K)
Fully oxidized silica	0.53
Suboxide silica	0.32

## **6. Defect formation in graphene under noble gas ion irradiation**

The discovery of graphene has brought some of the most exciting properties of materials in technological applications. It is made by isolating single two dimensional atomic layers of graphite. The strongest bond in nature, the C-C bond covalently locks these atoms in place resulting in remarkable mechanical properties. A suspended single layer of graphene is one of the stiffest known materials characterized by a remarkably high Young's modulus of  $\sim 1$  TPa. Graphene is five times stiffer and two orders of magnitude stronger than steel. Therefore, if we can overcome the limitations on production of graphene including size and price, this material can revolutionize the material industry. Graphene shows great heat dissipation and the capability to bear large current density. Therefore, the last decade has witnessed the flourishing of graphene in many areas from fundamental science to practical applications.

However, defects can deteriorate the useful properties of graphene based materials in radiation hostile environments, such as outer space. However, a pristine graphene is not always necessary or even desirable. Careful manipulation of graphene structure via ion irradiation can be used to tailor the properties. In this study, defect formation via energetic noble gas irradiation in graphene is investigated. In order to study defect formation under noble gas irradiation in graphene, an extensive set of reactive molecular dynamics simulations have been conducted.

In this study, the atomistic scale details of Kr ion impacts causing defect formation and the associated dynamic processes involved in the irradiations and during subsequent relaxation are analyzed.

## 6.1. Defect structures in graphene

As mentioned before, defects in graphene can affect graphene's electrical, mechanical, optical and thermal properties. In this section, most common defects in graphene structure will be introduced.

Stone-Wales (SW) defect does not involve removal or addition of carbon atoms. As shown in Figure 37, in this type of defect, four hexagons evolve into two heptagons and two pentagons[101]. SW defects can be very stable once formed because the formation energy for the defect is about 5 eV and a kinetic energy barrier of about 10 eV needs to be overcome to create this type of defect[102].

The formation energy for a mono vacancy (MV) that one carbon atom is knocked out of the graphene structure is about 7.5 eV. This type of vacancy is shown in Figure 38.

A double vacancy (DV) defect can be formed by merging two mono vacancies or by removing two adjacent carbon atoms. This defect can emerge in different configurations. Figure 39 shows some of the most common types of DV defects. The migration energy for a mono vacancy is about 1.3eV and for a double vacancy is about 7eV. Therefore, the MV can move around much more easily compared to DV.

In Frenkel defect an atom is displaced from its original position to another site, creating a vacancy at the original site and a defect at the new location. Some of the most common Frenkel defects are shown in Figure 40.

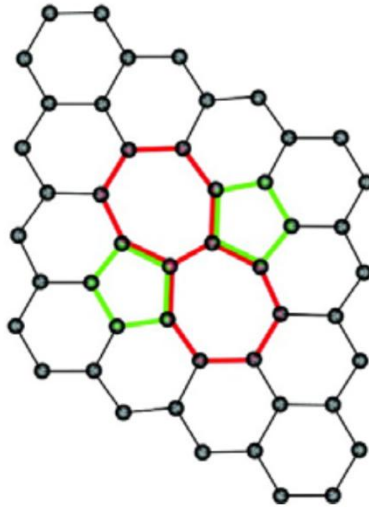


Figure 37. Stone-Wales defect in graphene

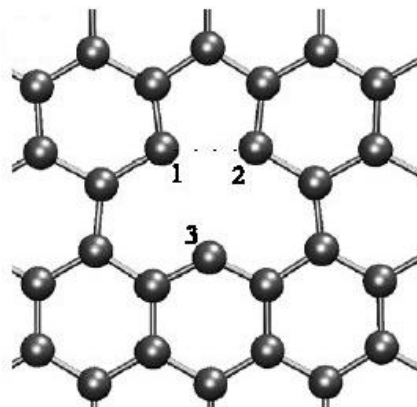


Figure 38. Mono Vacancy defect in graphene

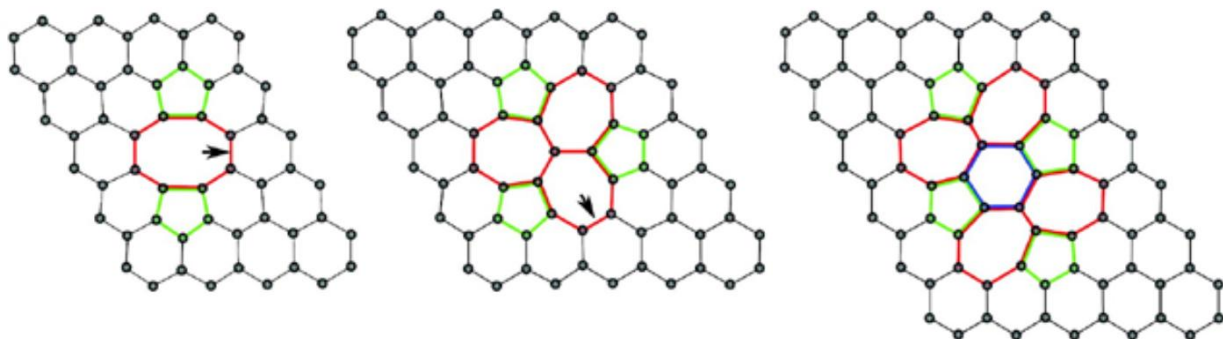


Figure 39. Some common types of double vacancy defects in graphene

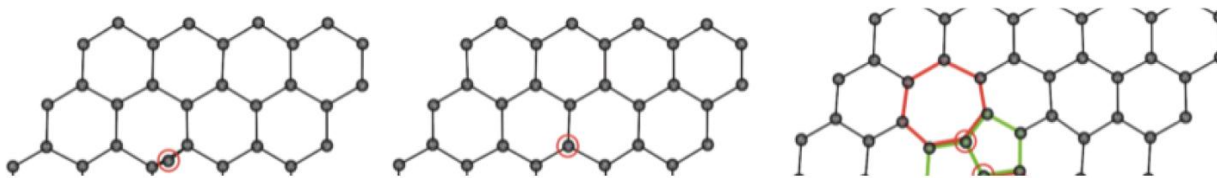


Figure 40. Some common types of Frenkel defects in graphene

## 6.2 Computational Method

For performing high energy Kr impacts on the graphene surface, molecular dynamic simulations in microcanonical ensemble (NVE) were performed using ReaxFF reactive force field program. The force field used for these simulations was developed on the base of ReaxFF force field previously developed for reproducing the mechanical properties of materials made with carbon[103]. For including Kr repulsive interactions with graphene, Density Functional Theory (DFT) and Ziegler-Biersack-Littmark (ZBL) universal repulsive potential calculations are used to retrain the van der Waals and Morse potential parameters of the ReaxFF potential. Since noble gases are non-reactive, interaction between Kr atoms and graphene only can be represented by repulsive interaction. In order to obtain these training data, Kr atoms are located at three different locations with respect to a benzene ring at different distances (Figure 41). The DFT calculations are performed using LACV3P\*\* basis set and B3LYP functional. The force field retraining results are shown in Figure 41.

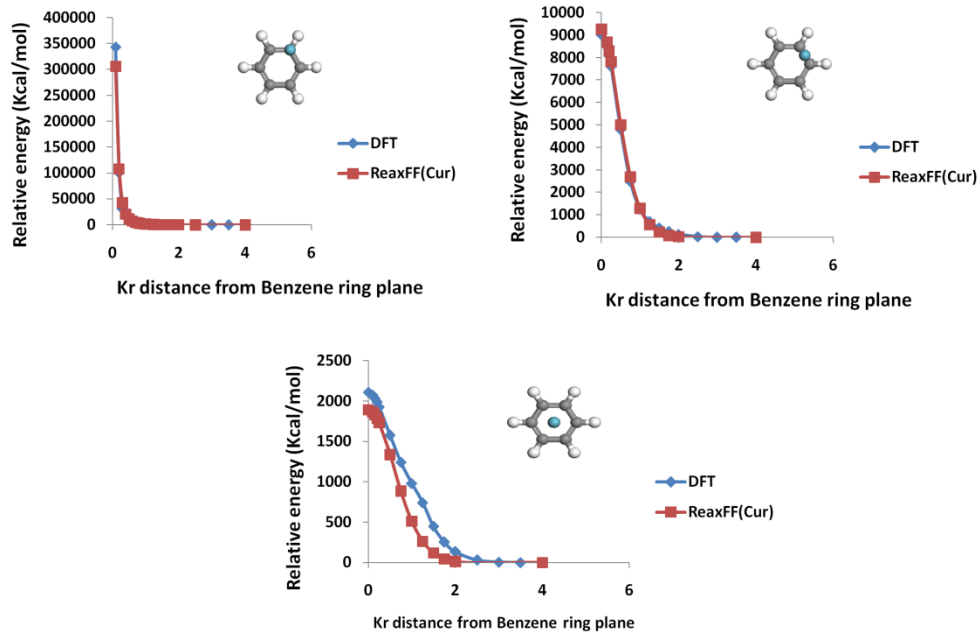


Figure 41. Force field training results of Carbon-Krypton interactions

The graphene sheet with dimensions of  $52 \times 40 \text{ \AA}^2$  is fully equilibrated at 300K prior to Kr irradiation. After the graphene equilibration, Kr ions are irradiated in the middle of the graphene of dimension  $30 \times 20 \text{ \AA}^2$  with impact energy of 25keV. To ensure conservation of energy during the hypervelocity  $\text{Kr}^+$  impacts, the small time step of the molecular dynamics simulation is chosen to be 0.02 fs. The dose of each  $\text{Kr}^+$  irradiation simulations was selected to be  $10^{14}$  ions/ $\text{cm}^2$ . Each irradiated graphene structure was annealed at 2000 K for 10 ps and cooled down to 300 K to eliminate any unrealistic configurations. In order to achieve statistically reliable results, total 100  $\text{Kr}^+$  irradiation on graphene simulations were performed.

### 6.3 Kr irradiation on graphene simulations results

The distributions of different defects after  $\text{Kr}^+$  impacts are shown in Table 22. These distributions are mentioned for two stages: before annealing and after annealing. In  $\text{Kr}^+$  irradiations, the mono-vacancy defect is the most frequent type of the defect observed. Based on the similar calculations for lighter noble gas impacts which are under study, in the lighter noble gas irradiations ( $\text{He}^+$ ), STW defects were the most frequently generated defect type, followed by Frenkel defects. The probability of generating mono-vacancy defects is negligible in  $\text{He}^+$  irradiations. The reason for having more vacancy-type defects in  $\text{Kr}^+$  irradiations is the larger amount of energy transfer between ions and graphene after impact, which was caused by larger collision cross-sections. In  $\text{He}^+$  irradiations, formation of STW and Frenkel defects, which required a lower amount of energy, are most frequently observed. The number of sputtered atoms per ion impact for  $\text{Kr}^+$  was measured to be 0.55 which is in good agreement with previous studies[104].

Table 22 Percentage of different defects in the  $\text{Kr}^+$  irradiated graphene

	MV	SW	Frenkel	DV
Before Annealing	77	6.1	10.8	6.1
After Annealing	78.8	9.5	4.8	6.9

In order to analyze the defect structures immediately after the irradiations, the distribution of adatoms from their original site (center of vacancy) are evaluated. The results are shown in Figures 42 and 43. With  $\text{He}^+$  irradiation, all the adatoms are distributed within 5 Å, while, in the irradiations of  $\text{Kr}^+$  ions, some adatoms were displaced even more than 10 Å. The heavier  $\text{Kr}^+$  ions transfer more energy to adatoms which causes displacement of carbon atoms farther away

along the graphene and finally trapped by other Carbon atoms of graphene. The peaks of adatoms displacements are observed at approximately 3 Å in both light and heavier ion irradiations.

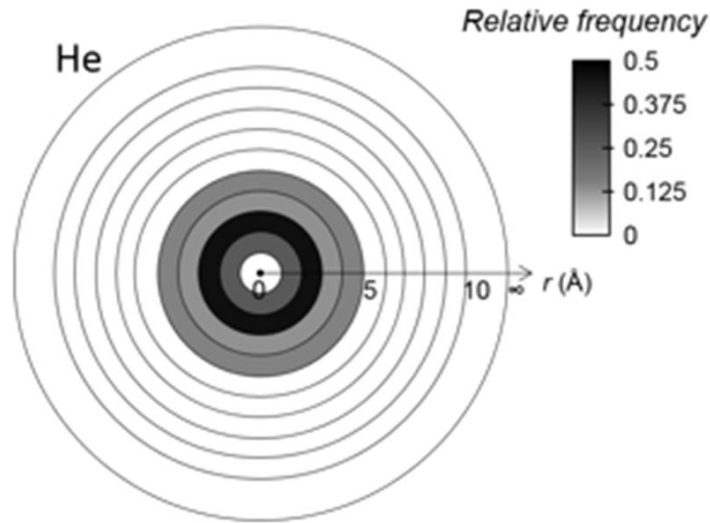


Figure 42. Adatoms distribution from their original lattice position after He<sup>+</sup> irradiations on graphene

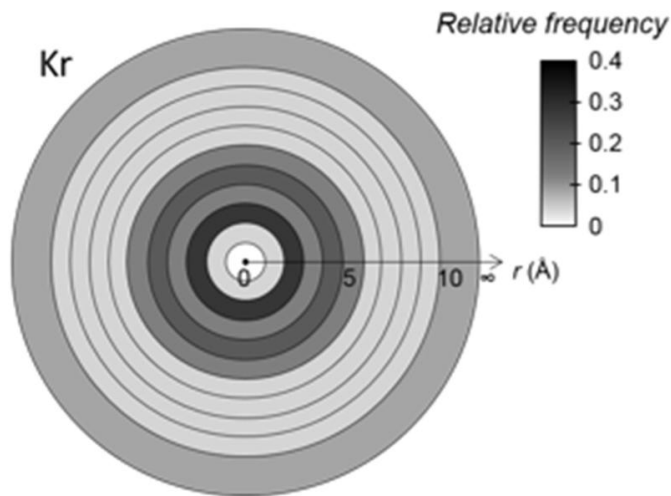


Figure 43. Adatoms distribution from their original lattice position after Kr<sup>+</sup> irradiations on graphene

## 7. Electron-induced degradation of Kapton

Kapton polyimide can be exposed to high-energy electrons, protons, heavy ions, vacuum ultraviolet and cosmic radiations in space environment. In the geosynchronous orbit, high energy electrons and protons are the main radiation factors in this environment. Under these conditions, major structural transformations in the Kapton, such as chain scission and cross-linking events can take place. These transformations can result in changes in the properties of the polymer like thermal conductivity, dielectric constant, etc. The concentration of the aromatic groups can offer protection against structural damage on exposure to electron or gamma irradiations.

Furthermore, radiation processing has emerged as a time saving and easy-to-control method to bring about desired modifications in polymers. Among several types of radiations that can be used for radiation processing, high-energy electrons are of particular interest for polymers, due to their high dose rates and consequently high-energy deposition in small time intervals.

There are a very few studies on evaluating the effects of radiation on mechanical and the structural properties of polyimides. Therefore, in the present work, we recently developed a new, ReaxFF-based, framework for studying electron beam damage in polymers.

Electron irradiation is another important type of irradiation that should be studied in more details. In this study, using ReaxFF molecular dynamics simulation of electron irradiation on Kapton, the effect of electron irradiation and the electron energy transfer to Kapton structure and the consequent changes in Kapton structure are evaluated using reactive molecular dynamics simulations.

## 7.1 Method description

In this work the effect of electron beam irradiation at different random points of Kapton is evaluated using ReaxFF molecular dynamics simulation. The Kapton structure is prepared with 7 long Kapton monomers ( $C_{110}H_{52}O_{25}N_{10}$ ). The initial configuration of the Kapton structure while the first electron beam is irradiated on it is shown in Figure 44. The Kapton structure is equilibrated at 300K before exposure to the electron beams. After equilibration, the electron beams are irradiated at different random locations of Kapton (Figure 45). Each electron beam is turned on for 1fs or 2fs at two different electron beam irradiation simulations. This electron beam irradiation on Kapton simulation procedure is shown in Figure 46. Experimental studies show that electron beams penetrate to a certain depth in Kapton and the energy of the electron beam gets dissipated in the bulk of Kapton [89]. These experimental results show that simulation of electron beams inside Kapton using stationary strings of charged particles can be a reasonable assumption. Therefore, in this study, each electron beam is modeled with a string of dummy atoms along the Kapton structure. In order to model this string of dummy atoms as an electron beam, a charge of -1 is added to each dummy atom at the time that the electron beam is supposed to be irradiated at a particular location. When it is time to turn off this particular electron beam, the charges of dummy atoms are changed back to zero value. Using this method, we could model an electron beam at each random location of Kapton.

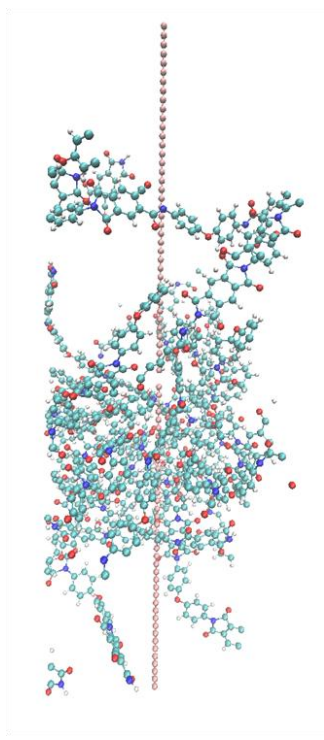


Figure 44. Initial configuration of Kapton at the start of electron beam irradiation

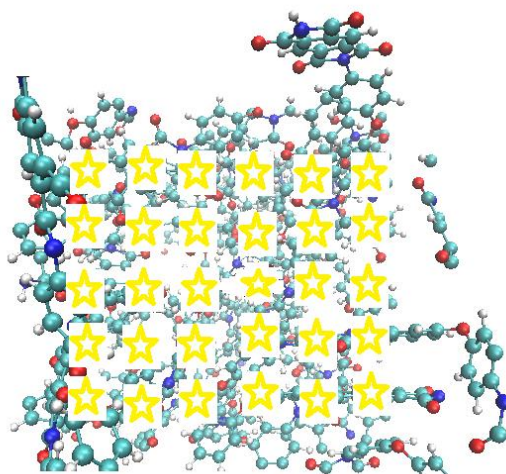


Figure 45. Random locations of electron beam irradiation on Kapton

For the simulation with 1fs electron beam exposure, total of 30 electron beams are irradiated on Kapton and for the simulation with 2fs electron beam exposure, total of 25 electron beams are irradiated.

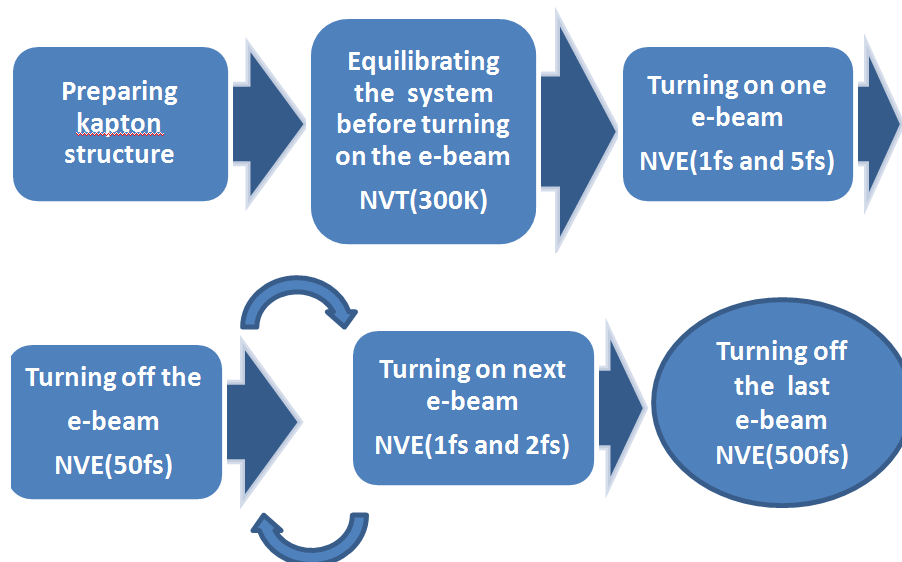


Figure 46. Electron beams irradiations on Kapton ReaxFF molecular dynamics simulation procedure

## 7.2 Electron beam irradiation on Kapton results and discussions

As mentioned previously, changing the time of electron beam irradiation can change the amount of energy transferred to the Kapton structure. Total energy transferred after thirty 1fs and twenty five 2fs electron beam irradiations are 112 eV and 363 eV respectively. The final temperatures of Kapton structures at the end of these simulations are around 800K and 1900K for these two electron beam irradiation simulations. The temperature evolutions are shown in Figures 47 and 48.

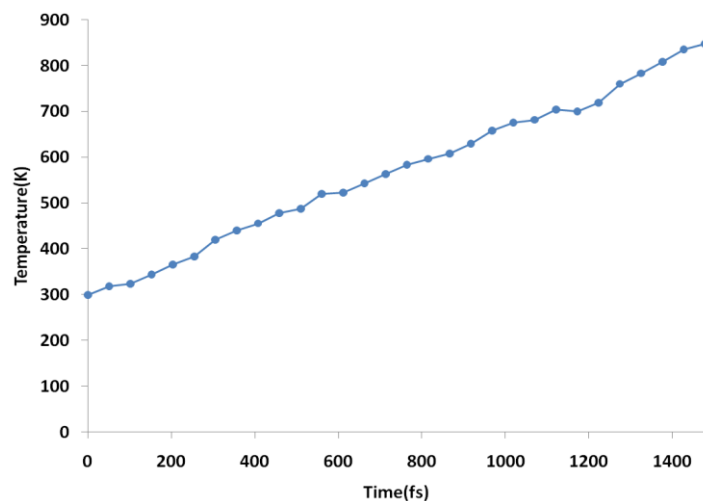


Figure 47. Temperature evolution of Kapton during 30 electron beam irradiation. Each electron beam is turned on for 1 fs. Each point on the graph is the time that on electron beam is irradiated.

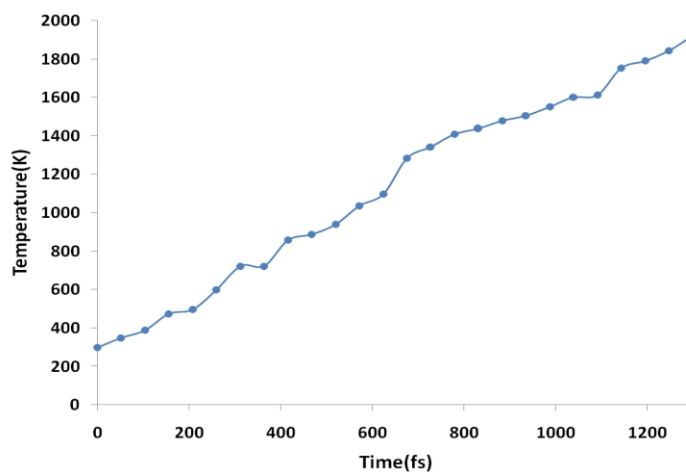


Figure 48. Temperature evolution of Kapton during 25 electron beam irradiation. Each electron beam is turned on for 2 fs. Each point on the graph is the time that on electron beam is irradiated.

The compositions of Kapton structure at the start of simulations and at the end of the simulations are shown in Tables 23, 24, 25.

Table 23 Molecular composition of Kapton structure at the start of simulations

Number of molecules	Molecular Formula	Molecular Mass
7	$C_{110}H_{52}O_{25}N_{10}$	1912.39

Table 24 Molecular composition of Kapton structure at the end of 1fs irradiations simulation

Number of molecules	Molecular Formula	Molecular Mass
1	$C_{110}H_{53}O_{25}N_{10}$	1913.40
4	$C_{110}H_{52}O_{25}N_{10}$	1912.39
2	$C_{110}H_{51}O_{25}N_{10}$	1911.38
1	H	1

Table 25 Molecular composition of Kapton structure at the end of 2fs irradiations simulation

Number of molecules	Molecular Formula	Molecular Mass
1	$C_{115}H_{51}O_{25}N_{10}$	1971.3830
1	$C_{110}H_{53}O_{25}N_{10}$	1913.3990
2	$C_{110}H_{52}O_{25}N_{10}$	1912.3910
1	$C_{100}H_{48}O_{21}N_8$	1696.3630
1	$C_{72}H_{35}O_{16}N_6$	1239.264
1	$C_{62}H_{21}O_{15}N_6$	1089.1530
1	$C_{34}H_{19}O_6N_2$	551.146
1	$C_{10}H_2O_4N_2$	214.012
1	$C_9H_3O_4N$	189.02
1	$C_{10}H_4O_3N$	186.029
1	$C_8H_3O_2$	131.022
1	$C_6H_4$	76.032
1	$C_3HO$	53.007
1	$C_3O$	51.999
1	$C_4H$	49.008
1	CHON	43.007
1	CON	41.999
2	CN	26
14	H	1.008

Experimental results show that Kapton starts to decompose at a temperature around 794 K(Dupont Kapton Polyimide Film General Specifications). This is consistent with the observations in our molecular dynamics simulations.

In an experiment performed by our colleagues at Air Force Research Laboratory (AFRL), Kapton film was irradiated with low-energy electron beam (0.5 keV) for 15 hrs. RGA spectra were taken every 20 minutes. The background spectrum was obtained after averaging of three RGA spectra taken sequentially with no electron beam on the sample. Table 26 summarizes the atomic masses of the observed peaks at different times in five different atomic mass unit (amu) regions. Below 45 amu peaks were not considered due to high intensity peaks of residual impurities presented in the chamber. The peak 2 is the most observed peak based on these observations. This has been verified in the distribution of the first molecules in the molecular dynamics simulations.

**Table 26 Atomic masses of the observed peaks at different times in five different atomic mass unit (amu) regions after low energy electron beam irradiation experiment**

<b>Time (min)</b>	<b>Peak 1 45-50 amu</b>	<b>Peak 2 50-60 amu</b>	<b>Peak 3 60-70 amu</b>	<b>Peak 4 70-80 amu</b>	<b>Peak 5 80-90 amu</b>	<b>Peak 6 90-100 amu</b>
20				73.4	88.8	
60	46.1	59.2	68.5		83.8/89.7	96.7
100						
140	48.5	55.2		72.6		92.6
180		55.6		79.1		
220	45.8	55.1/58.2				96.2
260	46	55.8		70.2		98.1
300	45.4	55.1		70.1	82.8	98.1
340			69.4		89.7	
380		54.9				
420		55.8		75.6		
460		55.8				
500		55.3			85.1	99.4
540						
580				70.3		
620						
660		55.2				
700						
740						96.8
780	48.6		65.8			
820		54.5				92
860				73.2		94.9
900			60.4	72.6	86.0	

## 8. Conclusions

Our ReaxFF simulations of Kapton, Kapton-POSS (polyhedral oligomeric silsesquioxane), amorphous silica and Teflon subject to the high energy AO (Atomic Oxygen) collision indicate that the amorphous silica shows the highest stability among these materials. However, once the disintegration of the silica starts under AO collision, it continues with a very high rate, due to the high exothermicity of silicon oxidation.

During the Kapton AO impact simulation, the initial gas-phase species are dominated by  $\text{H}_2\text{O}$ ,  $\text{O}_2$  while lower quantities of  $\text{H}$  and  $\text{OH}$ -radicals are observed, together with a wide range of larger Kapton degradation products. In the simulation in which POSS material is subject to AO collisions, initial gas species also contain  $\text{CO}$  and  $\text{CO}_2$ . In contrast, for the silica AO impact, the initial gas phase products are  $\text{O}_2$  and light silicon oxides and later, heavier silicon oxides appear as the gas phase. Similar to silica, Teflon shows very good stability while first 50 atomic Oxygens are impacted on its surface. With continuing the AO collision, Carbonyl fluorides are observed as the first molecules separating from the surface of the Teflon.

Comparing the stabilities of Kapton and Kapton-POSS stabilities under AO collision shows that adding silicon to the bulk of the Kapton structure enhances the stability of the structure against AO impact.

The NVT simulation results for controlling the temperature evolution of the Kapton-POSS material shows that heat transfer in the material during AO impact can provide a considerable decrease in the disintegration of the material. This effect is specially observed in silica AO collision and by lowering the temperature of the material using thermostats the stability of silica is increased considerably.

Comparing the simulation results to experimental results of AO erosion yield of Materials International Space Station Experiment 2 (MISSE 2) shows that the erosion yields of Kapton and Teflon at first stages of the simulation are close to the experiment results and Teflon shows lower erosion yield compared to Kapton.

Changing the Silicon content and also using other enhancement methods for Kapton material like the effect of different ions additives in the bulk of Kapton can enhance the stability of the Kapton structure in the low earth orbital environment, but the effect of these changes on the material characteristics like brittleness should be evaluated and the best material composition should be figured out considering all the limitations. As these simulations demonstrate, ReaxFF can provide a cost effective screening tool for such material optimization.

The ReaxFF simulations of crystal and amorphous ice cluster impacts on fully oxidized and suboxide silica structures at 1 km/s, 4 km/s and 7 km/s impact velocities indicate that at higher impact velocity more fragments are bouncing back from the surface. After ice cluster impacts on fully oxidized silica surfaces, more different types of fragments are observed bouncing back from the surface compared to the ice cluster impacts on suboxide silica surfaces. More water dissociations are observed in the case of amorphous ice cluster impacts compared to crystal ice cluster impacts.

Multiple ice cluster impacts on the silica surfaces at these three different impact velocities show that at 1 km/s ice cluster impact for both crystal and amorphous ice impacts the entire ice cluster accretes on the surface. With increasing the ice cluster impact velocities to 4 km/s and 7 km/s the amount of ice accretion decreases. Generally, at different ice cluster impact velocities, the ice accretion is more on suboxide silica compared to fully oxidized silica surfaces. The sticking

coefficients of these ice clusters are calculated by normalizing the number of H and O atoms attaching to the silica surfaces. These calculations show that the sticking coefficients for crystal ice clusters are higher than amorphous ice clusters for 4 km/s and 7 km/s impacts.

The simulation of ice cluster impacts on the surfaces that are completely covered with ice layers, show that when the silica surfaces are completely covered with ice layers, the 7 km/s ice impacts cause removal of ice molecules from the accumulated ice for both crystal and amorphous ice cluster impacts. However, crystal ice clusters impacting at 4km/s cause ice accumulation and amorphous ice clusters impacting at 4 km/s cause ice removal.

Analysis of the ice clusters temperatures during the collisions show that the electron excitation issue might be important at impact velocity of 10 km/s and higher.

From this study we have obtained a better understanding of the physicochemical processes of ice cluster hypervelocity collisions on silica surfaces. In future work, we aim to expand on the results presented here to evaluate the effect of these impacts on the mechanical properties of the materials and developing a better understanding of the interactions between quantum level, molecular level and experimental results.

The thermal conductivities of ice clusters deposited on silica surfaces are calculated. The ReaxFF reactive force field molecular dynamics simulations of the thermal conductivity (TC) values of crystal and amorphous ice clusters show good agreement with the available experimental TC values. Our results show that the TC value of crystal ice is higher than amorphous ice.

A dual thermostat method is applied to calculate the thermal conductivities. The simulation results show that TC values of the ice clusters decrease after deposition on silica surfaces. Generally, this decrease in TC value is higher in the case of ice deposition

on suboxide silica compared to fully oxidized silica surfaces. This is because of the loss of crystallinity in the ice clusters after deposition on suboxide silica surface.

The effect of 500 m/s and 1 km/s impact velocities of the ice clusters on the silica surfaces on the TC values are evaluated. The results show that 500 m/s impact velocity does not reduce the TC values significantly. But, at 1 km/s impact velocities, the crystal ice lose the crystal structure at its lower layers and this causes a considerable drop in the TC value of the crystal ice cluster deposited on the silica surface after 1 km/s impacts. Studies of the ice clusters after the second impacts show that the top layers of the deposited ice which come from the second ice clusters impacting on the top of the deposited first ice clusters, get less deformed. Therefore, the main contribution in the decrease of the TC values of the ice clusters is from the bottom layers of the deposited ice clusters.

Our calculations also show adding ionic species to the bulk of the ice clusters cause decrease in the value of the TC.

The effect of noble gas ion irradiation on defect type and defect evolution in graphene is investigated using ReaxFF reactive molecular dynamics simulation.

This study shows that high energy 25 keV impact of  $\text{Kr}^+$  noble gas ions can mostly create mono vacancy defect while lighter noble gas ions like  $\text{He}^+$  can mostly create Stone-Wales defect in graphene. In order to simulate the defects reconstruction into more stable configurations, the graphene sheets are annealed at 2000K for 10 ps after noble gas ion irradiations. The reconstruction of Frenkel defects, which were the second most-frequently observed defect type, was analyzed. In most cases, they were reconstructed into STW defects, healed forming 6-

member rings, or some other complex defects, in which adatoms were merged into pre-existing complex defects.

Lastly, electron beam irradiation on Kapton is modeled to understand the details of chemical composition change and temperature evolution of Kapton. Two different conditions are applied for electron beam irradiation in two different sets of simulations. In the first set of simulations, 30 electron beams are irradiated at random different locations and each electron beam is turned on for 1fs sequentially. In the second set of simulations, 25 electron beams are irradiated at random different locations and each electron beam is turned on for 2fs sequentially. The time of electron beam irradiation determines the amount of energy transferred to the Kapton. 1fs electron beam irradiations causes the first material decomposition observed at the moment that Kapton temperature is around 800K which is the experimental decomposition temperature observed for Kapton. 2fs electron beam irradiation causes first decomposition at total system temperature around 600K. This happens because of higher energy transferred per each electron beam to the Kapton. Firstly small molecules start to separate from Kapton and with continuing the electron beam irradiation, heavier molecules start to separate from Kapton. Electron beam irradiation experiments are performed with low energy electron beams for 900 minutes. The molecules separated from Kapton during electron beam irradiations are studied and the atomic masses of these molecules are classified in different regions. The atomic masses of the first molecules separating from the Kapton structure in molecular dynamics simulations agree with experimental results.

As mentioned previously, the surface of spacecraft is exposed to different irradiations and collisions that can cause degradation of materials on the surface of spacecraft. These conditions can include AO impact, UV irradiation, different ions irradiations, debris collisions and electron

irradiation. Studying the combined effect of these conditions can be an important enhancement in moving towards better modeling of material degradation in space condition.

In ice impact simulations, an important parameter that can affect the sticking coefficients of the ice clusters is the size of the ice clusters. Studying the relation between sticking coefficient and ice cluster size can be another point of interest for the future studies.

Using molecular modeling methods we can study the mechanical properties of different materials before and after exposure to the extreme space conditions mentioned in this study. Using these methods, the performance of these materials after exposure to extreme atmosphere and their qualities for further uses can be evaluated.

# References

- [1] J. A. King, D. R. Klimek, I. Miskioglu, and G. M. Odegard, "Mechanical properties of graphene nanoplatelet/epoxy composites," *Journal of Composite Materials*, vol. 49, pp. 659-668, Mar 2015.
- [2] T. Kuilla, S. Bhadra, D. H. Yao, N. H. Kim, S. Bose, and J. H. Lee, "Recent advances in graphene based polymer composites," *Progress in Polymer Science*, vol. 35, pp. 1350-1375, Nov 2010.
- [3] M. A. Rafiee, J. Rafiee, Z. Wang, H. H. Song, Z. Z. Yu, and N. Koratkar, "Enhanced Mechanical Properties of Nanocomposites at Low Graphene Content," *Acs Nano*, vol. 3, pp. 3884-3890, Dec 2009.
- [4] L. C. Tang, Y. J. Wan, D. Yan, Y. B. Pei, L. Zhao, Y. B. Li, *et al.*, "The effect of graphene dispersion on the mechanical properties of graphene/epoxy composites," *Carbon*, vol. 60, pp. 16-27, Aug 2013.
- [5] J. M. Zhang and T. K. Minton, "Production of volatile CO and CO<sub>2</sub> from oxidized polyethylene and graphite surfaces by hyperthermal atom-surface collisions," *High Performance Polymers*, vol. 13, pp. S467-S481, Sep 2001.
- [6] H. X. Teng, "Overview of the Development of the Fluoropolymer Industry," *Applied Sciences-Basel*, vol. 2, pp. 496-512, Jun 2012.
- [7] G. Son and C. G. Kim, "Protective effect of nanocomposite film from the low earth orbit environment," *Journal of Composite Materials*, vol. 49, pp. 2297-2306, Aug 2015.
- [8] S. Koontz, L. Leger, K. Albyn, and J. Cross, "VACUUM ULTRAVIOLET-RADIATION ATOMIC OXYGEN SYNERGISM IN MATERIALS REACTIVITY," *Journal of Spacecraft and Rockets*, vol. 27, pp. 346-348, May-Jun 1990.

- [9] J. Kleiman and Z. Iskanderova, *Protection of Materials and Structures from Space Environment: Icpmse-6*: Springer Netherlands, 2003.
- [10] S. J. Tomczak, M. E. Wright, A. J. Guenther, B. J. Pettys, A. L. Brunsvold, C. Knight, *et al.*, "Space Survivability of Main-Chain and Side-Chain POSS-Kapton Polyimides," in *Protection of Materials and Structures from Space Environment*. vol. 1087, J. I. Kleiman, Ed., ed Melville: Amer Inst Physics, 2009, pp. 505-518.
- [11] M. J. Buehler, A. C. T. van Duin, and W. A. Goddard, "Multiparadigm modeling of dynamical crack propagation in silicon using a reactive force field," *Physical Review Letters*, vol. 96, Mar 2006.
- [12] K. Chenoweth, A. C. T. van Duin, and W. A. Goddard, "ReaxFF reactive force field for molecular dynamics simulations of hydrocarbon oxidation," *Journal of Physical Chemistry A*, vol. 112, pp. 1040-1053, Feb 2008.
- [13] K. D. Nielson, A. C. T. van Duin, J. Oxgaard, W. Q. Deng, and W. A. Goddard, "Development of the ReaxFF reactive force field for describing transition metal catalyzed reactions, with application to the initial stages of the catalytic formation of carbon nanotubes," *Journal of Physical Chemistry A*, vol. 109, pp. 493-499, Jan 2005.
- [14] J. G. O. Ojwang, R. van Santen, G. J. Kramer, A. C. T. van Duin, and W. A. Goddard, "Predictions of melting, crystallization, and local atomic arrangements of aluminum clusters using a reactive force field," *Journal of Chemical Physics*, vol. 129, Dec 2008.
- [15] A. Rahnamoun and A. C. T. van Duin, "Reactive Molecular Dynamics Simulation on the Disintegration of Kapton, POSS Polyimide, Amorphous Silica, and Teflon during Atomic Oxygen Impact Using the Reaxff Reactive Force-Field Method," *Journal of Physical Chemistry A*, vol. 118, pp. 2780-2787, Apr 2014.

- [16] A. Rahnamoun and A. C. T. van Duin, "Study of thermal conductivity of ice clusters after impact deposition on the silica surfaces using the ReaxFF reactive force field," *Physical Chemistry Chemical Physics*, vol. 18, pp. 1587-1594, Jan 2016.
- [17] A. Strachan, E. M. Kober, A. C. T. van Duin, J. Oxgaard, and W. A. Goddard, "Thermal decomposition of RDX from reactive molecular dynamics," *Journal of Chemical Physics*, vol. 122, Feb 2005.
- [18] A. Strachan, A. C. T. van Duin, D. Chakraborty, S. Dasgupta, and W. A. Goddard, "Shock waves in high-energy materials: The initial chemical events in nitramine RDX," *Physical Review Letters*, vol. 91, Aug 2003.
- [19] A. C. T. van Duin, S. Dasgupta, F. Lorant, and W. A. Goddard, "ReaxFF: A reactive force field for hydrocarbons," *Journal of Physical Chemistry A*, vol. 105, pp. 9396-9409, Oct 2001.
- [20] N. Chaâbane, G. Jundt, H. Vach, D. M. Koch, and G. H. Peslherbe, "Cage effects and rotational hindrance in the surface scattering of large (N<sub>2</sub>)<sub>n</sub> clusters," *International Journal of Mass Spectrometry*, vol. 220, pp. 159-170, 2002.
- [21] W. Christen and U. Even, "Collision-induced fragmentation and neutralization of methanol cluster cations," *The European Physical Journal D-Atomic, Molecular, Optical and Plasma Physics*, vol. 16, pp. 87-90, 2001.
- [22] W. Christen and U. Even, "Hyperthermal surface-collisions of water cluster cations," *The European Physical Journal D-Atomic, Molecular, Optical and Plasma Physics*, vol. 24, pp. 283-286, 2003.
- [23] W. Christen, U. Even, T. Raz, and R. Levine, "Collisional energy loss in cluster surface impact: Experimental, model, and simulation studies of some relevant factors," *The Journal of chemical physics*, vol. 108, pp. 10262-10273, 1998.

- [24] F. Eusepi, A. Tomsic, and C. R. Gebhardt, "Analysis of solution-deposited alkali ions by cluster surface collisions," *Analytical Chemistry*, vol. 75, pp. 5124-5128, 2003.
- [25] C. Gebhardt, H. Schröder, and K.-L. Kompa, "Surface impact ionization of polar-molecule clusters through pickup of alkali atoms," *Nature*, vol. 400, pp. 544-547, 1999.
- [26] V. Gridin, C. R. Gebhardt, A. Tomsic, I. Schechter, H. Schröder, and K.-L. Kompa, "Surface impact induced fragmentation and charging of neat and mixed clusters of SO<sub>2</sub> and H<sub>2</sub>O," *International Journal of Mass Spectrometry*, vol. 232, pp. 1-7, 2004.
- [27] D. M. Koch, G. H. Peslherbe, and H. Vach, "Mechanisms of translational and rotational energy transfer in (N<sub>2</sub>)<sub>n</sub> cluster-surface scattering," *The Journal of Chemical Physics*, vol. 115, pp. 7685-7696, 2001.
- [28] T.V.Nguyen, D. M. Koch, G. H. Peslherbe, and H. Vach, "Molecular dissociation and vibrational excitation in the surface scattering of (N<sub>2</sub>)<sub>n</sub> and (O<sub>2</sub>)<sub>n</sub> clusters," *The Journal of chemical physics*, vol. 119, pp. 7451-7460, 2003.
- [29] A. Tomsic, P. U. Andersson, N. Marković, and J. B. Pettersson, "Collision dynamics of large water clusters on graphite," *The Journal of chemical physics*, vol. 119, pp. 4916-4922, 2003.
- [30] A. Tomsic, P. U. Andersson, N. Markovic, W. Piskorz, M. Svanberg, and J. B. Pettersson, "Molecular-dynamics simulations of cluster-surface collisions: Emission of large fragments," *The Journal of Chemical Physics*, vol. 115, pp. 10509-10517, 2001.
- [31] A. Tomsic and C. R. Gebhardt, "Molecular dynamics simulations of the micro-solvation of ions and molecules during cluster-surface collisions," *Chemical physics letters*, vol. 386, pp. 55-59, 2004.
- [32] A. Tomsic and C. R. Gebhardt, "A comparative study of cluster-surface collisions: Molecular-dynamics simulations of (H<sub>2</sub>O)<sub>1000</sub> and (SO<sub>2</sub>)<sub>1000</sub>," *The Journal of chemical physics*, vol. 123, p. 064704, 2005.

- [33] A. Tomsic, N. Markovic, and J. B. Pettersson, "Scattering of Ice particles from a graphite surface: A molecular dynamics simulation study," *The Journal of Physical Chemistry B*, vol. 107, pp. 10576-10582, 2003.
- [34] C. Anders, E. M. Bringa, G. Ziegenhain, and H. M. Urbassek, "Stopping of hypervelocity clusters in solids," *New Journal of Physics*, vol. 13, Nov 2011.
- [35] M. J. Eller, C. K. Liang, S. Della-Negra, A. B. Clubb, H. Kim, A. E. Young, *et al.*, "Hypervelocity nanoparticle impacts on free-standing graphene: A sui generis mode of sputtering," *Journal of Chemical Physics*, vol. 142, Jan 2015.
- [36] A. Gross and R. Levine, "Evanescent high pressure during hypersonic cluster-surface impact characterized by the virial theorem," *The Journal of chemical physics*, vol. 123, p. 194307, 2005.
- [37] R. Webb, M. Kerford, E. Ali, M. Dunn, L. Knowles, K. Lee, *et al.*, "Molecular dynamics simulation of the cluster-impact-induced molecular desorption process," *Surface and interface analysis*, vol. 31, pp. 297-301, 2001.
- [38] W. Zhu, Z. Pan, Y. Ho, and Y. Wang, "Simulations of C<sub>28</sub> chemisorption on diamond (001)-(2×1) surface: The comparison between cluster-cluster interaction and cluster-surface interaction," *Journal of Applied Physics*, vol. 88, pp. 6836-6841, 2000.
- [39] Z. Insepov, M. Sosnowski, and I. Yamada, "Molecular-dynamics simulation of metal surface sputtering by energetic rare-gas cluster impact," *Trans. Mater. Res. Soc. Jpn*, vol. 17, p. 111, 1994.
- [40] P. Melinon, V. Paillard, V. Dupuis, A. Perez, P. Jensen, A. Hoareau, *et al.*, "From free clusters to cluster-assembled materials," *International Journal of Modern Physics B*, vol. 9, pp. 339-397, 1995.

- [41] A. Terasaki, H. Yamaguchi, H. Yasumatsu, and T. Kondow, "Fragmentation dynamics of silicon cluster anions in collision with a silicon surface: contrast to aluminum cluster anions," *Chemical physics letters*, vol. 262, pp. 269-273, 1996.
- [42] A. Kaplan, A. Bekkerman, B. Tsipinyuk, and E. Kolodney, "Transition from during- to post-collision multifragmentation in cluster surface impact," *Physical Review B*, vol. 79, Jun 2009.
- [43] P. Larregaray and G. H. Peslherbe, "On the statistical nature of collision and surface-induced dissociation: A theoretical investigation of aluminum clusters," *Journal of Physical Chemistry A*, vol. 110, pp. 1658-1665, Feb 2006.
- [44] A. Lindblad, R. F. Fink, H. Bergersen, M. Lundwall, T. Rander, R. Feifel, *et al.*, "Post-collision interaction in noble gas clusters: Observation of differences in surface and bulk lineshapes," *Journal of Electron Spectroscopy and Related Phenomena*, vol. 156, pp. LX-LX, May 2007.
- [45] X. W. Luo, M. Wang, and B. T. Hu, "Molecular dynamics simulation of Cu-n clusters scattering from a single-crystal Cu(111) surface: The influence of surface structure," *Chinese Physics B*, vol. 25, Feb 2016.
- [46] W. U. Schroder, "Surface cluster emission in heavy-ion collisions," *Abstracts of Papers of the American Chemical Society*, vol. 229, pp. U304-U304, Mar 2005.
- [47] K. Wang, J. F. Liu, Q. H. Chen, W. M. Sun, A. Y. Ni, and C. Zhang, "Molecular dynamics simulation of impact of palladium clusters on the zirconium substrate," *Russian Journal of Physical Chemistry A*, vol. 90, pp. 383-389, Feb 2016.
- [48] S. Rutledge, J. Mihelcic, V. Srinivasan, and B. Bank, "Materials degradation in low Earth orbit," in *Proc. 119th TMS Minerals, Metals and Materials Annual Meeting and Exhibit, Anaheim, CA (February 18-22, 1990)*, 1990, pp. 35-48.
- [49] J. Madejski, "Droplets on impact with a solid surface," *International Journal of Heat and Mass Transfer*, vol. 26, pp. 1095-1098, 1983.

- [50] M. P. Allen and D. J. Tildesley, *Computer simulation of liquids*: Oxford university press, 1989.
- [51] Y. Chen, A. Chernatynskiy, D. Brown, P. K. Schelling, E. Artacho, and S. R. Phillpot, "Critical assessment of classical potentials for MgSiO<sub>3</sub> perovskite with application to thermal conductivity calculations," *Physics of the Earth and Planetary Interiors*, vol. 210, pp. 75-89, 2012.
- [52] A. Chernatynskiy, C. Flint, S. B. Sinnott, and S. R. Phillpot, "Critical assessment of UO<sub>2</sub> classical potentials for thermal conductivity calculations," *Journal of Materials Science*, vol. 47, pp. 7693-7702, 2012.
- [53] A. Chernatynskiy, R. W. Grimes, M. A. Zurbuchen, D. R. Clarke, and S. R. Phillpot, "Crossover in thermal transport properties of natural, perovskite-structured superlattices," *Applied Physics Letters*, vol. 95, p. 161906, 2009.
- [54] A. Chernatynskiy and S. R. Phillpot, "Evaluation of computational techniques for solving the Boltzmann transport equation for lattice thermal conductivity calculations," *Physical Review B*, vol. 82, p. 134301, 2010.
- [55] Y. He, I. Savić, D. Donadio, and G. Galli, "Lattice thermal conductivity of semiconducting bulk materials: atomistic simulations," *Physical Chemistry Chemical Physics*, vol. 14, pp. 16209-16222, 2012.
- [56] A. Henry and G. Chen, "High thermal conductivity of single polyethylene chains using molecular dynamics simulations," *Physical review letters*, vol. 101, p. 235502, 2008.
- [57] G. Hummer, J. C. Rasaiah, and J. P. Noworyta, "Water conduction through the hydrophobic channel of a carbon nanotube," *Nature*, vol. 414, pp. 188-190, 2001.
- [58] S. T. Huxtable, D. G. Cahill, S. Shenogin, L. Xue, R. Ozisik, P. Barone, *et al.*, "Interfacial heat flow in carbon nanotube suspensions," *Nature materials*, vol. 2, pp. 731-734, 2003.

- [59] Y. Liu, H. Yang, N. Liao, and P. Yang, "Investigation on thermal conductivity of bilayer graphene nanoribbons," *RSC Advances*, vol. 4, pp. 54474-54479, 2014.
- [60] J. R. Lukes and H. Zhong, "Thermal conductivity of individual single-wall carbon nanotubes," *Journal of Heat Transfer*, vol. 129, pp. 705-716, 2007.
- [61] T. Luo and G. Chen, "Nanoscale heat transfer—from computation to experiment," *Physical Chemistry Chemical Physics*, vol. 15, pp. 3389-3412, 2013.
- [62] E. Lussetti, T. Terao, and F. Müller-Plathe, "Nonequilibrium molecular dynamics calculation of the thermal conductivity of amorphous polyamide-6, 6," *The Journal of Physical Chemistry B*, vol. 111, pp. 11516-11523, 2007.
- [63] M. Nijmeijer, A. Bakker, C. Bruin, and J. Sikkenk, "A molecular dynamics simulation of the Lennard-Jones liquid–vapor interface," *The Journal of chemical physics*, vol. 89, pp. 3789-3792, 1988.
- [64] J. W. Pang, A. Chernatynskiy, B. C. Larson, W. J. Buyers, D. L. Abernathy, K. J. McClellan, *et al.*, "Phonon density of states and anharmonicity of UO<sub>2</sub>," *Physical Review B*, vol. 89, p. 115132, 2014.
- [65] E. Rossinsky and F. Müller-Plathe, "Anisotropy of the thermal conductivity in a crystalline polymer: Reverse nonequilibrium molecular dynamics simulation of the  $\delta$  phase of syndiotactic polystyrene," *The Journal of chemical physics*, vol. 130, p. 134905, 2009.
- [66] P. Shukla, A. Chernatynskiy, J. Nino, S. Sinnott, and S. Phillpot, "Effect of inversion on thermoelastic and thermal transport properties of MgAl<sub>2</sub>O<sub>4</sub> spinel by atomistic simulation," *Journal of Materials Science*, vol. 46, pp. 55-62, 2011.
- [67] B. Steele, A. Burns, A. Chernatynskiy, R. Grimes, and S. Phillpot, "Anisotropic thermal properties in orthorhombic perovskites," *Journal of materials science*, vol. 45, pp. 168-176, 2010.

- [68] T. Watanabe, S. G. Srivilliputhur, P. K. Schelling, J. S. Tulenko, S. B. Sinnott, and S. R. Phillpot, "Thermal Transport in Off-Stoichiometric Uranium Dioxide by Atomic Level Simulation," *Journal of the American Ceramic Society*, vol. 92, pp. 850-856, 2009.
- [69] A. McGaughey and M. Kaviany, "Observation and description of phonon interactions in molecular dynamics simulations," *Physical Review B*, vol. 71, p. 184305, 2005.
- [70] J. A. Thomas, R. M. Iutzi, and A. J. McGaughey, "Thermal conductivity and phonon transport in empty and water-filled carbon nanotubes," *Physical Review B*, vol. 81, p. 045413, 2010.
- [71] F. Müller-Plathe, "A simple nonequilibrium molecular dynamics method for calculating the thermal conductivity," *The Journal of chemical physics*, vol. 106, pp. 6082-6085, 1997.
- [72] C. Nieto-Draghi and J. B. Avalos, "Non-equilibrium momentum exchange algorithm for molecular dynamics simulation of heat flow in multicomponent systems," *Molecular Physics*, vol. 101, pp. 2303-2307, 2003.
- [73] K. V. Tretiakov and S. Scandolo, "Thermal conductivity of solid argon from molecular dynamics simulations," *The Journal of chemical physics*, vol. 120, pp. 3765-3769, 2004.
- [74] T. Gibbons and S. Estreicher, "Impact of Impurities on the Thermal Conductivity of Semiconductor Nanostructures: First-Principles Theory," *Physical review letters*, vol. 102, p. 255502, 2009.
- [75] D. J. Evans, "Homogeneous NEMD algorithm for thermal conductivity—application of non-canonical linear response theory," *Physics Letters A*, vol. 91, pp. 457-460, 1982.
- [76] G. P. Srivastava, *The physics of phonons*: CRC Press, 1990.
- [77] J. C. Fogarty, H. M. Aktulga, A. Y. Grama, A. C. Van Duin, and S. A. Pandit, "A reactive molecular dynamics simulation of the silica-water interface," *The Journal of chemical physics*, vol. 132, p. 174704, 2010.
- [78] W. G. Hoover, *Computational statistical mechanics*: Elsevier, 2012.

- [79] J. S. Bunch, A. M. van der Zande, S. S. Verbridge, I. W. Frank, D. M. Tanenbaum, J. M. Parpia, *et al.*, "Electromechanical resonators from graphene sheets," *Science*, vol. 315, pp. 490-493, Jan 2007.
- [80] J. S. Bunch, S. S. Verbridge, J. S. Alden, A. M. van der Zande, J. M. Parpia, H. G. Craighead, *et al.*, "Impermeable atomic membranes from graphene sheets," *Nano Letters*, vol. 8, pp. 2458-2462, Aug 2008.
- [81] J. C. Meyer, A. K. Geim, M. I. Katsnelson, K. S. Novoselov, T. J. Booth, and S. Roth, "The structure of suspended graphene sheets," *Nature*, vol. 446, pp. 60-63, Mar 2007.
- [82] C. Lee, X. D. Wei, J. W. Kysar, and J. Hone, "Measurement of the elastic properties and intrinsic strength of monolayer graphene," *Science*, vol. 321, pp. 385-388, Jul 2008.
- [83] A. A. Balandin, S. Ghosh, W. Z. Bao, I. Calizo, D. Teweldebrhan, F. Miao, *et al.*, "Superior thermal conductivity of single-layer graphene," *Nano Letters*, vol. 8, pp. 902-907, Mar 2008.
- [84] R. Murali, Y. X. Yang, K. Brenner, T. Beck, and J. D. Meindl, "Breakdown current density of graphene nanoribbons," *Applied Physics Letters*, vol. 94, Jun 2009.
- [85] M. Meyer, "NASA Technology Roadmap: In-Space Propulsion Systems," ed: NASA, 2012.
- [86] H. Inoue, H. Okamoto, and Y. Hiraoka, "EFFECT OF THE CHEMICAL-STRUCTURE OF ACID DIANHYDRIDE IN THE SKELETON ON THE THERMAL-PROPERTY AND RADIATION-RESISTANCE OF POLYIMIDE," *Radiation Physics and Chemistry*, vol. 29, pp. 283-288, 1987.
- [87] R. Mishra, S. P. Tripathy, K. K. Dwivedi, D. T. Khathing, S. Ghosh, M. Muller, *et al.*, "Spectroscopic and thermal studies of electron irradiated polyimide," *Radiation Measurements*, vol. 36, pp. 621-624, Sep 2003.
- [88] L. Yue, Y. Y. Wu, C. Y. Sun, J. D. Xiao, Y. P. Shi, G. L. Ma, *et al.*, "Investigation on the radiation induced conductivity of space-applied polyimide under cyclic electron irradiation," *Nuclear*

- Instruments & Methods in Physics Research Section B-Beam Interactions with Materials and Atoms*, vol. 291, pp. 17-21, Nov 2012.
- [89] S. Devasahayam and D. J. T. Hill, "Effect of electron beam radiolysis on mechanical properties of high performance polyimides. A comparative study of transparent polymer films," *High Performance Polymers*, vol. 17, pp. 547-559, Dec 2005.
- [90] A. v. Duin, "ReaxFF reactive molecular dynamics program manual," P. S. University, Ed., ed, 2013.
- [91] Z. Li, A. Borner, and D. A. Levin, "Multi-scale study of condensation in water jets using ellipsoidal-statistical Bhatnagar-Gross-Krook and molecular dynamics modeling," *Journal of Chemical Physics*, vol. 140, Jun 2014.
- [92] L. Zheng, A.Rahnamoun, A.Borner, D.A.Levin, A.van Duin "BGK and MD Simulations of water Supersonic Condensed Jets," AIAA 2014, pp. 2819.
- [93] W. Habashi, S.Nilamdeen, "Multiphase Approach Toward Simulating Ice Crystal Ingestion in Jet Engines," *J.Propulsion and Power* vol. 27, pp. 959-969, 2011.
- [94] *Orbiting debris : a space environmental problem*: DIANE Publishing.
- [95] V. V. Hoang, "Molecular dynamics simulation of amorphous SiO<sub>2</sub> nanoparticles," *The Journal of Physical Chemistry B*, vol. 111, pp. 12649-12656, 2007.
- [96] O. Andersson and A. Inaba, "Thermal conductivity of crystalline and amorphous ices and its implications on amorphization and glassy water," *Physical Chemistry Chemical Physics*, vol. 7, pp. 1441-1449, 2005.
- [97] W. M. Haynes, *CRC handbook of chemistry and physics*: CRC press, 2014.
- [98] D. R. Lide, *CRC handbook of chemistry and physics*: CRC press, 2004.
- [99] J. Klinger, D. Benest, and N. A. T. O. S. A. Division, *Ices in the solar system*: D. Reidel, 1985.

- [100] J. M. Ziman, *Electrons and Phonons: The Theory of Transport Phenomena in Solids*: OUP Oxford, 1960.
- [101] J. Kotakoski, J. C. Meyer, S. Kurasch, D. Santos-Cottin, U. Kaiser, and A. V. Krasheninnikov, "Stone-Wales-type transformations in carbon nanostructures driven by electron irradiation," *Physical Review B*, vol. 83, Jun 23 2011.
- [102] F. Banhart, J. Kotakoski, and A. V. Krasheninnikov, "Structural Defects in Graphene," *Acs Nano*, vol. 5, pp. 26-41, Jan 2011.
- [103] S. G. Srinivasan, A. C. T. van Duin, and P. Ganesh, "Development of a ReaxFF Potential for Carbon Condensed Phases and Its Application to the Thermal Fragmentation of a Large Fullerene," *Journal of Physical Chemistry A*, vol. 119, pp. 571-580, Jan 2015.
- [104] O. Lehtinen, J. Kotakoski, A. V. Krasheninnikov, A. Tolvanen, K. Nordlund, and J. Keinonen, "Effects of ion bombardment on a two-dimensional target: Atomistic simulations of graphene irradiation," *Physical Review B*, vol. 81, p. 4, Apr 2010.

## VITA

Ali Rahnamoun

### Academic Background

---

- Doctor of Philosophy, Mechanical Engineering (January 2012-Present)  
Institution: Pennsylvania State University
- M.S, Chemical Engineering  
Institution: Pennsylvania State University
- M.S, Mechanical Engineering  
Institution: Sharif University of Technology
- B.S, Mechanical Engineering  
Institution: Sharif University of Technology

### Research Experience:

---

*2012-2015 Graduate Research Assistant*, Mechanical Engineering Department,  
Penn State University

- Investigating the role of Propylamine functionalized POSS structure on CO<sub>2</sub> capture
- Obtaining insights into electron irradiation damage in kapton using reactive molecular dynamics simulation
- Modifying and implementing ReaxFF force field parameters for capturing the high energy ion impacts on graphene surface
- Study of reactive and non-reactive interactions of gases and impacting clusters on the surfaces of different materials using ReaxFF program
- Conducted reactive molecular dynamics simulations of hypervelocity impact of atomic oxygen on the disintegration of Kapton, POSS polyimide, amorphous silica and Teflon
- Performed Computer simulations on thermal conductivity calculations of materials using molecular dynamics simulations

*Fall 2011 Teaching Assistant*, CHE 480W, Chemical Engineering Laboratory

- Clarified key concepts of HPLC, fluid flow and heat Transfer experiments and assisted students during experiments and office hours
- Graded homework assignments and exams

*2009-2011 Graduate Research Assistant*, Mechanical Engineering Department, Penn State University

- Kinetic Monte Carlo simulation and model predictive control of thin film deposition